Universidade de Aveiro Departamento de Engenharia Mecânica
2018

Carmen Dias dos Santos

Análise do Ruído Aeroacústico de Ventiladores Axiais com Recurso a Dinâmica dos Fluidos Computacional (CFD) e Aeroacústica Computacional (CAA)

Aeroacoustic Noise Analysis of Axial Fans using Computational Fluid Dynamics (CFD) and Computational Aeroacoustics (CAA)

Com o apoio dos projetos: UID/EMS/00481/2013-FCT
CENTRO-01-0145-FEDER-022083

Universidade de Aveiro Departamento de Engenharia Mecânica
2018

Carmen Dias dos Santos

Análise do Ruído Aeroacústico de Ventiladores Axiais com Recurso a Dinâmica dos Fluidos Computacional (CFD) e Aeroacústica Computacional (CAA)

Aeroacoustic Noise Analysis of Axial Fans using Computational Fluid Dynamics (CFD) and Computational Aeroacoustics (CAA)

Dissertação apresentada à Universidade de Aveiro para cumprimento dos requisitos necessários à obtenção do grau de Mestre em Engenharia Mecânica, realizada sob orientação científica de Rui António da Silva Moreira, Professor Auxiliar do Departamento de Engenharia Mecânica da Universidade de Aveiro e de Jürgen Herbst, Engenheiro Acústico do Departamento TT-RHP/Eng-Av da Bosch Termotecnologia S.A..

O júri / The jury

Presidente / President

Professor Doutor Robertt Angelo Fontes Valente
Professor Associado da Universidade de Aveiro

Vogais / Committee

Professor Doutor José Fernando Dias Rodrigues
Professor Associado da Faculdade de Engenharia da Universidade do Porto

Professor Doutor Rui António da Silva Moreira
Professor Auxiliar da Universidade de Aveiro

Confidentiality Clause

This final thesis is based on internal, confidential data of Bosch Thermotechnik GmbH. This work may only be available to the first and second reviewers and authorized members of the board of examiners. An inspection of this work by third parties requires the expressed admission of Bosch Thermotechnik GmbH. Any publication and duplication of this final thesis, even in part, is prohibited until 2 years after the day of the presentation.

Agradecimentos / Acknowledgements

First, I would like to thank my advisors Prof. Dr. Rui Moreira from the Mechanical Engineering Department of the University of Aveiro, and Dr. Jürgen Herbst from the Heat Pump Development Department of Bosch Termotecnologia S.A., for the continuous support, advice and brainstorms that helped me guide this work in the right direction. Their passionate participation and input was very valuable. I would also like to thank Alister Clay from Bosch Thermotechnik GmbH. Junkers, for training me in Computational Fluid Dynamics. His guidance and recommendations were incredibly helpful. I want to express my gratitude towards my colleagues Paulo Trindade, Rómulo Lima and Luise Hötzel, for their help and availability in bringing several ideas to life. On a final remark, I also want to thank the people who steered my academic journey into a memorable experience: my parents, for teaching me the value of hard and smart-work; my sisters, for keeping my competitive spirit alive and my friends Sara, Joana, Gonçalo, Gaspar, Miguel, Carneiro, Nunes and Barros, who kept their sense of humor when I had lost mine.

Palavras-chave

Aeroacústica; Bomba de Calor; Ruído de Ventiladores Axiais; Fontes de Ruído Aerodinâmico; Turbulência na Camada Limite; Arestas serradas; Cavidades de Bolas de Golf

Resumo

O objetivo deste trabalho de investigação consistiu na análise do ruído aeroacústico emitido por dois ventiladores de diâmetros diferentes aplicados em duas unidades exteriores de bombas de calor, recorrendo a *Computational Fluid Dynamics* (CFD) e *Computational Aeroacoustics* (CAA). O modelo acústico *Broadband Noise Source* (BNS) e o modelo de turbulência *Transition SST*, implementados no código comerical *Fluent* 19.0, foram utilizados para detetar o ruído da camada limite dos diversos casos de estudo, utilizando simulações em regime permanente. Os objetivos do estudo estão divididos em três componentes: a análise da relação entre o diâmetro e a velocidade de ponta com o ruído aeroacústico, o estudo da influência do disco do motor na acústica da camada limite e a análise de arestas serradas e ventiladores com cavidades inspiradas nas bolas de Golf. Os resultados indicam um potential para redução do ruído aerodinâmico de 3,3 e 4 dB no modo de baixa e alta velocidade, respetivamente, utilizando o ventilador maior no *chassis* mais pequeno, uma vez que requer velocidades mais baixas para atingir o mesmo caudal de ar. Foi descoberto que o disco do motor influencia a distribuição do caudal à saída do ventilador e que previne o fluxo inverso de ar. Apesar de influenciar os pontos de operação do ventilador, utilizar o disco demonstra um potencial de redução de ruído de 0,4 e 0,8 dB num dos modelos nas velocidades anteriormente mencionadas, após ajustes para os requisitos de caudal. Por fim, foi descoberto que adicionar cavidades a regiões da superfície de ventiladores com tendência para separações de fluxo de ar pode prevenir este fenómeno e reduzir a energia cinética turbulenta, favorecendo o ruído da camada limite. Este fenómeno torna-se mais evidente em condições de operação perto do *stall* aerodinâmico. Não se registaram melhorias significativas no modelo com arestas serradas. Medições experimentais realizadas num túnel entálpico e numa câmara semi-anecóica dos três protótipos impressos à escala reduzida mostraram melhorias na ordem dos 3,7 e 5,3 $dB(A)$, a 350 rpm, com os modelos com cavidades e com arestas serradas, contudo novas medições devem ser conduzidas com igual qualidade de impressão para confirmação dos resultados.

Keywords Aeroacoustics; Heat Pump; Axial Fan Noise; Aerodynamic Noise Sources; Boundary Layer Turbulence; Serrated Trailing Edge; Golf-ball Dimples

Abstract The aim of this investigation is the aeroacoustic noise analysis of two fan models with different sizes used within two heat pump units, using Computational Fluid Dynamics (CFD) and Computational Aeroacoustics (CAA). The Broadband Noise Source (BNS) model and Transition SST turbulence model, implemented in Fluent 19.0, were used to detect the boundary layer noise component of the case studies in steady-state simulations. The targets of this study were divided in three main parts: analysis of the relation between diameter and tip speed and aeroacoustic noise, the motor cap's influence on boundary layer noise and the analysis of serrated trailing edges and fans with golf-ball dimples. Results indicate a potential of 3,3 and 4 dB aerodynamic noise improvement at low and high speed flow requirements, respectively, using the bigger fan in the small-chassis, due to the lower speed needed to maintain the same airflow rate. It was found that the motor cap influences downstream airflow and reduces reverse flow. Although influencing the operating point of the fans, using the motor cap shows 0,4 and 0,8 dB improvement potentials for one of the fan models at the aforementioned speed modes, after adjustments for required airflow rates. Lastly, it was discovered that adding dimples to regions of the fan's surface with a bias towards flow separation can help prevent the phenomenon and reduce turbulent kinetic energy in the near airflow, improving boundary layer noise. This becomes more evident in near-stall/stall operating conditions. The trailing edges didn't show considerable improvements for the fan model they were added to. Experimental measurements of the three re-scaled 3D printed fan models, conducted in an enthalpic tunnel and a hemi-anechoic chamber, showed noise improvement potentials in the order of 3,7 and 5,3 $dB(A)$ at 350 rpm for the fans with dimples and serrated edges, but new measurements need to be conducted with equal printing quality on all models to confirm the results.

Contents

List of Tables

List of Figures

Chapter 1

Introduction

This research work was developed within the Acoustics Team from Bosch Termotecnologia S.A., located in Aveiro, and relates to aeroacoustic noise simulations of axial fans in the context of its application in heat pump units. In this chapter, a brief introduction to the company and the fan noise concept can be consulted, as well as the motivation behind the scope of this thesis and how its significance can reflect in several different industries.

1.1 Bosch Termotecnologia S.A.

Bosch Thermotechnology is one of the world leading manufacturers of heating products. It offers solutions for room climate, domestic hot water and decentralized energy management. The company uses comprehensive know-how in condensing technology, solar thermal systems, heat pumps and combined-heat-and-power to meet the demands of the market, while contributing for the transition to cleaner energy and reducing CO_2 emissions.

In Aveiro, Bosch Termotecnologia S.A. focuses on the design and development of new devices, as well as its production and marketing. Currently, this location of Bosch Thermotechnology works on water heaters, gas boilers, electrical appliances for water heating and heat pumps.

The Bosch Heat Pumps comprise a variety of different models that range from low to high capacity. On the outdoor unit, the heat exchange takes place on the evaporator unit using forced convection; an axial fan is mounted after the evaporator with the aim of forcing airflow out of the heat pump chassis. The Bosch Heat Pump external units currently use one of two distinct fan models with different blade designs. Both models were designed and developed by Ebm-papst and represent the main focus of this research work.

1.2 Fan Noise

Fans are a common industrial component used to move air usually through a duct system. There are two major fan classes: axial and centrifugal fans, and within them several different types exist.

In short, fans work by inducing static and kinetic energy to the air around them as a result of their aerodynamic characteristics, thus creating a pressure differential which induces a force and causes the air to flow. The airflow is characterized by relatively low pressure, low velocity and high volume rate. In axial fans, the air flows parallel to the fan drive shaft. Fans are a common noise source in industrial applications. Noise generation is strongly influenced by inlet flow conditions and the blade tip speed. Depending on the axial fan function, there are two main types [1], listed bellow:

- Tube axial or propeller fans: these fans are widely used and usually have a variable pitch angle that can be adjusted for varying inlet pressures, discharge pressures and flow rates. Noise generated by these type of fans is characterized by a low-frequency dominated spectrum.

- Vane axial fans: similar to the previously mentioned type, but with incorporated downstream guide vanes, these fans are usually used in aircraft engines. Guide vanes increase the fan efficiency but also increase the mid to high-frequency noise levels due to the downstream flow-stator interaction.

Axial fans are employed in a wide variety of technologies and industries such as domestic HVAC systems, electronics cooling, aircraft engines, UAVs, industrial applications using heat exchangers and aerogenerators; in all its applications, axial fans have a common constraint: its noise emission to the far-field [2].

The noise emission is not only dependent on the fan type but also on the operating conditions. Relatively to the recommended values, higher airflow and lower static pressure increase noise, whereas the opposite tend to increase the low-frequency noise. All fans generate a tone at the blade passing frequency (BPF), given by Equation (1.1),

$$BPF = \frac{Nb \cdot rpm}{60} \tag{1.1}$$

where Nb represents the number of blades and rpm the rotation speed in revolutions per minute. The extent to which this tone is noticeable depends on the fan type and its operating conditions. Sometimes, the BPF tone and/or its harmonics can be amplified due to the following factors [1]:

- Acoustic resonance in the ductwork;

- Distortions at the inflow;

- Inlet volume control dampers;

- Turbulent and unstable flow behaviors.

The evaluation of fan noise sources and their frequency domain is therefore imperative to identify adequate noise reduction methods. In this work, focus will be given on the last of the aforementioned factors, the evaluation of fan noise sources due to turbulent behavior of the airflow and its interaction with solid surfaces, such as the blades, the motor and the shroud.

1.3 Motivation

In modern day engineering applications, noise legislations and regulations have become more stringent, mainly due to increasing urbanization and better living quality requirements. Several examples can be given to demonstrate the importance of reducing rotating machinery noise due to its impact in technological, economical, social and governmental aspects. For example, in industrial production facilities which resort to fans, noise emissions can be decisive in the plant size due to their proximity to urban areas. Therefore an improvement in fan noise emissions can lead to higher plant sizing freedom and production plant efficiency [2].

In regard to aircraft engine noise, several studies have identified fans as the major source of noise in aircraft take-off and approach [3; 4]. Considering the steadily growing number of both passenger and freight air traffic, and taking into account that air traffic is expected to increase by 50% over the next 20 years [5], it becomes ever more imperative to improve noise emissions for protection and relief of the people affected by it. Since the introduction of jet engines, technology improvements have led to a volume reduction of 25 dB mainly accomplished by active noise control measures [6]. The same idea applies to low-flying aircraft such as helicopters and small planes.

The drone industry is also an increasingly growing market which finds application in military operations, where noise reduction is understandably a major concern. Since 2017, in Europe, the drone industry is obligated to follow rules emitted by the European Aviation Safety Agency (EASA) concerning noise generation. [5]

On December 7th 2016, Amazon Prime Air performed the first fully autonomous air product delivery using a small drone [7]. The company states that, in a near future, seeing air delivery drones will be as normal as seeing Mail Lorries on the road, which is another indicator of expected increase of air traffic for small aircraft.

Even in the filmmaking industry, drones are widely used for videotape capture. As stated by Rick Gaeta, director of Oklahoma State University Unmanned Systems Development Center, noise interferes with footage and results in added time and capital to post-processing. In a world of streaming news, noise is a disturbance and restricts the industry [8].

In the energy sector, aerogenerator noise emissions have been proven to impact the health of people living near industrial wind turbine plants. Symptoms include sleep disturbances, stress, anxiety, depression and cognitive dysfunction, being wind turbine noise the main established cause of them [9].

Another relevant example are the growing complaints about the low-frequency noises of HVAC systems such as heat pumps, air-conditioning systems and district heating stations in residential areas, even if the noise levels comply with the standard limits. Entities like the German Environment Agency (UBA) therefore advise parties of construction projects of such facilities to evaluate noise emissions in early stages of project planning. Technical and legal framework options are also under investigation for low-frequency noise in residential areas [10].

Considering the advance of fan application technologies and the associated noise emission problems, it becomes understandable why aeroacoustic analysis and fan noise reduction techniques represent research fields which have been increasing progressively [11; 12]. Manifestly, the main goal of aeroacoustics is to reduce fan noise without affecting its aerodynamic performance.

1.4 Objectives

With the aim of reducing the Heat Pumps' noise, Bosch has been focusing on the reduction of the noise contribution of each component. This thesis was developed with the aim of detecting the main broadband noise sources of the axial fan component and investigating eventual noise improvement techniques applicable within the heat pump environment.

Computational Fluid Dynamics (CFD) and Computational Aeroacoustics (CAA) were used to analyze the aeroacoustics of the two fan models currently used in Bosch Heat Pumps: a ⌀500 mm fan and a ⌀630 mm fan model. Using a steady-state approach, the overall airflow behavior, the flow turbulence and the aerodynamic noise at the fan blades and motor surfaces were analyzed using the Broadband Noise Source (BNS) Model as the acoustics model and Transition SST as the turbulence model. Both algorithms are implemented in the commercial code Fluent 19.0.

The first approach analyzed the diameter and tip speed influence by comparisons between both fan models and their re-scaled versions; further, the influence of the motor cap on aerodynamic noise was studied and different variations were created for optimization purposes; finally, two noise reduction features were simulated in free flow and within the heat pump environment and compared to the noise levels of a simplified version of the original fan. The final approach consisted in re-scaling and 3D printing the three fan prototypes for measurements in an enthalpic tunnel and in a semi-anechoic chamber, so the noise levels of the fan with dimples and the fan with serrated edges could be compared to the reference model.

Chapter 2

State of the Art

2.1 Noise Reduction Techniques for Industrial Applications

In this chapter, an overview regarding different noise reduction methods used in industrial applications is presented.

The topics range from well known and debated aeroacoustic problems such as aircraft engine noise, to more recently arising subjects and complaints regarding unmanned aerial systems and aerogenerators.

2.1.1 Aircraft engine fans

In aircraft engine technology, the fan is one of the major sources of noise [12]. Even with acoustic liners, studies have shown that fans dominate total engine noise during take-off and approach to landing, as can be observed in Figure 2.1.

Guide vanes have a special contribution for noise generation in aircraft engines. Studies conducted under the Advanced Subsonic Technology (AST) Program have shown that sweeping and leaning the outlet guide vanes has significant benefits, showing noise reductions in the order of 5 dB in the inlet quadrant and 10 dB in the exhaust quadrant for all tested angles [3]. This benefit is due to the additional viscous wake decay and the additional variation in the phase of the incident wake along the vane span, which results in more wakes intersecting a single vane and therefore results in more noise cancellation and less interaction noise than without a swept and leaned stator.

An example of swept and leaned stators can be observed in Figure 2.2.

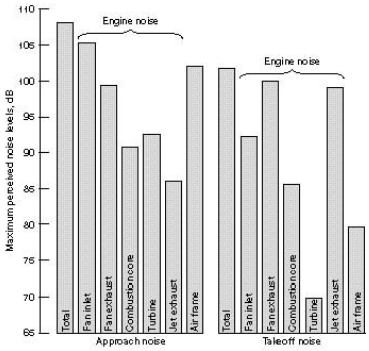

Figure 2.1: Breakdown of the noise components of a typical engine with 1992 level technology [13].

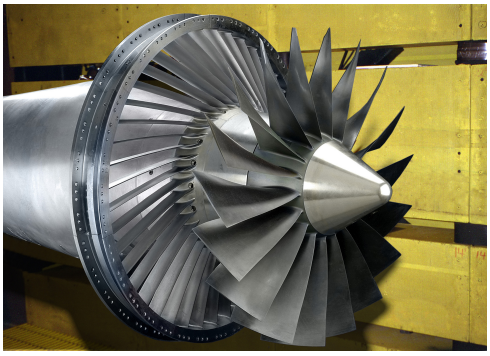

Figure 2.2: Swept, leaned stators, developed by NASA [14].

Another hypotheses tested in the AST-program was the active control of the fan noise, with the aim of generating an acoustic field that could cancel out the tonal noise component of aircraft fan noise. It was found to be a successful technique for generating a canceling acoustic field of equal amplitude but opposite phase as the one generated by the turbofan. The actuator array, which produced the canceling acoustic field, consisted of conventional electromagnetic drives (speakers) mounted upstream the fan test model. The experiments were executed considering local control (inlet or exhaust) or global control (both) and different numbers of spinning modes, where each mode corresponded to a specific frequency to be canceled by the actuator(s). The noise reduction for different fan speeds averaged around 18 dB, although the noise benefits tend to diminish with increasing number of simultaneously controlled modes, as expected in aircraft engines, due to the higher complexity of the mode phase relationship [17].

As newer engine cycles become less tone dominant, the incentive to investigate and apply active noise control diminishes, unless a new method to cancel broadband noise can be created. Therefore, practical applications of active noise control in turbofans remains an open development subject [3].

Another approach for fan noise reduction in aircraft engines is based on the modification of the fan wake. One technique for wake modification is mass injection at the blade trailing edge, also known as trailing edge blowing, which intends to lower the levels of unsteady vane loading by forcing the flow to become more uniform before its interaction with the stator vanes. This is accomplished by adding internal channels, which start at the blade root and terminate at the trailing edge, where the internal fluid is injected in the fan wake flow [18].

Fan tip speed has also been target of research as a noise reduction method in aircraft engines. By decoupling the fan from the low-pressure turbine with a gearbox, noise levels can be decreased substantially, since fan noise levels are estimated to be proportional to the fan tip speed [19].

Finally, serrated nozzles are also an example of a noise reduction mechanism implemented in aircraft. The geometry has shown to influence the flow development by reducing the peak turbulence and spreading rates [20].

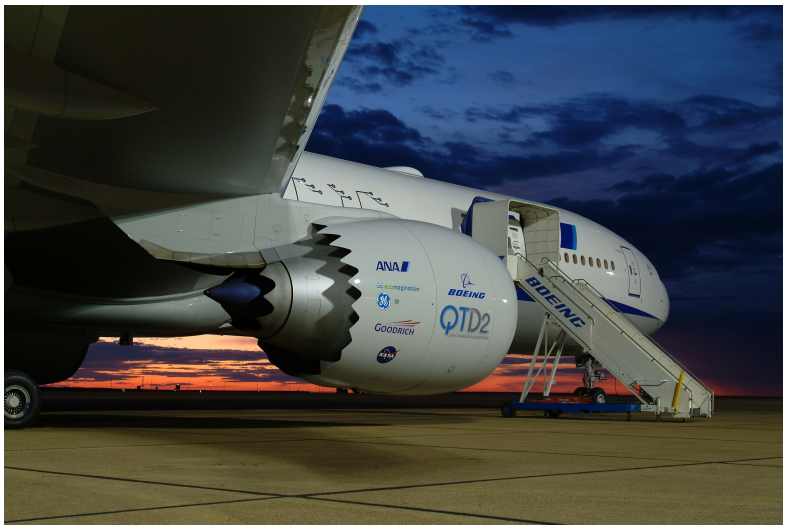

Figure 2.3: The Boeing 777 with chevron nozzles developed by NASA [15].

2.1.2 Helicopter rotor blades

Nowadays, the aerodynamic performance and the overall rotorcraft acoustics are both taken into account when designing a helicopter, as the demand is for both efficient and quieter aircraft.

The main sources of rotor noise are the blade tip speed and, to less extent, the blade loading. In this type of aircraft, a common blade-vortex interaction (BVI) noise is generated in descending flights, which led to continuous research in blade tip designs to improve noise emissions without compromising both hover and cruising performances. BVI occurs when a rotor blade passes within close proximity of the shed tip vortexes from the previous blade. This causes an impulsive change in the loading on the blade, resulting in noise emissions.

Over the past decades, effort has been given in designing a blade tip shape that aimed to split or diffuse the tip vortex before it interacts with the next blade, but these designs have not been adopted due to their limited performance potential. Easier options have been used, which consist mainly in using low volume tips at lower tipspeeds. Still, several authors are worth mentioning whose work contributed to understanding the challenge of reducing BVI noise. The work of *Landgrebe and Bellinger (1972), Tangler (1975), Boklehurst and Pike (1994), McAlister et al. (2001)* were focused on the reduction of BVI noise by altering the tip geometry of rotor blades, introducing several designs such as the Ogee tip, which aimed to reduce the peak velocity of the tip vortex by decreasing tip area, and the Vane tip, which aimed to separate the main vortex into two more discrete ones, see Figure 2.6 [21].

Researchers also focused on wing tip blowing. Slots were introduced into blades to direct turbulent airflow through the vortex, this way dissolving the inner laminar region. This is commonly known as vortex diffusion and consists in energizing the vortex flow. Results show a vortex swirl velocity reduction of nearly two-thirds but with an undesired power increase of 3% [21].

Further BVI noise reduction research lead to different tip designs, including the Ogee tip and a curved anhedral tip, among others, which were tested with a "turbulence

generating device" attached on the structure of the trailing edge vortex. The rotor was tested in hovering mode and the device was effective in reducing the tip vortex velocities, but also caused an 18% increase in rotor torque [21].

Until today, there appears to be no general consensus for helicopter blade tip design; the USA uses the sheared-tip or the swept-tapered-anhedral tip, while the UK uses the BERP tip and in Europe the Parabolic tip is widely used [21]. It is assumed that each tip is suited to its operating requirements. These are the three tip designs commonly found on helicopters, see figures 2.4, 2.5 and 2.7.

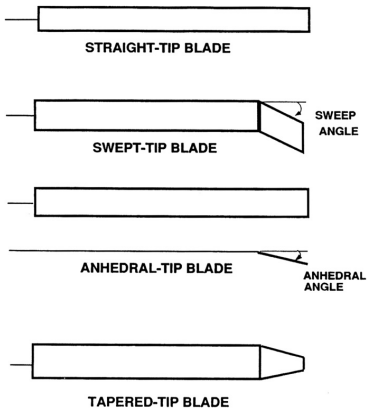

Figure 2.4: Examples of different types of rotor blade tip shapes currently used [21].

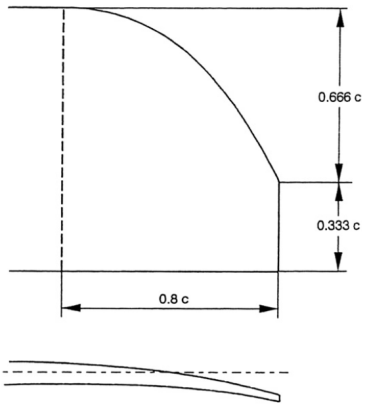

Figure 2.5: The parabolic tip SPP8 as designed by Joncheray [21].

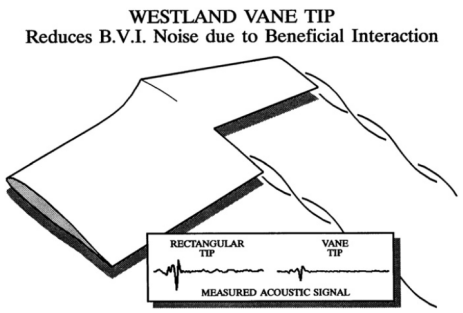

Figure 2.6: The Westland Vane tip, which aimed to separate the tip vortex into two [21].

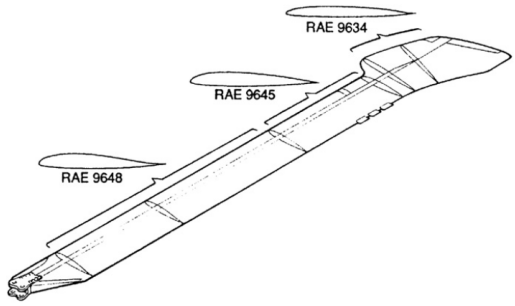

Figure 2.7: The B.E.R.P. tip, as proposed by Perry, with different airfoil sections along the span [21].

2.1.3 UAVs

In the drone industry, great importance has been given to noise reduction methods due to the high pitch noise emitted by UAVs; there is a considerable impact on psychoacoustics and the devices' noise is often described by people as annoying [22]. Besides military and police operations, civilian jobs can also be affected by drone noise; for example, wildlife-monitoring researchers and photographers often have difficulties to access the animals in their natural state due to noisy drone rotors.

Traditional techniques, such as winglets and blade loading compromise, are already

common to see on the drone market. Recent and innovative advances were accomplished by Dotterel Technologies, a New Zeland startup, which created noise reductive shrouds built with a nano-fibre acoustic damping material that reduces and directs the noise skywards, improving noise pollution experienced from the ground [23]. The company shares results in human noise perception of half as much as it would be without the damping shrouds.

Figure 2.8: Dotterel drone: lightweight propeller shrouds comprising sound-absorbing acoustic materials [24].

2.1.4 Aerogenerators

Trailing edge serrations are an accepted method to reduce the aeroacoustic noise from wind turbine blades, even though a complete understanding of serration noise reduction physics is still pending. Anechoic wind tunnel tests have proven the performance of serrations for noise improvement, but several gaps still exist concerning the serration driving parameters and the acoustic performance scaling of a serrated model [25].

Design optimization algorithms and simulation codes are still under research for turning serration prototype designs into commercially viable products.

Potential optimization in serration panel design was accomplished by *J. Mathew et al. (2016)* [25], with field measurements that indicate 1,5 *dB* noise reduction across the wind speeds of interest in three different wind turbines. Using reduced order models to predict aerodynamic, acoustic and structural performance of serrations, the researchers investigated the effect of serration dimensions and flap angles on lift and drag coefficients, bending moments on the serrations and, more importantly for this investigation, on the self-noise of the airfoils. For frequencies under 10 kHz, sound power level improvements up to 3,7 *dB* were accomplished using serration panels with a flap angle of 10°, as can be observed in Figure 2.9.

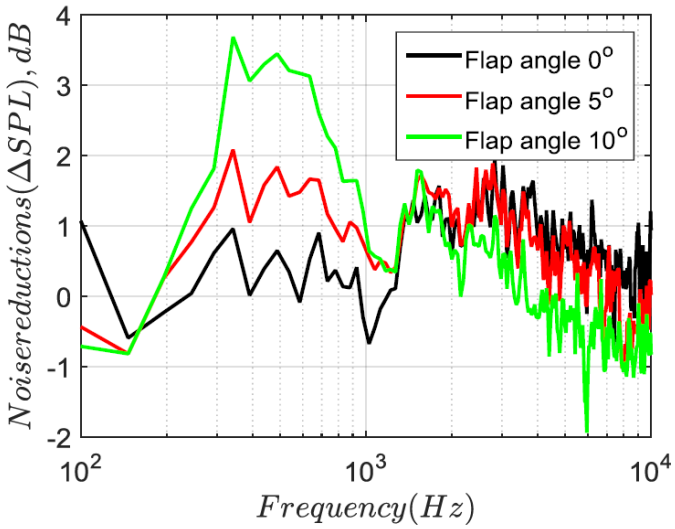

Figure 2.9: Impact of serration flap angle in noise reduction between the straight edge airfoil and the serrated airfoil [25].

The blade tip shape of wind turbines has also been object of investigations.

Studies conducted by *Maizi et al. (2018)* [25] on horizontal wind turbines have shown noise improvements with a consequent power output reduction of about 3% using a Shark Tip, when compared to a normal, reference tip. The results indicate that the shark tip reduces vorticity in several sections of the blade at a wind speed of 7 m/s (figures 2.10 and 2.11), thus improving the acoustic power for high frequencies above 1 kHz (Figure 2.12).

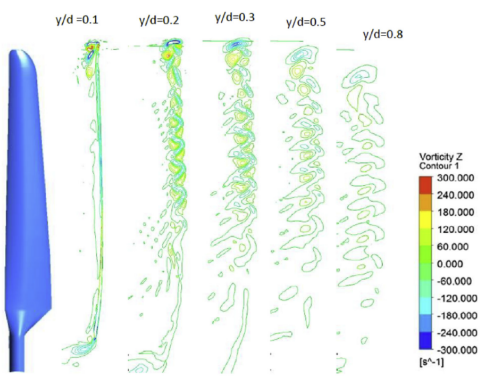

Figure 2.10: Z vorticity contours at different sections in the Y direction at 7 m/s wind speed - reference tip[26].

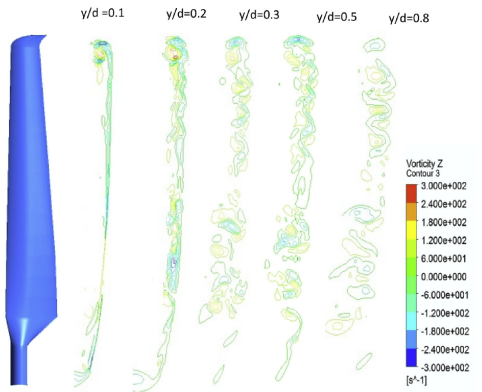

Figure 2.11: Z vorticity contours at different sections in the Y direction at 7 m/s wind speed - improved shark tip[26].

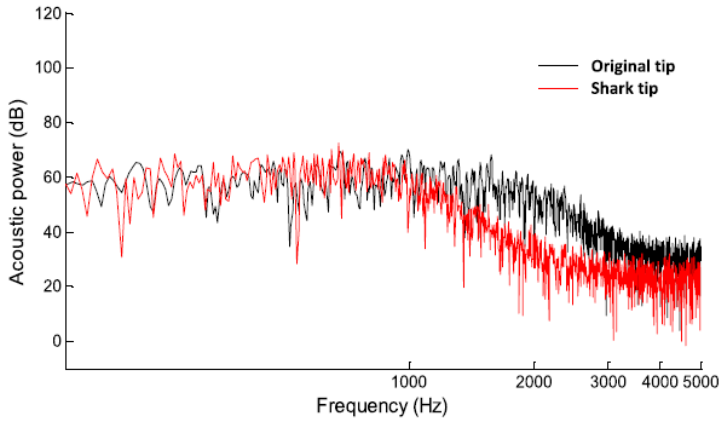

Figure 2.12: Acoustic power level spectra for both blades at 7 m/s [26].

Chapter 3

Theoretical Background

After a review of state of the art noise reduction techniques and fan noise characterization, focus will shift towards useful theoretical background for this investigation, namely noise generating mechanisms and its sources, fan affinity laws and potential solutions for noise reduction.

3.1 Axial Fan Noise Characterization

After an overview of the overall noise reduction techniques in general fan industrial applications, the focus will now shift towards fan noise characteristics.

Fan noise is a strong function of the rotational tip speed and fan pressure ratio. The most accurate way to reduce fan noise is to decrease the tip speed and pressure ratio, but this causes the fan diameter to increase in order to recover thrust [3]. A compromise between rotational velocity and fan diameter is therefore an aspect worth investigating while seeking fan noise reduction.

An axial fan noise spectrum usually comprises of a broadband noise component and a tonal noise component, which are harmonics of the blade passing frequency (BPF). In literature, most investigations focus on the reduction of the tonal component using transient analysis [27]. Thanks to previous investigations [28], sources of turbomachinery noise can be categorized into three major groups:

- a monopole source, as a consequence of the blade motion;
- a dipole source, caused by pressure fluctuations on the blades surfaces; and
- a quadrupole source, resulting from the turbulent flow.

These three major noise source groups categorize all the noise generating mechanisms caused by rotating motion, blade loading and fluid-solid interactions such as trailing edge vortex shedding, turbulent inlet flow fluctuations, tip leakage vortexes and the interactions of vortexes with neighboring blades or the rotor wake. In chapter 3.2, the aforementioned noise generating mechanisms are further discussed.

The major difference between the noise sources are elaborated below, namely their origin and directivity pattern.

3.1.1 Monopole Source

A monopole sound source represents a physical mass in a fixed region of space, which fluctuates and produces sound waves of equal strength in all directions, with a directivity pattern as shown in Figure 3.1. These sources periodically add and remove the same amount of mass from the involving system, which generates a relative sound power level equally radiated in every direction [2].

Sound power is a measure of acoustical energy emitted by a source per unit of time and, contrary to sound pressure, does not depend upon the distance from the source. If the monopole source is of aerodynamic nature, as in the case of the fan blade motion, the radiated sound power, measured in Watts $[W]$ can be related to the mean flow velocity as stated in Equation (3.1) [2].

$$SP_w \approx \frac{L^2 U^4 \rho_0}{4\pi c} \tag{3.1}$$

where L represents the typical dimension of the considered flow, such as the fan diameter, U stands for the mean flow velocity, ρ_0 for the mean flow density and c denotes the speed of sound. It can be stated that the sound power for a monopole sound source with aerodynamic nature scales with the power of four of the mean flow velocity. As stated in literature [27; 28], the sound power of the periodic fan blade motion can this way be scaled to the fourth power of the mean airflow velocity.

3.1.2 Dipole Source

The dipole sound source consists of two monopole sources of equal strength but opposite phase. The separation distance between both monopoles is usually considerably smaller than the wavelength of the generated sound waves. Physically, a dipole source can be represented by a fluctuating point of mass in space, oscillating back and forth in its involving environment, creating a fluctuating force [2]. The directivity pattern for a dipole source can be observed in Figure 3.2.

Dipoles are weaker sound sources than monopoles, due to the interference between the two sources in the perpendicular directions to the source's axis.

The sound power radiation on a dipole of aerodynamic nature can be expressed as stated in Equantion (3.2) [2].

$$SP_w \approx \frac{d^2 U^6 \rho_0}{3\pi c^3} \tag{3.2}$$

where d denotes the distance between the sources. For a dipole source, the sound power scales with the power of six of the mean flow velocity, which correlates to the sound power associated to pressure fluctuations on a fan blade surface.

3.1.3 Quadrupole Source

A quadrupole source can have two configurations: a linear/longitudinal quadrupole or a lateral quadrupole.

The longitudinal or linear source is characterized by two dipoles, aligned on the same axis but with opposite directions. The directivity pattern changes from the near-field to the far-field; whilst the dipoles cancel each other out at a distance sufficiently far

from the sources, in the near-field there will still be sound emission in the perpendicular direction of the dipole's axis, due to the distance between each one's path length. In the far-field, this distance becomes negligible and the waves cancel each other out, as demonstrated in Figure 3.3 (a).

The lateral quadrupole represents four sources of sound located near each other and creating a square geometry, where each has a different phase than its neighbour. The directivity pattern is shown in Figure 3.3 (b). The waves cancel each other out in the perpendicular direction to the square sides due to the opposite phases, but remain equal in the directions of the corners of the square [2].

The sound power radiation can be expressed by equations (3.3) and (3.4) for a linear and a lateral quadrupole source, respectively.

$$SP_{linear} \approx \frac{d^2 U^8 \rho_0}{15\pi c^5} \tag{3.3}$$

$$SP_{lateral} \approx \frac{d^2 U^8 \rho_0}{5\pi c^5} \tag{3.4}$$

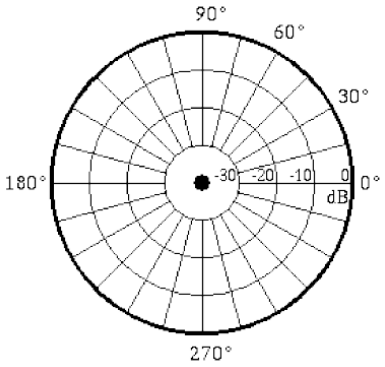

Figure 3.1: Monopole directivity field [2].

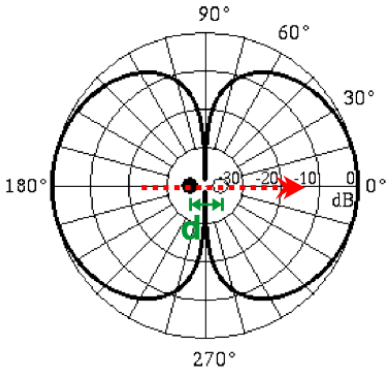

Figure 3.2: Dipole directivity field, where d represents the distance between the sources and the arrow its axis [2].

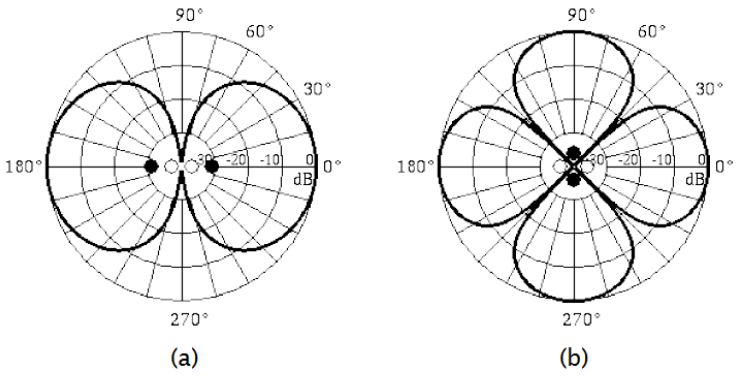

Figure 3.3: Directivity patterns a) longitudinal quadrupole in far-field b) lateral quadrupole [2].

Again, the quadrupole source is a weaker sound source due to the increased wave cancellation phenomenon, when compared to a monopole or a dipole. The turbulent flow characteristic of rotating machinery can therefore be correlated with a sound power scaled with the eighth power of the mean flow velocity.

3.2 Noise Reduction Features for Axial Fans

Axial fan noise prediction methods are based on expensive computational methods such as Large Eddy Simulations (LES) or Direct Numerical Simulation (DNS), but the application of these methods is not yet completely feasible for concrete evaluation of fan designs [2] using common computational resources. Therefore, noise reduction features are usually evaluated and validated recurring to experimental testing. Over the years, several investigations and testing, whilst analyzing both fan performance and its noise emission, lead to the existence of noise reduction features which can be seen on regular, commercially available fans. This chapter is dedicated to the analysis of these features.

3.2.1 Skewed Blades

One of the most important parameters that define low-pressure axial fan performance and acoustics is the fan blade skew, since it has major impact on the flow-field. Recent aeroacoustic investigations on different skew geometries [29] have shown that forward-curved blades have lower sound emission than backward-skewed or unskewed blades.

Investigations conducted by Zenger and Becker [29] compared both geometries and performed a fluid mechanical and acoustic characterization. Laser Doppler Anemometry (LDA) measurements were realized at the pressure and suction side of forward-and backward-skewed fan blades and it was observed that the backward-skewed blade induced flow in the outwards direction, while at the forward-skewed blade an inwards directed flow was perceived.

The forward-skewed blade registered lower broadband noise in mid-frequency region (0,5 kHz to 2 kHz), but higher in the high-frequency region (higher than 2 kHz). The authors attribute this increase at higher frequencies to accentuated vortex shedding on the trailing edge, caused by an increased velocity profile perpendicular to the trailing edges, which on the other hand is caused by the induced inward flow, characteristic of this skew type. The backward-skewed blade registered higher noise emissions due to the thicker boundary layer manifested on the suction side of the blade, caused by the radially outwards directed flow. This radial migration has a major influence on the turbulent kinetic energy at the pressure and suction side, see Figure 3.4. Authors reveal almost identical pressure and suction side contours for both fans, therefore only plots at the pressure side are shown. Also, subharmonic components (non-corresponding to BPF and BPF harmonics) were manifested in the spectrum, justified by increased kinetic energy registered at the blade tip region created by complex flow phenomena: backflow from pressure to suction side interaction with the fan blades. [29] Therefore, forward-skewed blades present lower noise emissions in general.

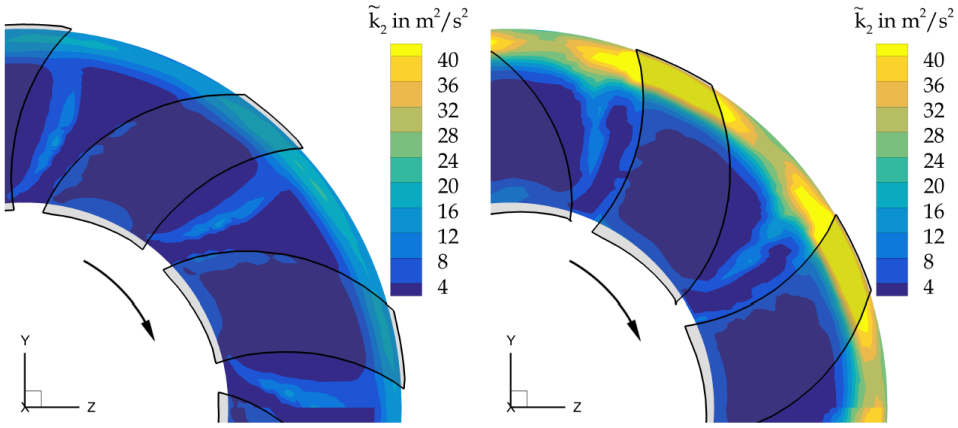

Figure 3.4: Mean turbulent kinetic energy, $\tilde{k}_2$, at the fan pressure side of a forward- (left) and backward-skewed fan (right) [29].

3.2.2 Winglets

Winglets are features widely used in flight engineering and aim to reduce tip vortexes. In small, shrouded fans, winglets are used to reduce the turbulence felt at the tip clearance. Experimental studies conducted by Nashimoto *et al.* [30] showed the influence of winglets in reducing tip vortexes and vorticity magnitude in the near wake region, denoting a noise level reduction of about 1 dB for a fan with winglets.

Ebm-papst [31] states that winglets on shrouded, axial fans reduce the transportation of air mass into the tip clearance region, thus reducing the force on the blade tip vortex and improving noise levels at given airflow levels. The company also states an improvement of 2 to 4 $dB(A)$ for different fan operating points, as shown in Figure 3.5.

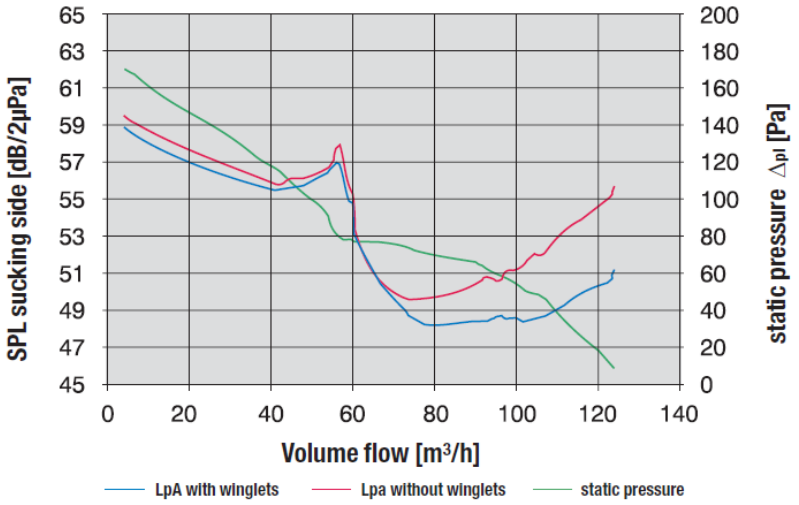

Figure 3.5: Comparison of SPL on the suction side of fans with and without winglets at different operating points [31].

3.2.3 Serrated Edges and other treatments

Serrated edges are a noise reduction feature applied to airfoils and rotor blades, which aim to reduce the wake separation and vortex shedding on regions of flow instability. The most common application of serrations can be seen at trailing edges, with the aim of inducing wake attenuation [32]. Several investigation showed that serrated trailing edge inserts can achieve a self-noise reduction of 2 up to 6 dB with significant reduction at high frequencies, while maintaining an acceptable aerodynamic performance [33].

The sudden flow expansion at a blunt trailing edge of an airfoil can generate vortexes and consequently noise. To some extent, the vortexes can also fall upon the leading edge of the neighbor rotor blade. Serrated trailing edges can also help in delaying aerodynamic stall conditions by energizing the low momentum region at the blade suction side. Serrations induce two separate flows: the flow at the *tip* region, as seen from the suction side, and the flow at the *root*, as seen from the pressure side. Both flows interact at the suction side wake separation region and enhance mixing. The valley flow creates a counter-rotating vortex to the separation vortex, which moves the suction side separation wake upstream. In consequence, the flow stays attached to the blade longer because the valley flow energized the wake region [37].

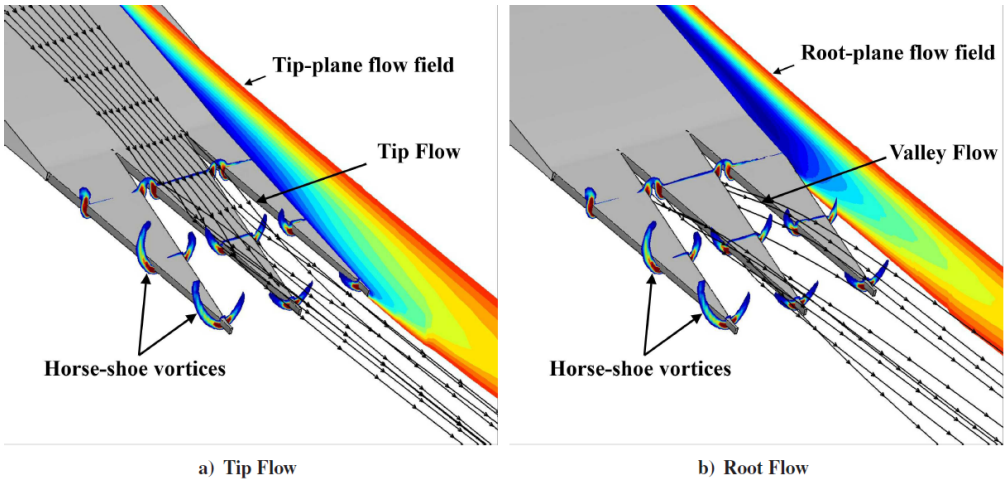

Figure 3.6: RANS simulation results showing a) the tip and b) the root flow field over serrations for a Reynolds number of $Re_c = 3 \cdot 10^5$ [33].

Studies have shown that the wake structure at the suction side decreases with increasing angles of attack (AoA), which suggests that, for axial fans, lower trailing edge noise levels can be reached with high incidence angles and lower speed [33]. Serrations can be seen as features able to generate turbulence to energize unstable flow, thus attenuating the wake. These features can also be applied at leading edges. In order to promote flow attachment to blade surfaces, mid-chord blade structures are usually added with the same main goal of energizing the flow and delaying separation. Results obtained by Gruber *et al.* [34] show that sharp serrations with small angles show the best noise improvement.

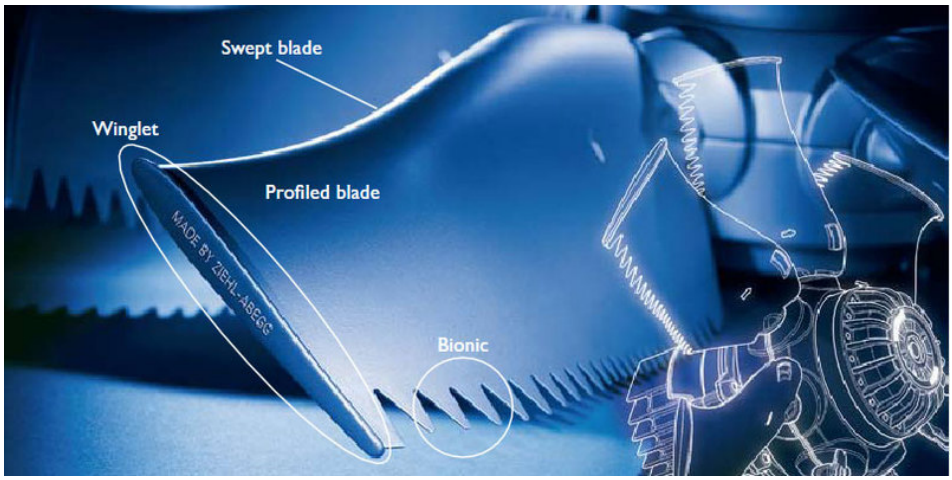

Figure 3.7: Ziehl Abbeg Fe2 Owlet Axial Fan: a commercially available product with several noise reduction features, including serrations at the trailing edge [35].

Another method for reducing trailing edge noise consists in using slots or circular channels that start at the hub corner separation and extend to the trailing edges of the blades. This mechanism seeks to redirect flow from the hub region to the trailing edge wake, this way energizing the wake separation and therefore reducing trailing edge noise. The downside of this method is the increased complexity and cost associated to production ends.

3.2.4 Inlet geometries

Inlet geometries can help to create a more uniform flow at the inlet [36], thus reducing flow fluctuations upstream of the fan. One example, as can be seen in Figure 3.8, is the inlet nose cone.

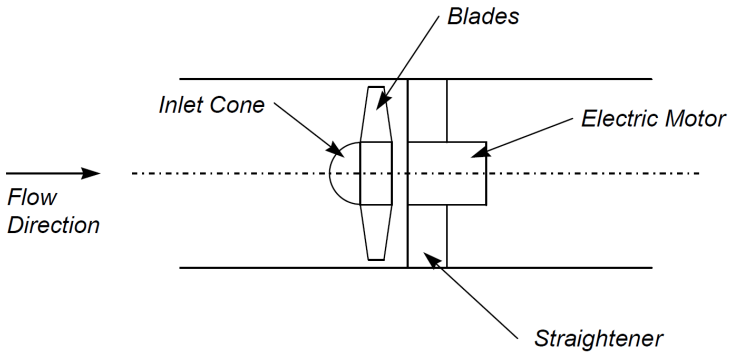

Figure 3.8: Schematic representation of an inlet cone on a shrouded fan [36].

These kind of geometries can be analyzed through design and performance optimization algorithms and can have beneficial effects on both aerodynamic performance and noise levels. Investigations conducted by Derksen and Bender [36] show two types of optimized inlet cones for lowest surface vorticity, which depend on the available space upstream of the fan and its hub-to-tip ratio. Their study shows that short inlet cones

should have a blunt inlet face and a slight hump or rise above the hub radius, while longer inlet cones should have a smooth curved inlet cone with large radius of curvature and no hump, see Figure 3.9.

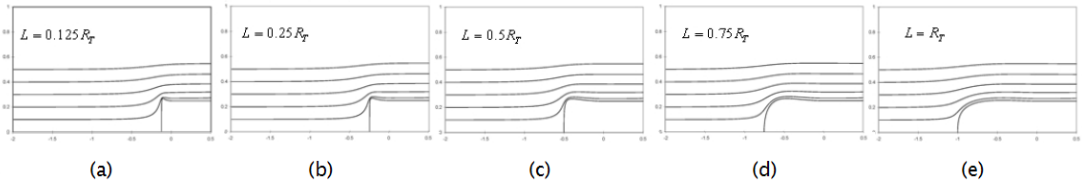

Figure 3.9: Inlet cones geometry as a function of its length. L/R_t represents the non-dimensional hub length, which increases from a) to e), thus the change in the inlet cone's optimal geometry. Adapted from [36].

3.3 Noise Generating Mechanisms

An insight into noise generating mechanisms commonly found in fans can be consulted below, including the causes and built-up of these phenomena.

3.3.1 Vortex Roll- Up

Vortex roll-up is a phenomenon that occurs in fan blades due to the interaction between two flows at the tip clearance region. Because of the axial pressure difference between upstream and downstream flow across the duct, being the pressure at the downstream higher, a reverse tip clearance leakage flow occurs, while a tip clearance vortex occurs in consequence of the radial pressure difference between the blade suction and pressure sides. The tip clearance flow provides this way momentum for the vortex to roll-up. Increased tip clearances are, therefore, prone to induce higher noise levels. Noise is then generated when the vortex roll-up interacts with the shroud and the blade surface itself, due to the dissipation of momentum energy into acoustic energy. This noise type can be found as broadband noise after the first blade passing frequency [37]. The introduction of winglets are a vortex roll-up noise reduction method by reducing the tip vortexes, as mentioned in Chapter 3.2.2.

3.3.2 Blade Loading

Blade loading consists in the blade distribution across the rotor and is a parameter with major influence in fan performance. The degree of blade loading also influences noise whilst influencing vorticity production, due to the difference in pressure across and over the blade [37]. Blade loading which minimizes radial outflow decreases tip region turbulence and the formation of vortexes, that being the main reason behind forward skewed blades being best for quieter fans, as mentioned in Chapter 3.2.1.

3.3.3 Vortex Shedding

Suction side flow separation from the blade surface can happen due to the formation of unstable wake structures. The condition of minimum flow at which the amount of suction side separation becomes inoperable is known as Aerodynamic Stall, and has a

considerable influence on noise due to the pressure fluctuations and the unstable wake. Therefore, minimizing the wake by maximizing flow stability also minimizes noise.

In regard to axial fans, aerodynamic stall can be a problem if the amount of suction side separation flow creates this unstable wake structure. This condition can be reached if the minimum flow rate requirements to avoid stall are not met, which leads to assume that aerodynamic stall is more likely to happen at lower rotational fan speed. At higher flow rates, the suction side separation is minimized, which minimizes the wake and consequently reduces noise generation, even though higher fan speed is required [37].

Thus, flow separation noise reduction methods seek to induce favorable changes in the flow in order to support flow attachment, usually by introducing features to energize the wake structure.

Vortex shedding is a phenomenon that occurs when obstacles to the flow path interact with the flow layer, generating vortexes that can interact with other instabilities further downstream. Obstacles to the flow can be solid edges or pressure differentials that induce sudden expansion to the fluid. In axial fans, vortex shedding can occur due to instabilities in the laminar flow layer on the suction side of the blades [38], given the low fluid momentum at the separation region, and due to the flow interaction with blunt edges (for example, trailing and leading edges). Both scenarios generate vortex shedding and consequently turbulence and noise.

Blade designs which seek to reduce the vortex shedding noise usually introduce serrations or structures at the mid-chord, leading or trailing edge, to turn the laminar layer into a turbulent region, preventing or delaying wake separations as mentioned in Chapter 3.2.3.

3.3.4 Hub Corner Separation

When the inlet flow reaches the hub region of a fan, it finds a blockage at the motor surface and abrupt changes occur in its velocity directions and magnitude. The fan leading edge suffers therefore different levels of flow incidence. This flow block can eventually result in flow separation and vortexes due to the flow interactions and therefore higher levels of noise. Fan blade designs typically take this factor into account by supporting different layers with different Angles of Attack (AoA) from hub to tip region. [37]

The Ebm-papst fans currently used in the heat pump units are designed by the manufacturer taking into account the fan blade design, the fan hub and the motor altogether. The characteristic high AoA of the blade root near the hub is believed to help directing the flow onto the blade with a smoother transition. Inlet geometries, such as cone inlet noses, can improve hub corner separation flow, as explained in chapter 3.2.4.

3.4 Fan Affinity Laws

Affinity laws can be used to evaluate fan performance for given changes in the fan speed and wheel diameter, namely its flow rate, static pressure drop and power consumption. For this investigation, the fan affinity laws were of great importance by enabling starting points for iterative analysis, as will be explained in Chapter 4.

The general fan laws for volume flow capacity $[m^3 \cdot s^{-1}]$, static pressure drop $[Pa]$ and power $[W]$ can be observed in equations (3.5) to (3.7).

$$\frac{q_1}{q_2} = \frac{n1}{n2} \cdot \left(\frac{d_1}{d_2}\right)^3 \tag{3.5}$$

where q represents volume flow $[m^3 \cdot s^{-1}]$, n the rotational speed $[rpm]$ and d the fan's outer diameter $[m]$;

$$\frac{\Delta p_1}{\Delta p_2} = \left(\frac{n1}{n2}\right)^2 \cdot \left(\frac{d_1}{d_2}\right)^2 \tag{3.6}$$

where Δp stands for static pressure $[Pa]$;

$$\frac{P_1}{P_2} = \left(\frac{n1}{n2}\right)^3 \cdot \left(\frac{d_1}{d_2}\right)^5 \tag{3.7}$$

where P denotes power $[W]$. Given the three equations, it becomes possible to analyze the impact that a change in diameter or in fan speed can have on the above stated operating parameters.

3.4.1 Fan Diameter Effect

For a constant rotational speed, the performance impact for a change in the fan diameter can be evaluated using equations (3.8) to (3.10).

$$\frac{q_1}{q_2} = \left(\frac{d_1}{d_2}\right)^3 \tag{3.8}$$

$$\frac{\Delta p_1}{\Delta p_2} = \left(\frac{d_1}{d_2}\right)^2 \tag{3.9}$$

$$\frac{P_1}{P_2} = \left(\frac{d_1}{d_2}\right)^5 \tag{3.10}$$

An increase in fan diameter therefore boosts mostly airflow and input power. Overall pressure drop changes in a quadratic proportion to fan speed, which, in the acoustic perspective, could lead to an increase of the sound pressure level.

3.4.2 Rotor Speed Effect

For a constant fan diameter, a change in the rotor speed affects fan performance as shown by equations (3.11) to (3.13).

$$\frac{q_1}{q_2} = \frac{n_1}{n_2} \tag{3.11}$$

$$\frac{\Delta p_1}{\Delta p_2} = \left(\frac{n_1}{n_2}\right)^2 \tag{3.12}$$

$$\frac{P_1}{P_2} = \left(\frac{n_1}{n_2}\right)^3 \tag{3.13}$$

By observation of the above listed equations, a change in rotor velocity has its highest impact on the fan power consumption and its lowest on the airflow rate.

3.4.3 Non-dimensional Correlation between Tip Speed and Diameter Increase

Considering the fan affinity laws and the tip speed formula, it is possible to use non-dimensional analysis to derive a metric correlation between diameter increase of the fans and its influence on the tip speed, given the necessary rotation speed to deliver the same airflow.

Forcing the airflow to be constant, Equation (3.5) becomes Equation (3.14), as:

$$1 = \frac{n_1}{n_2} \cdot \left(\frac{d_1}{d_2}\right)^3 \equiv \frac{n_2}{n_1} = \left(\frac{d_1}{d_2}\right)^3 \tag{3.14}$$

Equation (3.15) represents the tip speed T in $[m/s]$ as a function of radius r and rotation speed rpm,

$$T = \frac{rpm \cdot 2r \cdot \pi}{60} \tag{3.15}$$

Consider t_1 and t_2 to be the tip speed before and after the diameter increase. The output from Equation (3.14), namely n_2, and the changes in fan diameter d_2 can this way serve as input to calculate the variations in tip speed according to the rpm. $2r$ corresponds therefore to d_2 and rpm to n_2.

Considering a non-dimensional analysis, the Equations can be written as:

$$\frac{n_2}{n_1} = \left(\frac{d_2}{d_1}\right)^{-3} \tag{3.16}$$

$$\frac{t2}{t1} = \frac{\left(\frac{n2}{n1}\right) \cdot \left(\frac{d2}{d1}\right) \cdot \pi}{60} \tag{3.17}$$

For demonstration purposes, consider d_1 as 1, n_1 as 100 and variations of d_2 from 1 to 2, in increments of 0,2. The non-dimensional curve of the new rotational speed $\left(\frac{n_2}{n_1}\right)$ and the fan's tip speed $\left(\frac{t_2}{t_1}\right)$ as a function of the diameter increase $\left(\frac{d_2}{d_1}\right)$ can this way be obtained. See Figure 3.10.

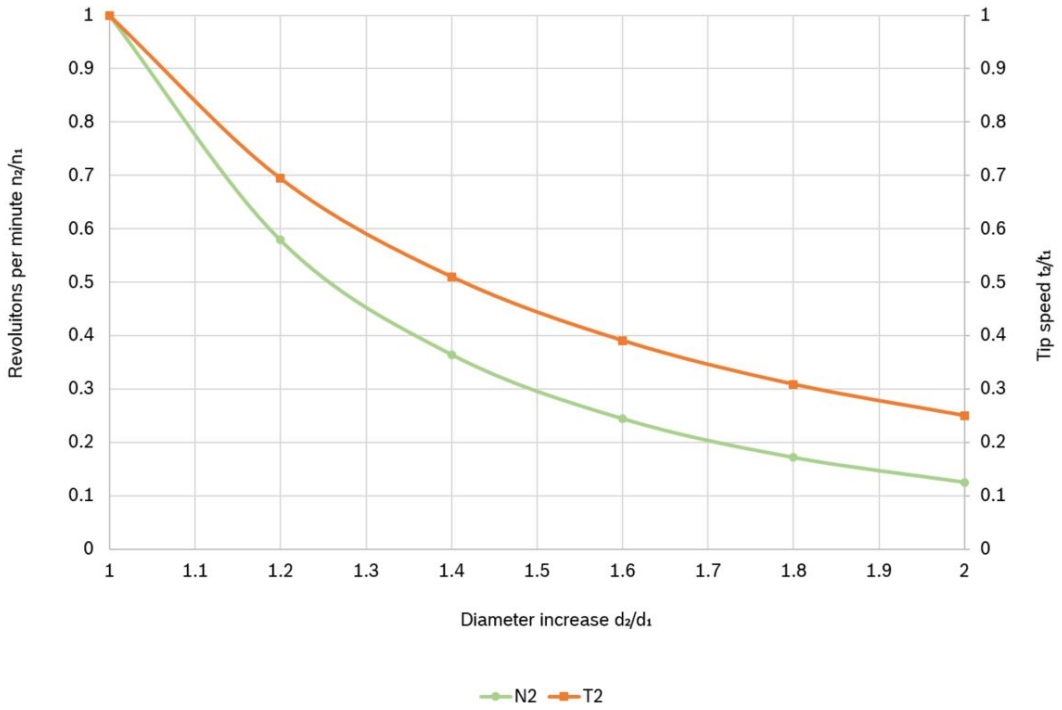

Figure 3.10: Non-dimensional curves of revolutions per minute and tip speed of an axial fan as a function of its diameter increase.

From the chart, it becomes clear how the relation between diameter variation and rotational fan speed, which scales to the power of three, influences the tip speed's linear dependency of *rpm* and fan diameter. It's possible to see that the highest impact on rotational speed reduction is accomplished within the first 25% of diameter increase, reaching half of the initial *rpm*. The tip speed, although showing a linear dependency with fan *rpm* and diameter in its mathematical formulation, benefits in a non-linear way with a diameter increase that suits airflow requirements, due to the *rpm*'s non-linear curve behavior (green curve) that serves as input.

Chapter 4

Diameter and Tip Speed Analysis

4.1 Case Studies: Variations in Fan Diameter to Fit in Chassis

As mentioned before, the fan speed contributes greatly to aerodynamic noise. In this chapter, the influence of the fan diameter and its tip speed will be analyzed by comparing the two Ebm-papst fans adapted to fit both of the heat pump chassis produced by Bosch.

As a first approach, four case studies were analyzed:

- Case 1: ⌀630 mm Fan in mid-chassis
- Case 2: ⌀500 mm Fan in small-chassis
- Case 3: ⌀630 mm Fan reduced to ⌀500 mm in small-chassis
- Case 4: ⌀500 mm Fan amplified to ⌀630 mm in mid-chassis

The goal was to compare Case 1 with Case 4 and Case 2 with Case 3, respectively, and to evaluate the different geometries of the blades' influence on noise. Two different simulation environments were used: the ⌀630 fans in the mid-chassis heat pump unit and the ⌀500 fans inserted in the small-chassis unit. Both fans can be seen in Figure 4.1. The heat pumps operate between a range of fan rotational velocities comprised between 500 and 720 revolutions per minute. Noise evaluation was therefore performed for both limits of the range: the low speed mode (500 rpm) and the high speed mode (720 rpm). A diagram of the simulation workflow can be found in the Appendix A. All four case studies were modeled and analyzed using the same pre- and post-processing conditions, which are described in detail within the next chapters.

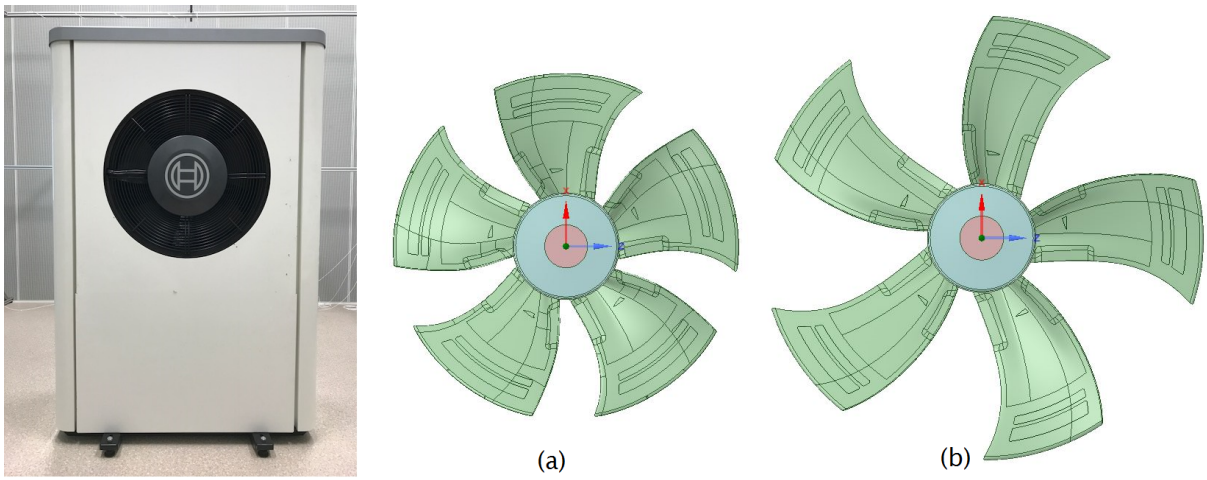

Figure 4.1: Bosch AirX heat pump external unit which comprises one of two different fans according to its capacity a) ⌀500 fan for small-chassis and lower capacity ranges b) ⌀630 fan for mid-chassis and higher ranges. Note the different blade shapes.

4.1.1 CFD models

Fluent 19.0 is a commercially available CFD code which, in recent years, adopted two algorithms to account for aerodynamic noise: the Broadband Noise Source (BNS) model and the Ffowcs Williams-Hawkings (FW-H) Equations. Fluent 19.0 was used to predict the aerodynamic noise caused by the interaction between airflow and solid surfaces. Meshes were generated using Ansys Meshing and Ansys Fluent was used as the CFD solver and post-processor, alongside CFD-Post.

The simulation scenario consisted of an evaporator, a connection chamber, an outlet domain and a shrouded axial fan. Similar boundary and cell zone conditions were applied to all cases, where changes lie only within the given angular velocity of the fans.

The evaporator was simulated as a porous medium with given inertial and viscous resistance values provided by Bosch. Those values, listed in Table 4.1, are the result of previous simulation work performed by the company. The evaporator will induce a pressure drop on the airflow in consequence of the increased velocity gradient and the associated shear stresses around its tubes.

Table 4.1: Evaporator Inertial and Viscous Resistance (data provided by Bosch).

	Direction x	Direction y	Direction z
Viscous Resistance $[1/m^2]$	6142650	2860910	2125990
Inertial Resistance $[1/m]$	273,85	230,83	181,70

Geometry

A schematic representation of the four case studies can be seen in Figure 4.2.

Note that the small- and mid-chassis have distinct evaporator sizes, accounting for

the heating power offered by each model. The small-chassis accounts for a tip clearance of 3 mm while the mid-chassis shows a slightly increased clearance of 5,5 mm.

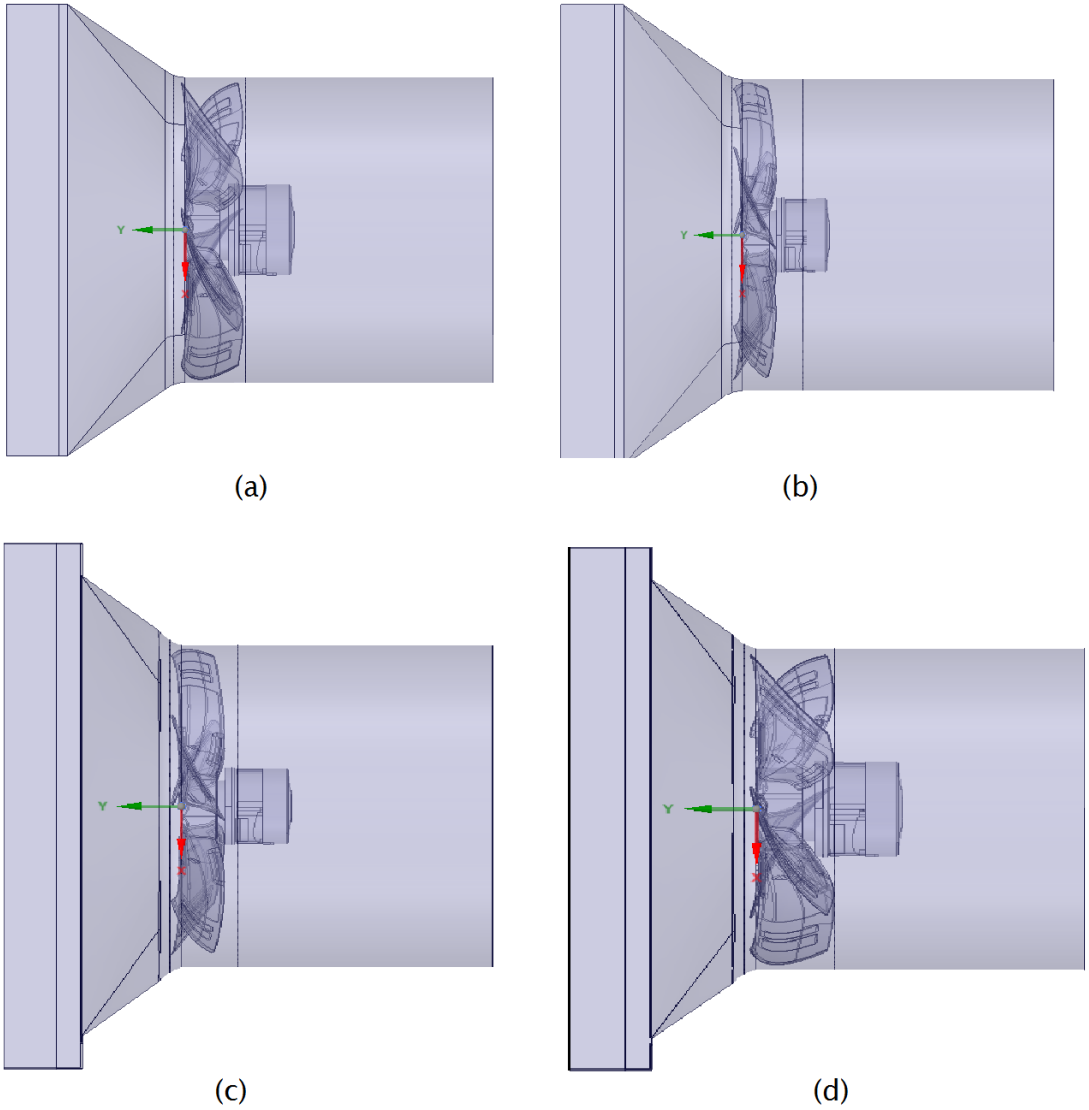

Figure 4.2: CFD model setup using the heat pump environment a) ⌀500 fan in small-chassis b) ⌀630 fan reduced to 500 mm in small-chassis c) ⌀630 fan in mid-chassis d) ⌀500 fan amplified to 630 mm in mid-chassis.

Mesh

Due to the high complexity of the blade design, a compromise between mesh quality and element statistics was established. Despite accessibility to the Bosch High Performance Computer (HPC) Cluster for job submissions, the number of elements were kept lower than 10 million due to an eventual risk of compromising post-processing capabilities. As mentioned before, Ansys Meshing was used for mesh generation.

The elements' orthogonal quality was the mesh metric used for quality control and

an orthogonality minimum value of 0,1 was established to be the ideal mesh target.

The proximity and curvature size function was used for good element flexibility.

The curvature normal angle was set to 4°to capture the blade surface's sweeps and the defeaturing option was enabled for quality reasons.

A conformal mesh with tetrahedral elements was applied to all domains, as can be seen in the example shown in Figure 4.3.

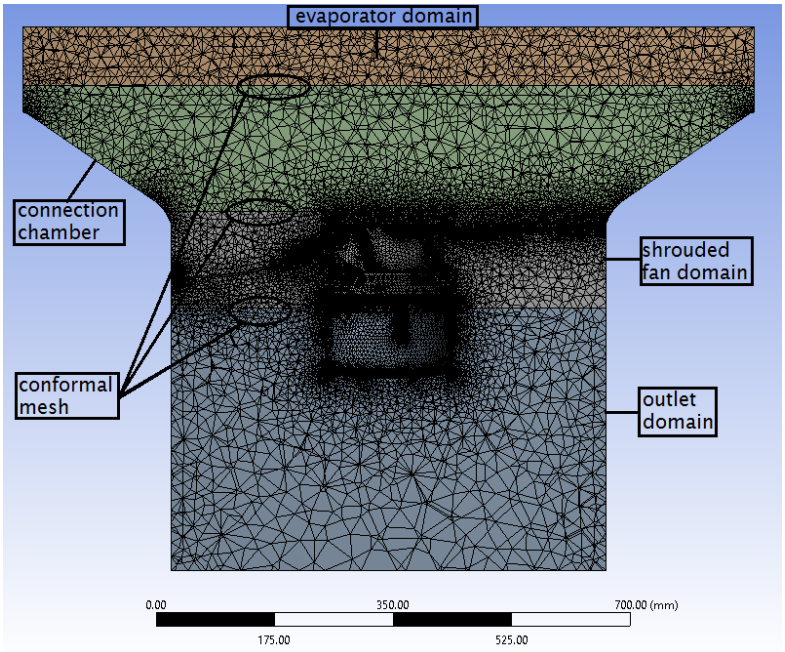

Figure 4.3: Section view of the conformal, tetrahedral mesh for the small-chassis with the reduced ⌀630 fan model.

The minimum and maximum size of the elements as well as the defeature and the proximity size were optimized for each case in order to obtain the best possible mesh quality. The statistics of each model's mesh alternates between 4 and 4,5 million elements.

Turbulence Model

There are several turbulence models implemented in commercial CFD codes. Common ones are the Reynolds-Averaged-Navier-Stokes (RANS) model and the Large Eddy Simulation (LES) model; but there is no general agreement concerning which one is the best. It is of the responsibility of the CFD engineer to choose the best suited for each scenario. For this investigation, the Transition SST model was used and further information on its behavior is hereafter described.

Transition SST Model

This model is based on the Langtry-Menter 4-Equation Transitional SST model, as described in Langtry and Menter's [39] and in Menter, Langtry and Volker's [40] studies. This algorithm is known for its ability to capture the flow characteristics in its transition

from laminar to turbulent behavior. It is a combination of SST $K-\omega$, coupled with intermittency γ and transition onset Reynolds number. Re_θ is the critical Reynolds number where the intermittency starts. Four transport equations are solved, two of them being:

$$\frac{\partial}{\partial t}(\rho k) + \frac{\partial}{\partial x_i}(\rho k u_i) = \frac{\partial}{\partial x_j}\Big(\Gamma_k \frac{\partial k}{\partial x_j}\Big) + G_k - Y_k + S_k \tag{4.1}$$

$$\frac{\partial}{\partial t}(\rho \omega) + \frac{\partial}{\partial x_j}(\rho \omega u_j) = \frac{\partial}{\partial x_j}\Big(\Gamma_\omega \frac{\partial \omega}{\partial x_j}\Big) + G_\omega - Y_\omega + D_\omega + S_\omega \tag{4.2}$$

where ρ, k and ω represent flow density, turbulent kinetic energy and specific dissipation; G_ω and G_k represent the generation of turbulent kinetic energy and the specific dissipation rate; Γ_ω and Γ_k denote the flow diffusivity, Y_ω and Y_k correspond to dissipation and S_ω and S_k to source terms. D_w is an extra cross diffusion term. The second pair of equations,

$$\frac{\partial(\rho\gamma)}{\partial t} + \frac{\partial \rho U_j \gamma}{\partial x_j} = P_x\gamma 1 - E_{\gamma 1} + P_{\gamma 2} - E_{\gamma 2} + \frac{\partial}{\partial x_j}\Big[\Big(\mu + \frac{\mu_t}{\sigma_\gamma}\Big)\frac{\partial \gamma}{\partial x_j}\Big] \tag{4.3}$$

$$\frac{\partial(\rho R\bar{e}_{\theta t})}{\partial t} + \frac{\partial(\rho U_j R\bar{e}_{\theta t})}{\partial x_j} = P_{\theta t} + \frac{\partial}{\partial x_j}\Big[\sigma_{\theta t}(\mu + \mu_t)\frac{\partial R\bar{e}_{\theta t}}{\partial x_j}\Big] \tag{4.4}$$

correspond to the equations for intermittency γ and transition momentum thickness Reynolds number $R\bar{e}_{\theta t}$, where U corresponds to velocity, P to additional crossflow instabilities, μ to the molecular dynamic viscosity and E relates to an empirical correlation regarding the length of the transition region. Further information on these equations can be found in literature [39; 40].

Aeroacoustic Model

Lighthill came forward to lay the mathematical ground work behind the theory of aeroacoustics. An extension to Lighthill's acoustic analogy was later introduced by Curle, by explaining the effect of boundary layer flows and showing that boundary terms can provide effective mass and momentum injection into the main flow, and that these phenomena acoustically represent dipole sources. Aeroacoustic noise algorithms are currently implemented in Fluent 19.0. The Broadband Noise Source (BNS) model consists of several different models which should be used for specific purposes. In this investigation, the Boundary Layer Noise Source model was used. The other available models, such as Proudman's Formula and the Jet Noise Source model weren't used due to their limitations; the first model requires isotropic turbulence to provide proper results and the second one is limited to axisymmetric jet models.

Broadband Noise Source (BNS) - Boundary Layer Noise Source model

The Boundary Layer Noise Source model aims to identify sound generated by turbulent boundary layer flow over solid surfaces at low Mach numbers [41]. The surface acoustic power is calculated based on Curle's integral, and accounts for the local contribution from the body surface to the total acoustic power based on the turbulent

boundary flow. The total acoustic power emitted from the body surface can, therefore, be computed from Equation (4.5)

$$P_A = \frac{1}{\rho_0 a_0} \int_0^{2\pi} \int_0^{\pi} \overline{p'^2} r^2 d\theta d\psi \tag{4.5}$$

where $\overline{p'^2}$ represents the sound intensity, ρ_0 denotes fluid density, a_0 the sound velocity, $r \equiv |\overrightarrow{x} - \overrightarrow{y}|$ and θ consists in the angle between $|\overrightarrow{x} - \overrightarrow{y}|$ and the wall-normal vector $\overrightarrow{n}$. Equation (4.5) is an extension made to Lighthill's general theory of aerodynamic sound in order to incorporate the influence of solid boundaries upon the sound field. The mathematical deduction of Equation (4.5) can be found in literature [42]. Fluent 19.0 can report the surface acoustic power defined by Equation (4.5) in W/m^2 or in dB units, by applying Equation (4.6).

$$L_p = 10 \log \left(\frac{P_A}{P_{ref}} \right) \tag{4.6}$$

where P_{ref} represents the reference acoustic power, defined as 10^{-12} W/m^2. Fluent 19.0 also enables to calculate the area-weighted average of a quantity using a surface integral. This integral is computed by summing the product of the field variable ϕ and the facet area A_i, where each facet i is associated with a cell in the domain, in a total of n cells. The area-weighted average is then computed by dividing the summation of the product by the total area of the surface A [41], as expressed in Equation (4.7).

$$\frac{1}{A} \int \phi dA = \frac{1}{A} \sum_{i=1}^{n} \phi_i |A_i| \tag{4.7}$$

Equation (4.7) was used to evaluate the area-weighted average of the Surface Acoustic Power Level, which represents the average Acoustic Power Level of the boundary layer noise on the entire surface of the fan, represented in dB.

4.1.2 Iterative Process for Airflow Requirement

To guarantee a fair aerodynamic noise comparison between the aforementioned case studies, it was important to assure the same airflow rate for each model. This way, the primary effect of the fan, its heat removing capability, remains equal. The adequate fan speed was adjusted for each model using Equation (3.11), the fan affinity law which states the direct correlation between wheel speed and airflow, given a constant fan diameter.

Using the airflow from the original fan models as the target values for both low speed and high speed modes, the rotation speed (rpm) of the re-scaled models were adjusted in order to meet those same airflow requirements. As a first iteration, 500 and 720 rpm were used. Although the ⌀500 fan displays larger blades and can, therefore, move more air in a given time frame, the ⌀630 fan has a larger diameter. Therefore, for the same speed, it is expected to see a higher airflow rate for the ⌀630 fan model. Results are presented in Chapter 4.1.3.

4.1.3 Results

The obtained results for the original and the re-scaled fans at adjusted speeds are listed in Table 4.2.

Table 4.2: Operating points and surface Acoustic Power Level (SWL) for the original and re-scaled fans at low and high speed modes.

Fan	$\varnothing[mm]$	**velocity** $[rpm]$	**Airflow** $[m^3/h]$	**Pressure Drop** $[Pa]$	**Tip Speed** $[m/s]$	**Area Avg. SWL** $[dB]$	**Max. SWL** $[dB]$
500 fan	500	500	1825,2	20,8	13,1	40,1	63,1
	500	720	2635,2	43,7	18,9	47,9	73,8
630 r*	500	572	1814,4	21,6	15,0	41,4	65,1
	500	804	2660,4	41,6	21,0	49,2	73,5
630 fan	630	500	3196,8	23,0	16,5	42,9	69,9
	630	720	4723,2	44,8	23,8	50,7	78,4
500 a*	630	480	3200,4	30,2	15,8	44,3	68,1
	630	721	4716,0	66,8	23,8	53,4	81,3

r* - denotes reduced (630 to 500) and a* - amplified (500 to 630)

The flow behavior of these models can be evaluated by analyzing a centered section view, as presented in figures 4.4 to 4.7. These images show a) how the velocity increases towards the fan due to the connection chamber's decreasing section area and, as stated by the Bernoulli Principle, as a consequence there is an associated decrease in static pressure, visible in images e). As previously mentioned, the evaporator induces a pressure drop in the airflow due to the shear stresses manifested along the finned tubes, which is also visible in the pressure contours. The y-velocity contours, images b), expose positive y-directed flow downstream of the fan, thus revealing the existence of reverse flow towards the fan hub. The small-chassis cases show increased pressure at the outlet domain walls when compared to the mid-chassis models.

This analysis also enabled to identify the critical boundary layer noise regions of the fans. Figures 4.8 and 4.9 show how the aerodynamic noise is most critical on the suction side's upper span regions of the fans. The winglet, the blade tip and some extend of the leading and trailing edge are also areas of considerable noise source.

From Table 4.2 and Figure 4.8, it is possible to observe that reducing the $\varnothing$630 fan model to 500 mm implies higher average and maximum SWL levels on the fan blades than the original $\varnothing$500 fan. The need to adjust the fan speed for airflow requirements generates higher tip speed velocities and therefore more turbulence on the critical winglet region (Figure 4.10). In the case of amplifying the $\varnothing$500 fan to 630 mm, although the re-scaled model shows a lower maximum surface SWL level, the average value is higher than for the original $\varnothing$630 fan; observing Figure 4.9, it is possible to see that the $\varnothing$630 fan reveals a higher dB level at its tip region than the re-scaled model, but it is evident that this higher noise level region is more localized in comparison to the re-scaled fan. Although rotating at lower speed, the amplified fan is predicted to have higher sound emissions of aerodynamic source in the far-field. Note that the contours of each fan blades differ from each other due to the assymmetry of the connection chamber, which influences the inlet airflow conditions.

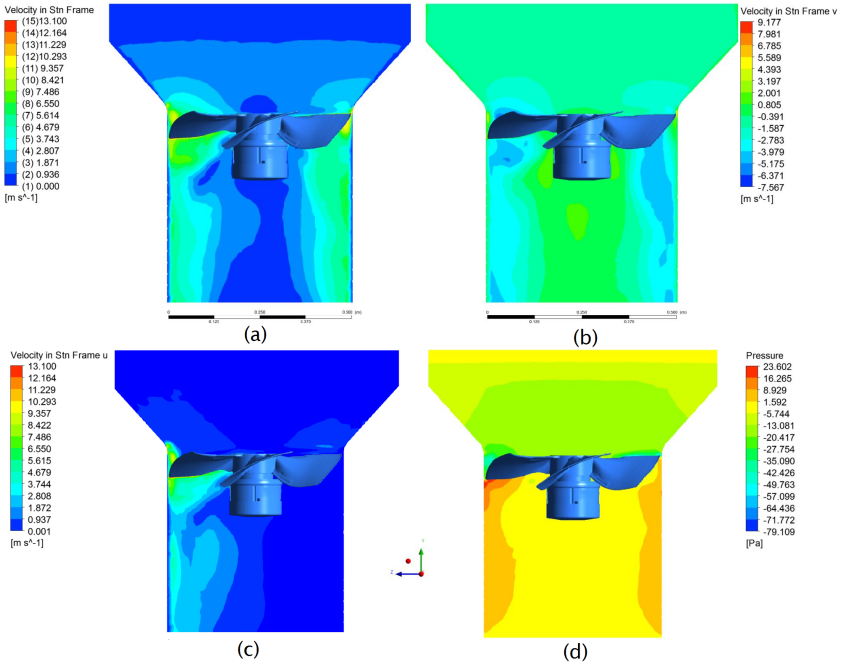

Figure 4.4: Velocity and Pressure contours at central section view of the small-chassis with the $\varnothing 500$ fan at 500 rpm a) velocity magnitude m/s b) Y-directed (axial) velocity m/s c) X-directed (radial) velocity m/s d) static pressure Pa.

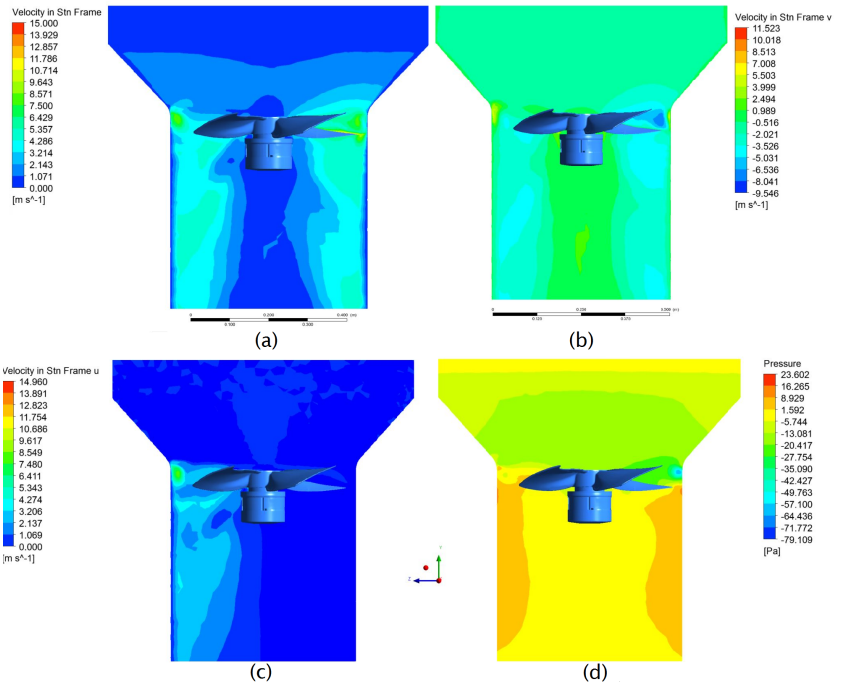

Figure 4.5: Velocity and Pressure contours at central section view of the small-chassis with the reduced $\varnothing 630$ fan at 572 rpm a) velocity magnitude m/s b) Y-directed (axial) velocity m/s c) X-directed (radial) velocity m/s d) static pressure Pa.

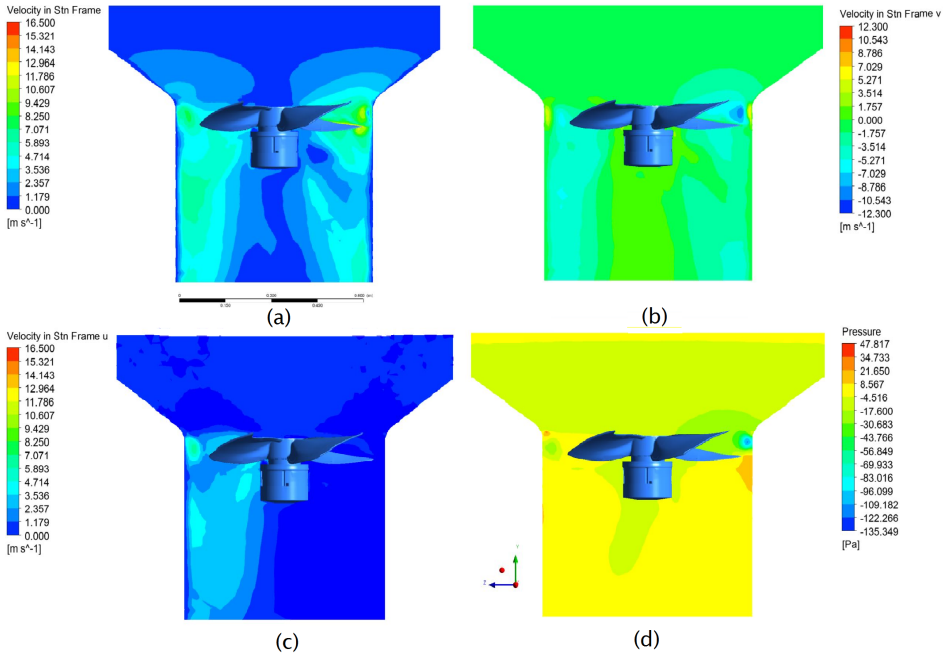

Figure 4.6: Velocity and Pressure contours at central section view of the mid-chassis with the ⌀630 fan at 500 rpm a) velocity magnitude m/s b) Y-directed (axial) velocity m/s c) X-directed (radial) velocity m/s d) static pressure Pa..

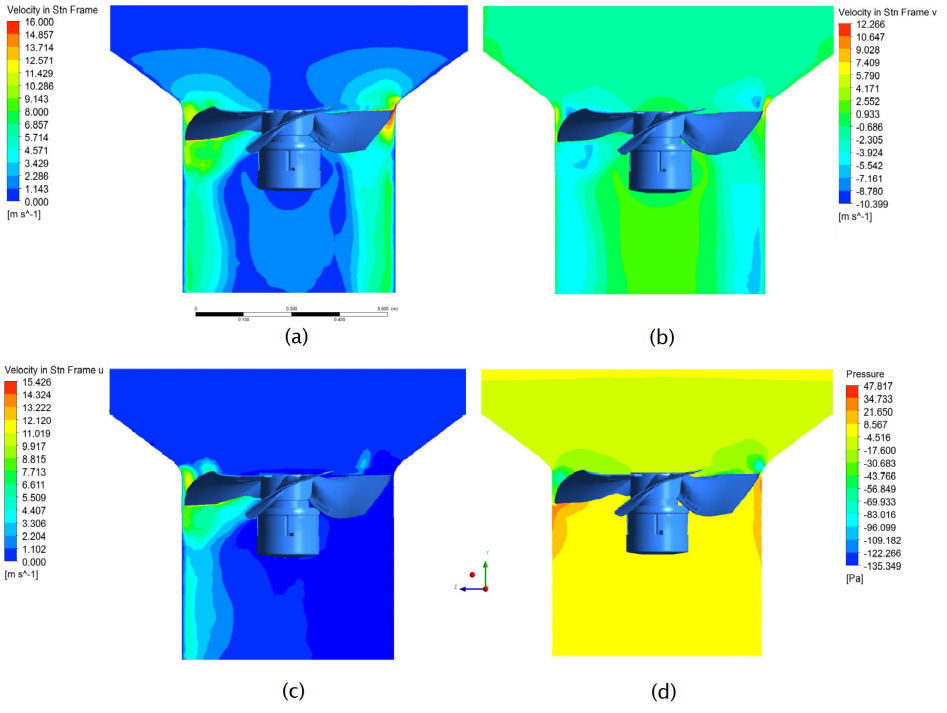

Figure 4.7: Velocity and Pressure contours at central section view of the mid-chassis with the amplified ⌀500 fan at 480 rpm a) velocity magnitude m/s b) Y-directed (axial) velocity m/s c) X-directed (radial) velocity m/s d) static pressure Pa.

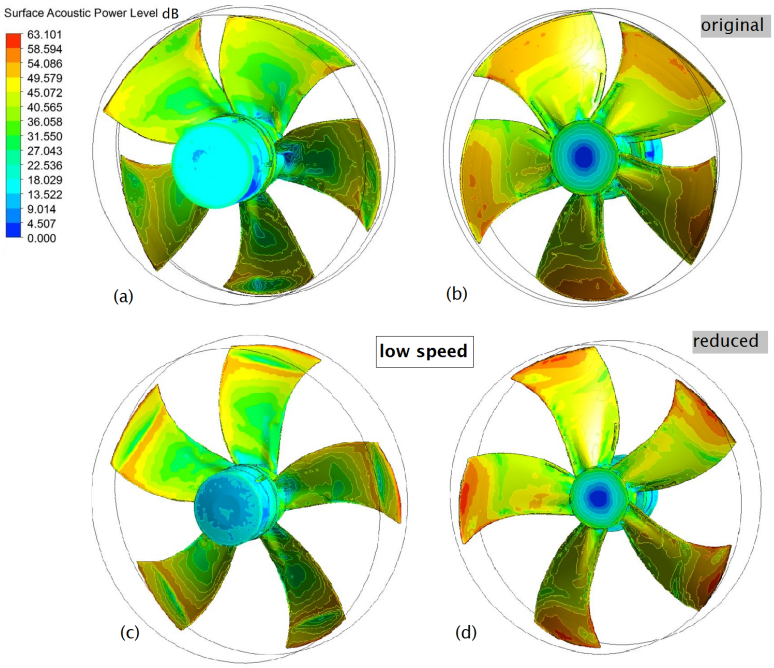

Figure 4.8: Surface Acoustic Power Level contours at a) original ⌀500 fan pressure side b) original ⌀500 fan suction side c) reduced ⌀630 fan pressure side d) reduced ⌀630 fan suction side; fan speed 500 *rpm* for a) and b) and 572 *rpm* for c) and d).

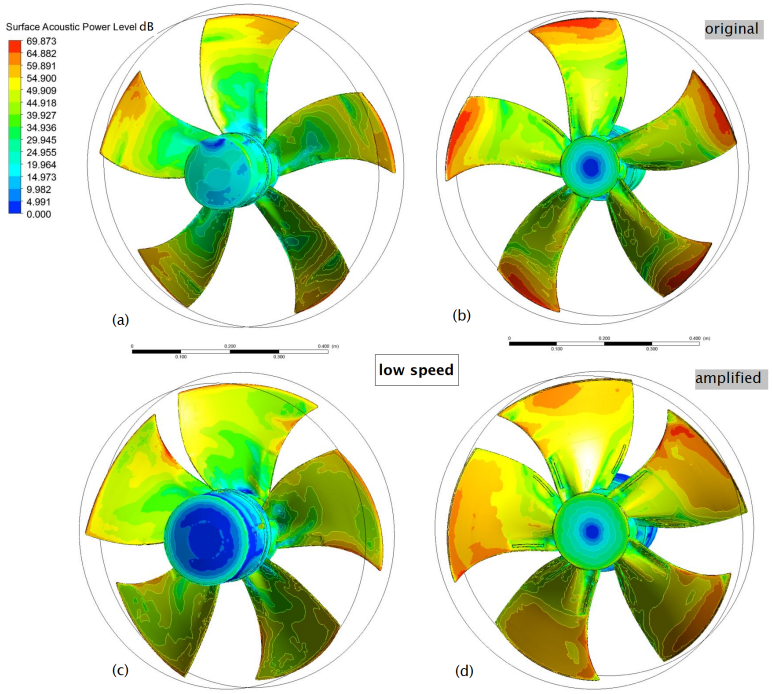

Figure 4.9: Surface Acoustic Power Level contours at a) original ⌀630 fan pressure side b) original ⌀630 fan suction side c) amplified ⌀500 fan pressure side d) amplified ⌀500 fan suction side; fan speed 500 *rpm* for a) and b) and 480 *rpm* for c) and d).

The turbulent kinetic energy can be observed in figures 4.10 and 4.11. Turbulence appears to shift slightly from the winglet area on the ⌀630 fans' blade shaped models to the tip and leading edge on the models based on the ⌀500 fan.

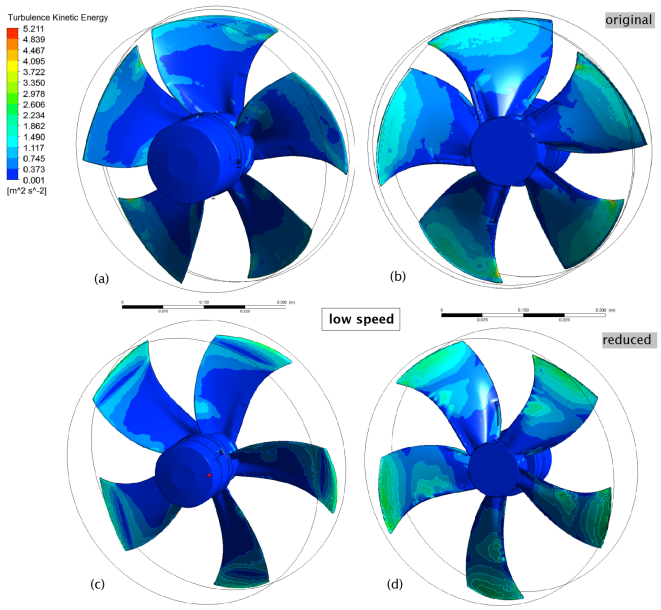

Figure 4.10: Turbulent Kinetic Energy contours at a) original ⌀500 fan pressure side b) original ⌀500 fan suction side c) reduced ⌀630 fan pressure side d) reduced ⌀630 fan suction side; fan speed 500 *rpm* for a) and b) and 572 *rpm* for c) and d).

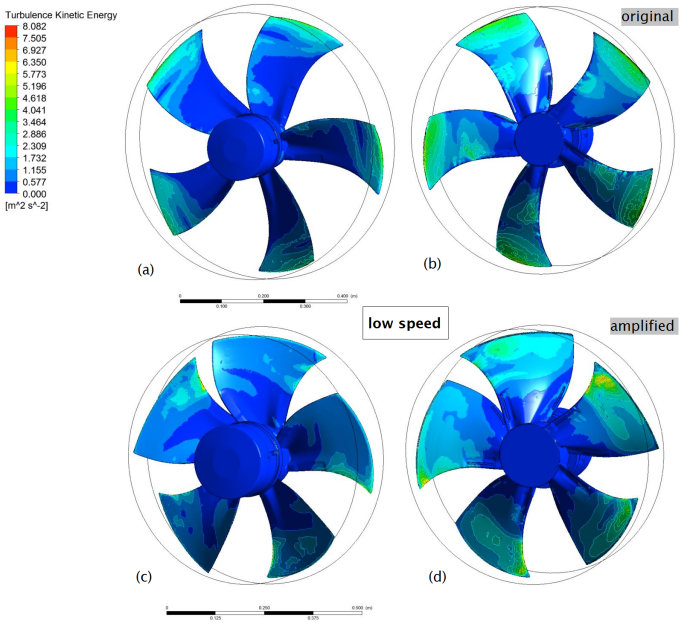

Figure 4.11: Turbulent Kinetic Energy contours at a) original ⌀630 fan pressure side b) original ⌀630 fan suction side c) amplified ⌀500 fan pressure side d) amplified ⌀500 fan suction side; fan speed 500 *rpm* for a) and b) and 480 *rpm* for c) and d).

Using CFD-Post, the streamline velocity profiles were plotted for the original fans, to better understand the generation of turbulence in the rotating flow. In figures 4.12 and 4.13 , the original ⌀500 *mm* and ⌀630 *mm* fans' streamlines reveal how the interaction between the incoming flow and the energized, rotating flow generates small-scale turbulent vortexes near the upper area of the suction side. These vortexes, more predominant for the ⌀630 model due to its increased diameter, generate turbulence in the boundary layer flow. The vortex generating areas match the most turbulent regions shown in figures 4.10 and 4.11.

It is also possible to visualize reverse tip leakage flow in the tip clearance, likely due to the pressure differential between the pressure and the suction sides of the blade (see images e) and f) of both figures). The reverse tip leakage phenomenon is steeper on the ⌀630 fan, due to its increased tip clearance. As discussed in Chapter 3.3.1, increased tip clearances are in general associated with higher noise emissions. This reverse tip leakage gathers momentum and forms a visible and well defined vortex which rolls-up near the winglet and generates turbulence overall in the suction side upper area of the blade.

Reverse leakage near the motor is also visible in both cases due to the pressure differential between upstream and downstream of the fan (see images d) of figures 4.4 and 4.6). This phenomenon reveals itself mostly in the ⌀500 fan model, since the outlet airflow domain has a smaller diameter in the small-chassis than in the mid-chassis. For the same airflow, the forwards directed flow creates more pressure on the outlet walls of the small-chassis, which contributes to increased pressure differentials and more reverse flow.

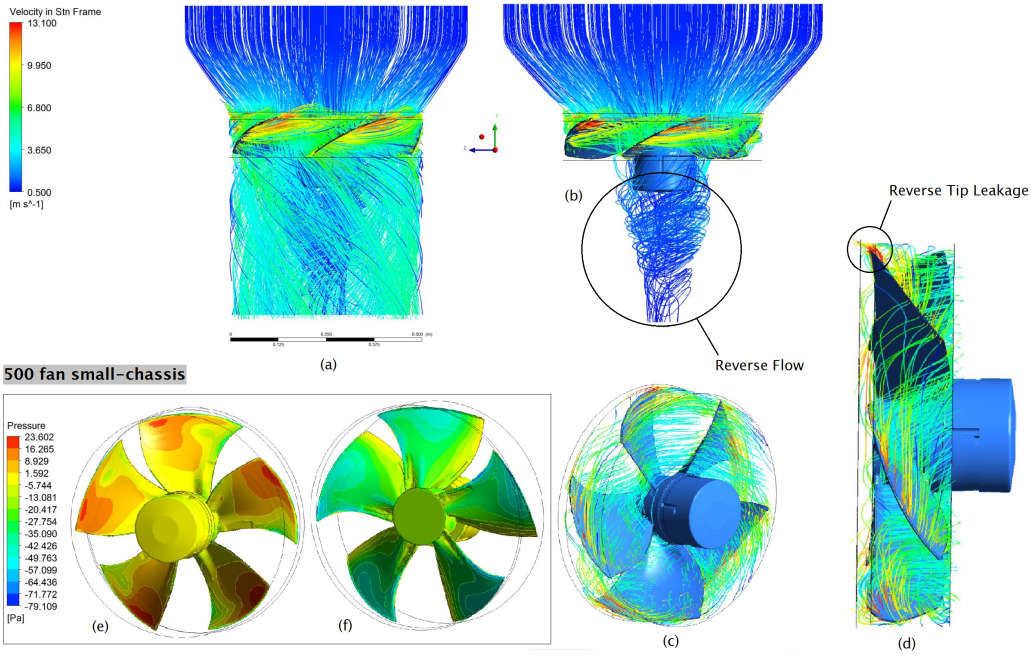

Figure 4.12: Velocity streamlines ⌀500 fan in small-chassis at 500 *rpm* a) entire model b) backwards directed flow relatively to the fan c) rotating flow domain near the fan, revealing some turbulent zones d) profile view of rotating airflow revealing reverse tip leakage e) fan pressure side pressure contour f) fan suction side pressure contour.

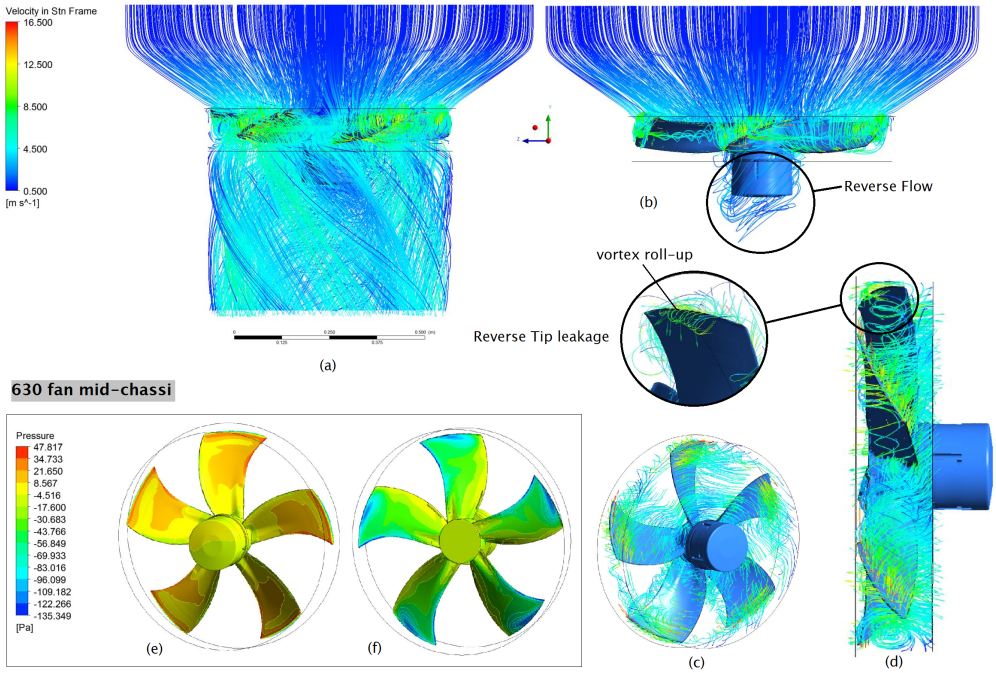

Figure 4.13: Velocity streamlines ⌀630 fan in mid-chassis at 500 *rpm* a) entire model b) backwards directed flow relatively to the fan c) rotating flow domain near the fan, revealing major turbulent zones d) profile view of rotating airflow revealing reverse tip leakage e) fan pressure side pressure contour f) fan suction side pressure contour.

The results depicted in figures 4.4 to 4.13 were obtained for the low speed condition. It was observed tat those results present a similar distribution for the high speed mode, presenting a higher magnitude, as expected (Table 4.2). Therefore, the contour plots are omitted. As a final remark, Figure 4.14 presents a plot of airflow $[m^3/h]$ and average surface acoustic power level $[dB]$ of the four case studies and in Figure 4.15 the respective operating points can be observed.

When plotting the average surface acoustic power level as a function of airflow, as shown in Figure 4.14, it becomes clear that amplifying or reducing the original fans results in higher boundary layer noise on the fan's surfaces, while also changing the fan's operating point by influencing the pressure drop across the fan, see Figure 4.15.

These plots summarize the obtained results by exposing the negative impact that a re-scaled fan would have on both the small- and -mid-chassis unit.

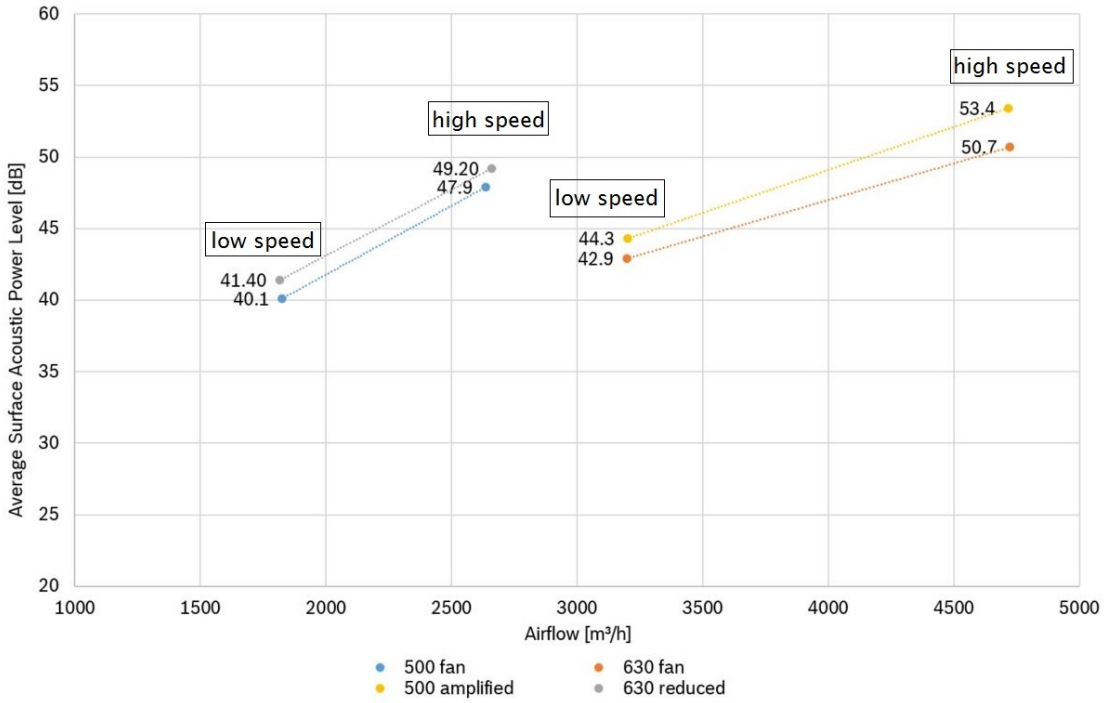

Figure 4.14: Average Surface Acoustic Power as a function of Airflow for the four case studies at low and high speed modes: ⌀500 fan, ⌀500 amplified, ⌀630 fan and ⌀630 reduced.

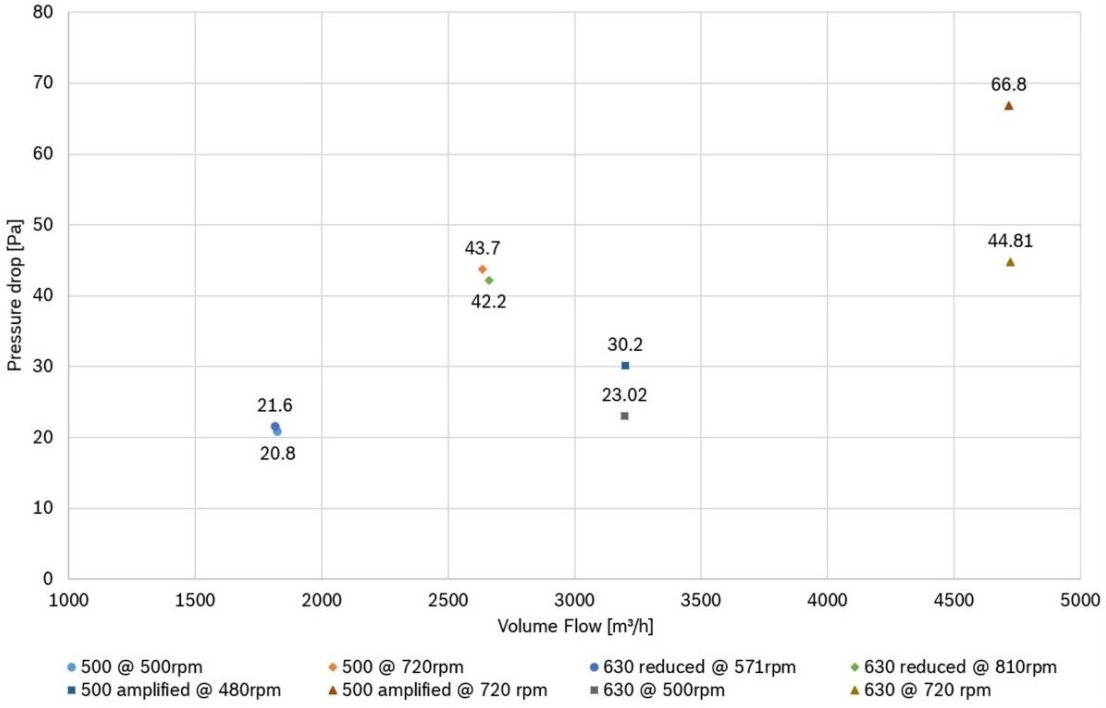

Figure 4.15: Operating Points of the four case studies at low and high speed modes.

4.2 Case Studies: Variations in Chassis Configuration to Fit the Fans

The discrepancies in the operating points of the previous models are due to the fans' different geometries and the different sizes of the evaporators in each chassis. In this chapter, the noise improvement potential of fan diameter and tip speed is evaluated within the same heat pump context. The goal was to evaluate the influence on aerodynamic noise of using the original ⌀630 fan in the small-chassis, instead of the ⌀500 fan model. Therefore, the chassis housing that connects the evaporator to the fan had to be changed and adapted to house the bigger fan. The two case studies to be compared are therefore:

- Case 1: ⌀500 Fan in small-chassis
- Case 2: ⌀630 Fan in small-chassis

Once again, to ensure a fair comparison between both cases, the speed of Case 2 was adjusted to deliver the same airflow as Case 1, using an iterative process supported by the fan affinity law represented by Equation (3.11) . The tip clearance for the ⌀630 fan model, which was 5,5 mm in the mid-chassis, was reduced to 3 mm for correct analogy.

4.2.1 CFD model

The CFD setup, meshing techniques, turbulence and acoustic models were applied as described in Chapter 4.1.1. The geometries to be compared can be observed in Figure 4.16. The evaporator resistance data remains the same and can be consulted in Table 4.1.

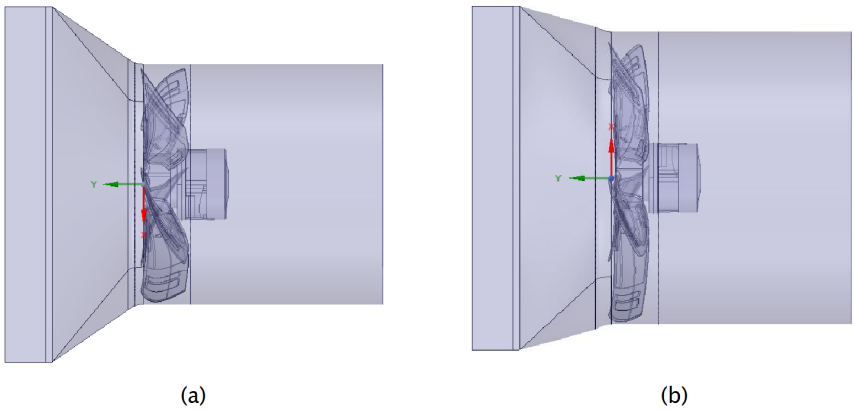

Figure 4.16: CFD model setup a) ⌀500 fan in small-chassis b) ⌀630 fan in small-chassis with adapted connection chamber and outlet domain.

4.2.2 Results

The results obtained for the ⌀630 fan model inserted in the small-chassis and rotating at adjusted speeds are listed in Table 4.3, alongside the data from Chapter 4.1.3 for the ⌀500 fan in the small-chassis.

Table 4.3: Operating points, tip speed and surface Acoustic Power Level (SWL) for the original fans inserted in the small-chassis.

Fan	⌀$[mm]$	**velocity** $[rpm]$	**Airflow** $[m^3/h]$	**Pressure Drop** $[Pa]$	**Tip Speed** $[m/s]$	**Area Avg. SWL** $[dB]$	**Max. SWL** $[dB]$
500 fan	500	500	1825,2	20,8	13,1	40,1	63,1
	500	720	2635,2	43,7	18,9	47,9	73,8
630 fan	630	365	1821,6	16,3	12,0	36,8	59,5
	630	510	2656,8	31,0	16,8	43,9	67,0

Figure 4.17 shows the velocity and pressure contours at the central section view. By comparison with Figure 4.4 and data from Table 4.3 , it is possible to verify lower tip speed for the bigger fan, due to the lower motor speed required. The same airflow can be obtained at lower rotation speed given the bigger fan diameter: while the ⌀500 model needs 500 rpm to reach 1825 m^3/s, the ⌀630 model requires only 365 rpm to reach the same airflow. Overall, the flow distribution and pressure contours are similar to the ⌀500 model and it was also possible to identify reverse flow downstream of the fan.

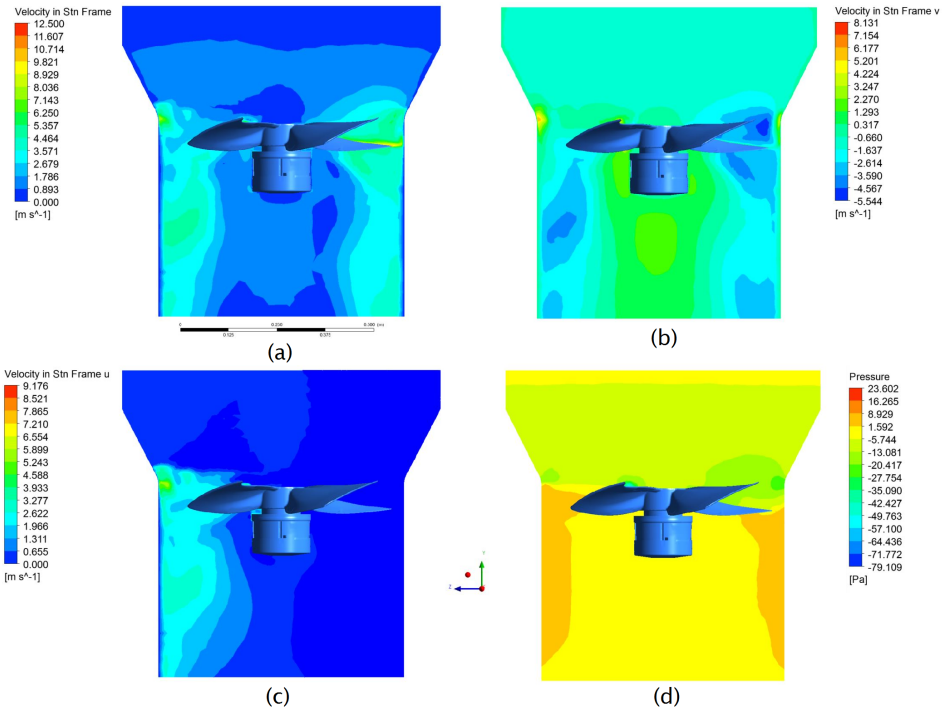

Figure 4.17: Velocity and Pressure contours at central section view of the small-chassis with the ⌀630 fan at 365 rpm a) velocity magnitude m/s b) Y-directed velocity m/s c) X-directed velocity m/s d) static pressure Pa.

The critical boundary layer noise areas for the ⌀630 fan correspond to the same areas described in Chapter 4.1.3, although lower dB values are manifested at the fan blades due to the lower rotational speed (Figure 4.19). Compared to the ⌀500 fan rotating

at 500 *rpm*, considerable less critical areas can be observed, specially on the suction side of the fans. These contours show the considerable impact angular velocity has on aerodynamic noise. Recalling the non-dimensional analysis performed in Chapter 3.4.3, in can be observed where the switch from the ⌀500 to the ⌀630 model places itself on the chart for both speed modes, see Figure 4.18.

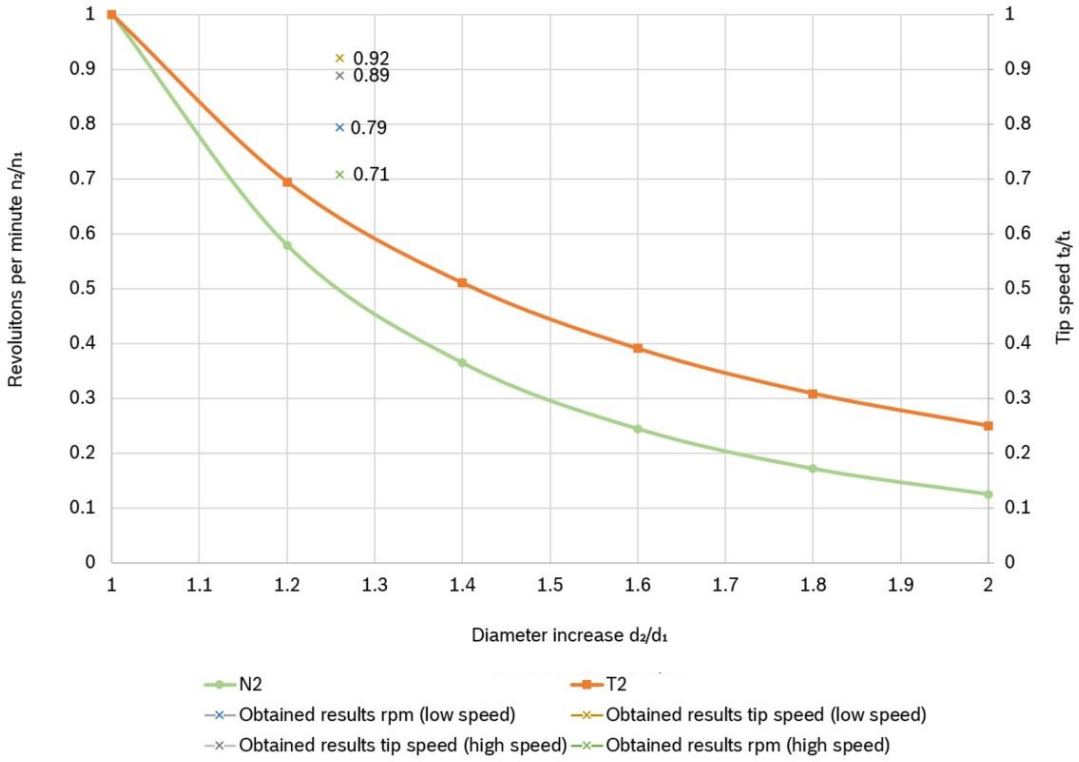

Figure 4.18: Non-dimensional curves demonstrated in chapter 3.4.3 plotted against the obtained points, which reflect the *rpm* reduction from 500 to 365 and 720 to 510, and the tip speed reduction from 13,1 to 12,0 and 18,9 to 16,8 m/s, for a diameter increase of $\left(\frac{630}{500}\right) = 1,26$. Note that the theoretical curves have this mathematical behavior for re-scaled versions of the same fan model, which is not the case in practical terms.

Evidently, the discrepancies seen between the theoretical and the obtained data are due to the different fan geometries. Still, it is possible to see how tip speed benefits from the diameter increase due to the lower rotational speed needed to obtain the same airflow. Figure 4.20 presents the turbulent kinetic energy contours on the fans' pressure and suction side. Turbulence is evidently dominant on the ⌀500 fan whilst rotating at higher speed. It concentrates mostly on the upper region of the fan blades and the tip, and also on some extent of the leading edge of the ⌀630 fan.

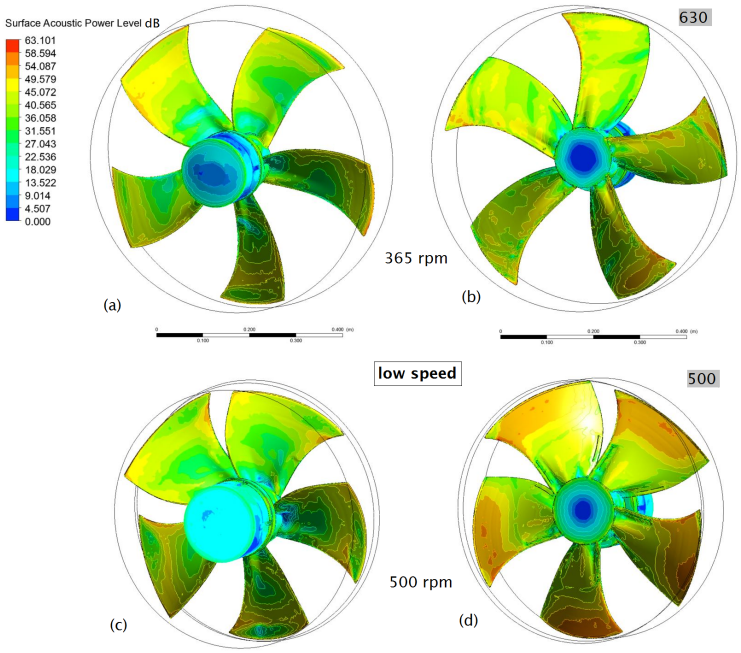

Figure 4.19: Surface Acoustic Power Level contours at a) ⌀630 fan pressure side b) ⌀630 fan suction side c) ⌀500 fan pressure side d) ⌀500 fan suction side; fan speed 365 *rpm* for a) and b) and 500 *rpm* for c) and d).

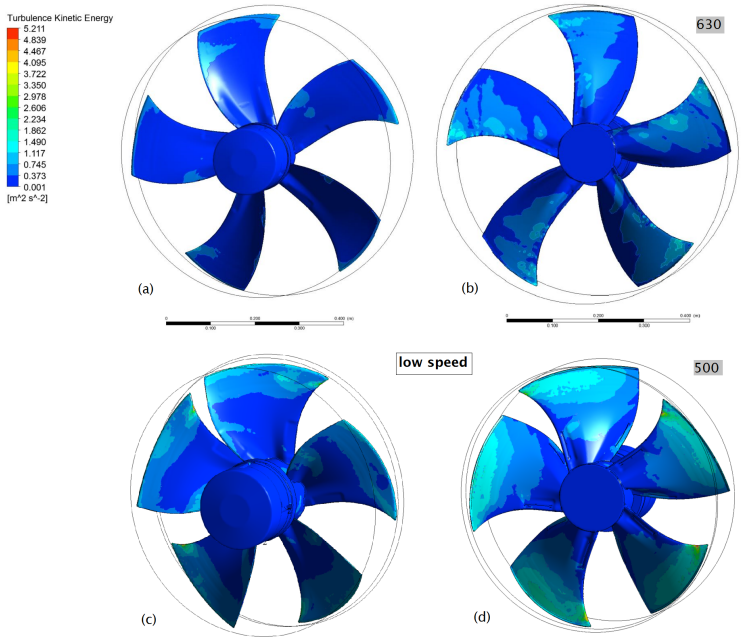

Figure 4.20: Turbulent Kinetic Energy contours at a) ⌀630 fan pressure side b) ⌀630 fan suction side c) ⌀500 fan pressure side d) ⌀500 fan suction side; fan speed 365 *rpm* for a) and b) and 500 *rpm* for c) and d).

In Figure 4.21 the velocity streamlines for the ⌀630 fan model can be observed. The streamlines indicate some inlet flow turbulence. To house the big fan in the small chassis,

adjustments on the connection chamber led to a less tapered connection, meaning that the chamber does not present a smooth converging section towards the fan as it does for the ⌀500 fan model. This rather straighter connection can lead to some inlet fluctuations thus generating turbulence in the flow, as mentioned in Chapter 3.2.4. Reverse flow near the motor is still visible in b). In Figure 4.21 d) it is possible to see some reverse tip leakage, but to less extend as previously observed. There appears to be little to no vortex roll-up. Despite the positive influence of the lower speed, the reduction in the tip clearance has most likely also a strong influence on the extension of this reverse tip flow and vortex across the fan blades. Images depicted in figures 4.21 e) and 4.21 f) show the pressure contour for this fan, and by comparison with Figure 4.12 e) and 4.12 f), it's possible to see how the pressure on the thinner fan is mostly concentrated on the upper leading edge region, while for the larger model this effect occurs mostly on the upper and trailing edge areas.

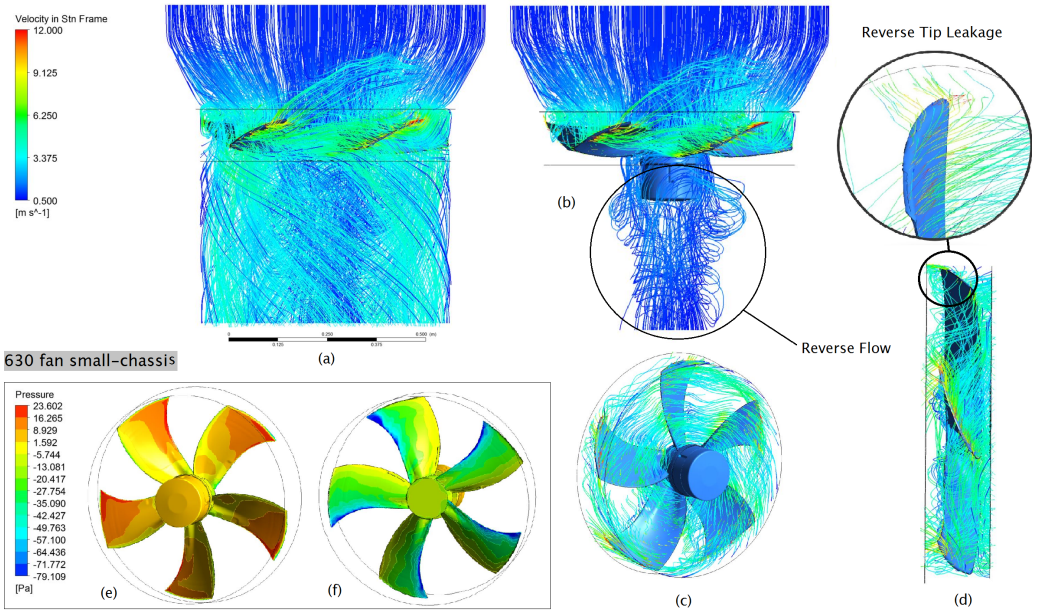

Figure 4.21: Velocity streamlines ⌀630 fan in small-chassis at 365 *rpm* a) entire model b) backwards directed flow relatively to the fan c) rotating flow domain near the fan, revealing turbulent airflow d) profile view of rotating airflow revealing less reverse tip leakage e) fan pressure side pressure contour f) fan suction side pressure contour.

Although it is possible to see fluctuations in the inlet flow by using a bigger fan on the smaller chassis, the obtained data shows how an increase in fan diameter allows for lower fan speed, thus reducing aerodynamic boundary layer noise on the fan blades. Lower velocities translate into less turbulent kinetic energy and less vortex generation on critical areas, such as the winglets. Figure 4.22 show the potential aerodynamic noise reduction by replacing a small fan for a bigger one, maintaining the same airflow requirements, whilst Figure 4.23 plots the operating points of the simulated models at low and high speed modes. Despite inserted within the same environment and moving the same airflow, the operating points still do not match exactly. The pressure drop across the fan changes slightly between both models due to the difference in the blade geometry. Also, the ⌀630 fan model has an increased inlet area, thus a reduced airflow

velocity is expected when compared to the ⌀500 fan.

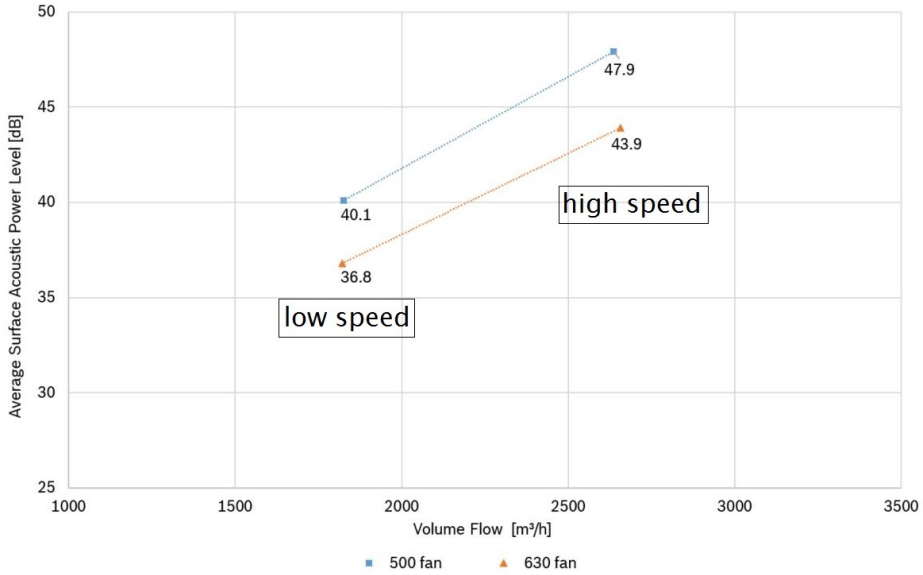

Figure 4.22: Average Surface Acoustic Power Level as a function of Airflow for the two case studies at low and high speed modes: ⌀630 fan and ⌀500 fan in small-chassis.

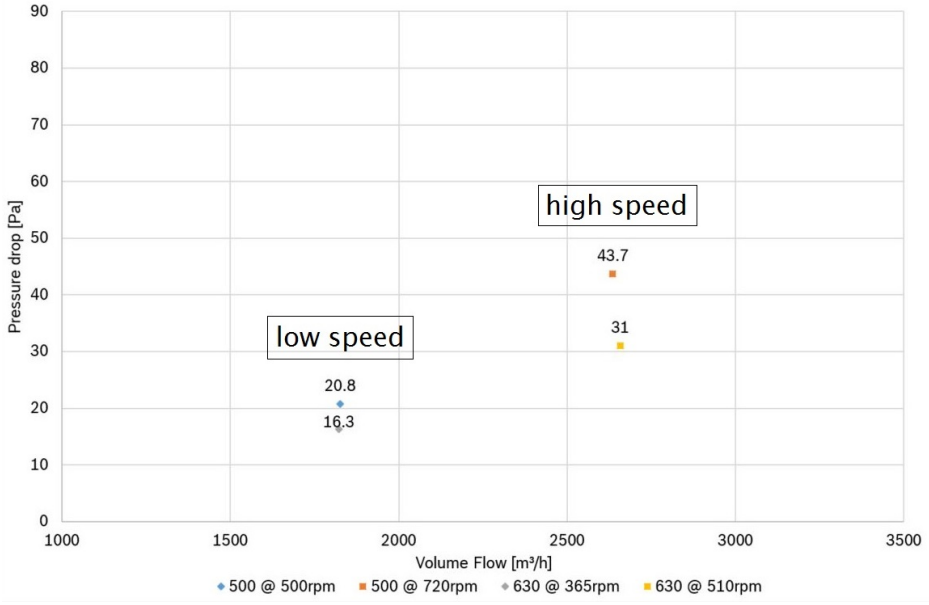

Figure 4.23: Operating Points of the two case studies in the small-chassis at low and high speed modes: ⌀630 fan and ⌀500 fan in small-chassis.

4.3 Conclusions

From the outcome of the work documented within this Chapter 4, some striking remarks can be drawn:

- The case studies enabled to identify the main sources of broadband noise on the fan models, which can be summarized as the turbulent flow behavior resulting from reverse flow at the tip clearance and the consequently vortex roll-up effect, as well as the interaction between rotating fan flow and inlet flow fluctuations.
- Both fans, ⌀500 and ⌀630, are designed by the manufacturer and the characteristics of each blade are likely to be optimized for each model considering the fan's diameter and its most suitable operating range. Therefore, amplifying or reducing the existing fans may affect negatively their performance, resulting in higher acoustic power levels at the fan surfaces. This would inevitably result in increased noise emissions into the far-field;
- The operating points of the re-scaled fans, despite respecting the airflow requirements, undergo relevant changes in pressure drop which shall not be ignored. Fan efficiency and heat removal from the evaporator are two variables which would most likely be affected;
- Re-scaling the fans would result in increased aerodynamic noise levels for both speed modes and both chassis, as evidenced from the information gathered in Figure 4.14;
- Using a fan with increased diameter allows for lower operating speeds while respecting the required airflow. The tip speed has high influence on fan aeroacoustics and the decrease in rotational velocity has more effect onto emitted noise than the increase in fan diameter;
- There is a 3,3 dB noise improvement potential at low speed and 4 dB at high speed mode for the small-chassis unit whilst using the ⌀630 fan instead of the ⌀500 fan model, see Figure 4.22;
- Still, the operating point of the ⌀500 fan at low and high speed modes can't be matched precisely using the ⌀630 fan, due to geometry differences on the blades and the connection chambers. The possibility of using the bigger fan rotating at lower velocities requires studying its exact operating point on the fan curve; if near-stall or stall range is reached, it is advised to use higher speeds.

Chapter 5

Influence of Motor Cap on Aerodynamic Noise

5.1 Case Studies

Bosch Heat Pumps have a cap in front of the fan motor for aesthetic purposes, as illustrated in Figure 5.1. Preliminary noise measurements performed by Bosch on these appliances indicated that the motor cap was responsible for noise reduction in the far-field.

In this chapter, the same CFD models presented in Chapter 4.2 (⌀630 and ⌀500 fan models in the small-chassis) were simulated with the motor cap and compared to the previously obtained data. On further analysis, the motor cap diameter was modified to evaluate its influence on the downstream flow and identify which phenomena were impacting the aerodynamic noise of the fans.

Ten different case studies were defined for this analysis; each case study was simulated within the small-chassis for both fans at low and high speed modes, in a total of 40 different simulations, see Table 5.1. The simulation workflow diagram can be found in Appendix A. In Figure 5.2, three of the aforementioned models can be observed for the ⌀500 fan model.

Table 5.1: Motor Cap case studies.

Original Cap $[mm]$	**Reductions** [%]	**Amplifications** [%]
270	15	10
-	10	15
-	-	25
-	-	35
-	-	40
-	-	50
-	-	65

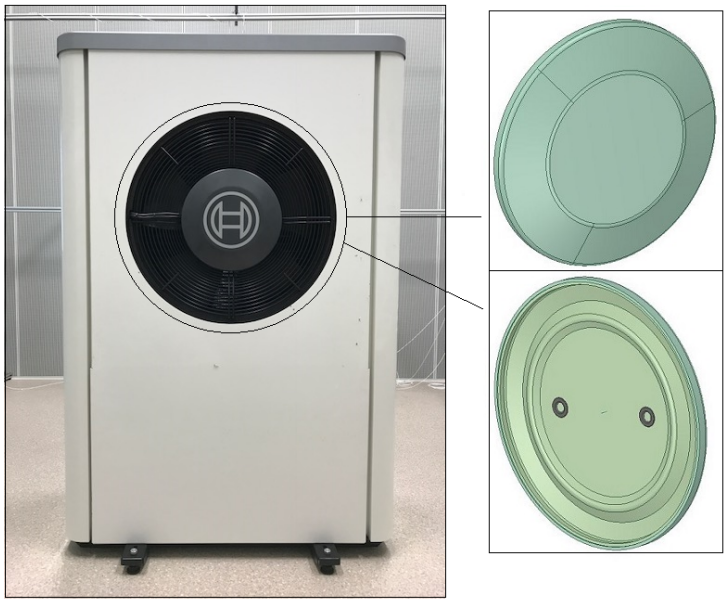

Figure 5.1: Motor cap with the Bosch symbol, fixed at the ⌀500 fan motor in the small-chassis unit.

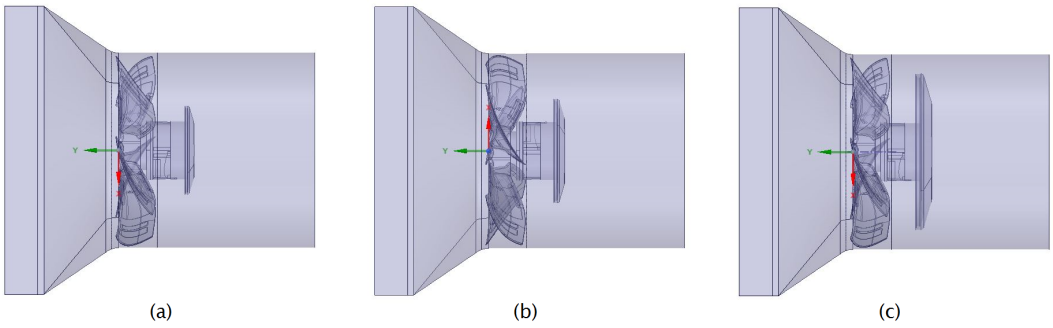

Figure 5.2: Examples of CFD models for the ⌀500 fan in the small-chassis with motor cap a) 15% diameter reduction b) original motor cap c) 50% diameter amplification.

Tip clearance remains 3 *mm* for the two fans. The CFD setup and meshing techniques were the same as described in Chapter 4.1.1.

5.1.1 Results

The results obtained from the motor cap analysis are listed in tables 5.2 and 5.3 for the ⌀500 and the ⌀630 fan models, respectively.

Note that the ⌀500 fan with original motor cap model shows a slight decrease in airflow for the low speed mode.

Table 5.2: Operating points and surface Acoustic Power Level (SWL) for the motor cap variations performed on the ⌀500 fan model in small-chassis, at low and high speed modes.

Fan	**cap** ⌀$[mm]$	**velocity** $[rpm]$	**Airflow** $[m^3/h]$	**Pressure Drop** $[Pa]$	**Area Avg. SWL** $[dB]$	**Max. SWL** $[dB]$
500 o*	-	500	1825,2	20,8	40,1	63,1
		720	2635,2	43,7	47,9	73,8
Cap o*	270,0	500	1764,0	22,7	39,0	60,2
		720	2635,2	42,0	47,1	74,1
-15%	229,5	500	1789,2	21,0	39,0	61,8
		720	2667,6	40,3	47,1	73,3
-10%	243,0	500	1764,0	22,0	39,3	61,2
		720	2689,2	39,4	46,9	72,6
10%	297,0	500	1692,0	23,1	39,2	60,5
		720	2538,0	46,1	47,2	74,5
15%	310,5	500	1692,0	24,3	39,1	58,7
		720	2520,0	46,7	47,0	74,2
25%	337,5	500	1584,0	24,1	38,4	60,1
		720	2304,0	53,4	46,1	71,5
35%	364,5	500	1440,0	26,1	38,9	60,0
		720	2160,0	57,8	45,0	68,5
40%	378,0	500	1350,0	26,3	39,1	61,1
		720	2088,0	59,3	44,7	68,1
50%	405,0	500	1188,0	29,1	38,5	60,4
		720	1818,0	65,8	43,4	69,2
65%	445,5	500	864,0	35,3	37,2	62,9
		720	1332,0	82,2	41,8	71,6

o* - denotes original model

Table 5.3: Operating points and surface Acoustic Power Level (SWL) for the motor cap variations performed on the ⌀630 fan model in small-chassis, at low and high speed modes.

Fan	**cap** ⌀$[mm]$	**velocity** $[rpm]$	**Airflow** $[m^3/h]$	**Pressure Drop** $[Pa]$	**Area Avg. SWL** $[dB]$	**Max. SWL** $[dB]$
630 o*	-	365	1821,6	16,3	36,8	59,5
		510	2656,8	31,0	43,9	67,0
Cap o*	270,0	365	1836,0	16,0	35,0	58,1
		510	2692,8	31,6	41,0	65,6
-15%	229,5	365	1836,0	15,7	36,0	59,9
		510	2667,6	29,9	43,0	65,0
-10%	243,0	365	1836,0	15,9	36,0	60,4
		510	2685,6	30,1	42,9	66,7
10%	297,0	365	1821,6	15,5	34,3	60,1
		510	2664,0	31,6	40,9	69,7
15%	310,5	365	1818,0	15,5	34,5	58,7
		510	2685,6	31,3	41,2	65,8
25%	337,5	365	1800,0	15,8	34,4	58,4
		510	2685,6	33,5	41,4	66,0
35%	364,5	365	1746,0	15,3	34,0	61,0
		510	2628,0	31,6	41,0	67,5
40%	378,0	365	1717,2	15,4	34,7	57,0
		510	2613,6	33,8	41,2	66,9
50%	405,0	365	1659,6	15,8	34,8	58,0
		510	2448,0	31,5	41,2	66,1
65%	445,5	365	1562,4	17,9	37,3	61,7
		510	2232,0	32,9	41,9	65,4

o* - denotes original model

Comparison of models with and without motor cap

First, the models with and without motor cap were compared to understand the overall influence of this component.

As can be observed in Figure 5.3, the motor cap prevents reverse flow downstream of the fan. In the models without the cap, the axial reverse flow is more prominent near the fan hub and the root of the blades. This reverse flow interacts with the energized airflow of the fan and creates turbulence near those areas, generating more boundary layer noise. Therefore, the surface acoustic power level is less critical in those regions with the motor cap than without, see figures 5.4 and 5.5. However, the acoustic power level contours on the motor surfaces are lower without the motor cap. This is likely due to some flow accumulation that happens with the motor cap, increasing pressure fluctuations near the motor.

Still, the motor cap models show an average lower acoustic power level on the fan's surface for both models and speed modes, as evidenced in figures 5.4 and 5.5.

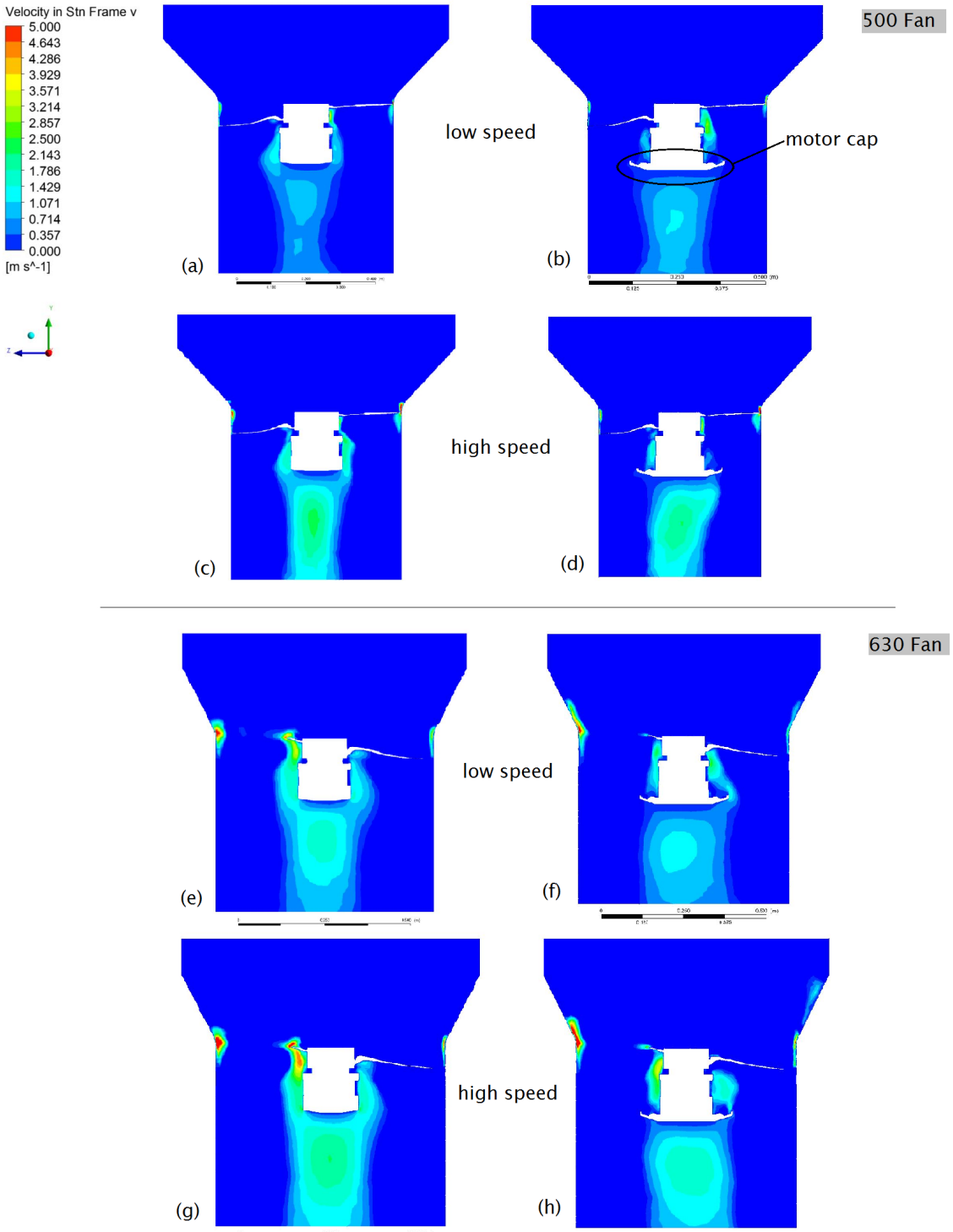

Figure 5.3: Reverse flow identified by Y-directed velocity contours at central section view of fan models, with and without motor cap; upper images correspond to the ⌀500 fan in small-chassis a) without motor cap at 500 *rpm* b) with motor cap at 500 *rpm* c) without cap at 720 *rpm* d) with cap at 720 *rpm*; lower images represent the ⌀630 fan in small chassis e) without cap at 365 *rpm* f) with cap at 365 *rpm* g) without cap at 510 *rpm* h) with cap at 510 *rpm*.

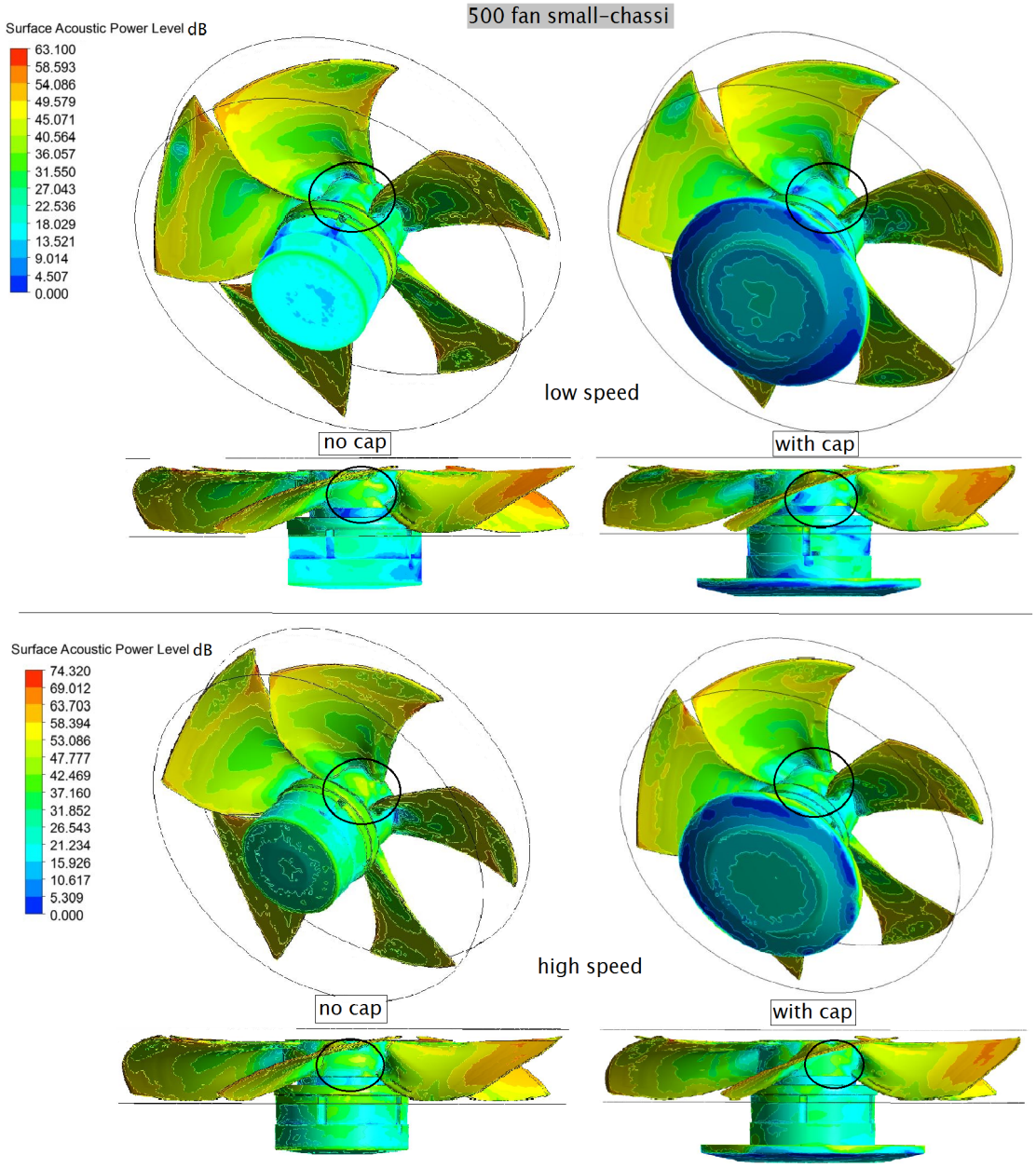

Figure 5.4: Surface Acoustic Power Level [dB] on the ⌀500 fan model, with and without cap, at 500 and 720 rpm.

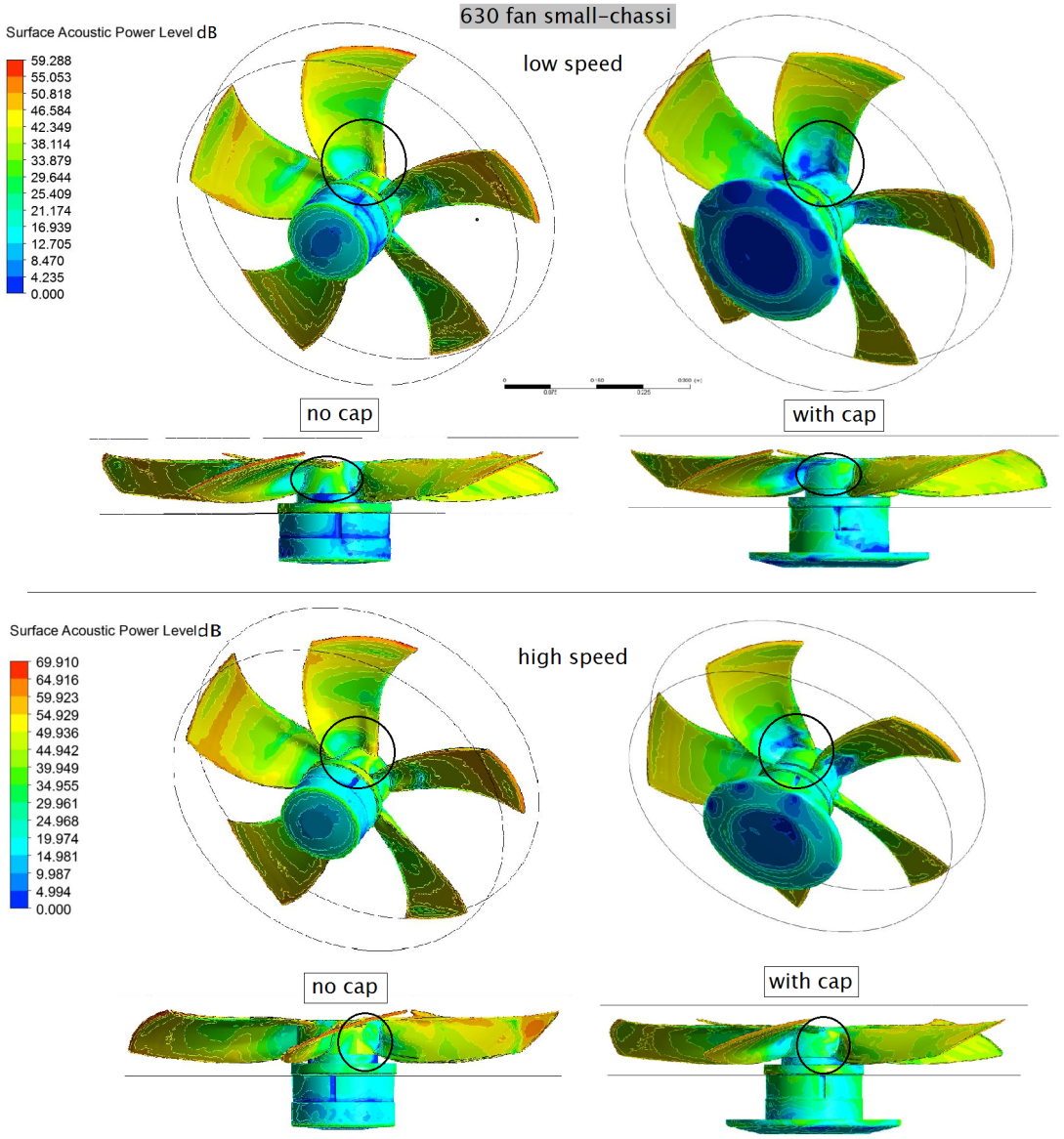

Figure 5.5: Surface Acoustic Power Level [dB] on the ⌀630 fan model, with and without cap, at 365 and 510 rpm.

Comparison within motor cap variations

As mentioned before, by running several diameter variations it was possible to realize some optimization analysis. In figures 5.6 and 5.7, the average acoustic power on both fans is represented as a function of cap diameter.

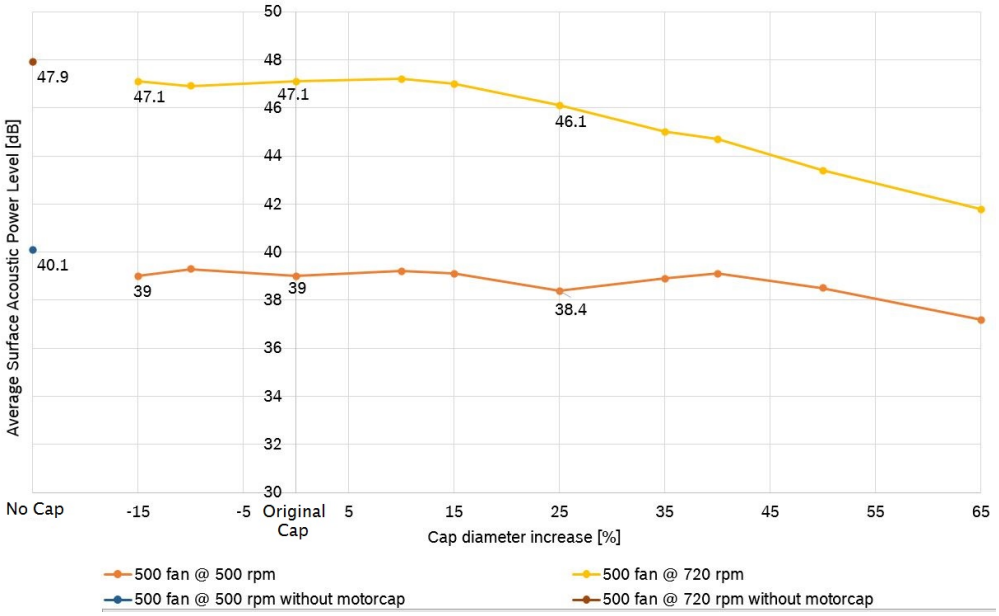

Figure 5.6: Average Surface Acoustic Power as a function of percentual diameter variation, as well as without motor cap, ⌀500 fan in small-chassis at low (500 *rpm*) and high (720 *rpm*) speed modes.

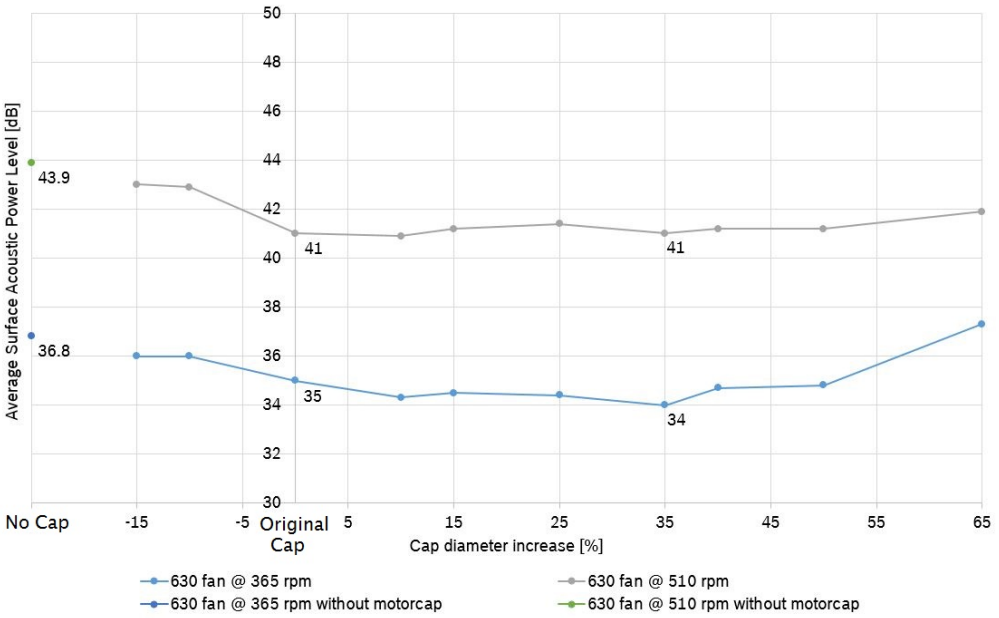

Figure 5.7: Average Surface Acoustic Power as a function of percentual diameter variation, as well as without motor cap, ⌀630 fan in small-chassis at low (365 *rpm*) and high (510 *rpm*) speed modes.

Increasing the diameter of the motor cap excessively has drastic impact on the operating point of the fans, specially for the ⌀500 model, as can be observed in the data from tables 5.2 and 5.3. Figure 5.8 shows a plot of the operating point evolution with

increasing motor cap diameter for the ⌀500 fan, to better illustrate this observation. The motor cap introduces some resistance into the system, which results in increased pressure downstream of the fan.

For the ⌀500 model, the average surface acoustic power on the fan decreases with increased diameter, see Figure 5.6. Although the motor cap helps preventing reverse flow downstream of the fan, the noise improvement stated in the chart shall not be used to draw conclusions, given the significant shift in the operating points of the fan. Therefore, the cap variations of -15% and 25% were chosen as the best candidates for further analysis, as they proved to be the most promising ones, given its operating points and noise improvement potential: 0,6 and 1 dB at low and high speed modes, respectively, for the 25% diameter increase, while no significant changes were registered with the 15% reduction, see highlighted data in Figure 5.6.

For the ⌀630 model, decreasing the cap diameter and increasing it above 40% impact aerodynamic noise rather negatively. The motor cap variations do not have significant impact on the fan's operating points, due to the bigger fan diameter. In this case, the 35% diameter increase was selected as the cap variation with most potential noise improvement when compared to the original cap, given the 1 dB simulation result registered at low speed mode and no significant influence at high speed mode, see highlighted data in Figure 5.7.

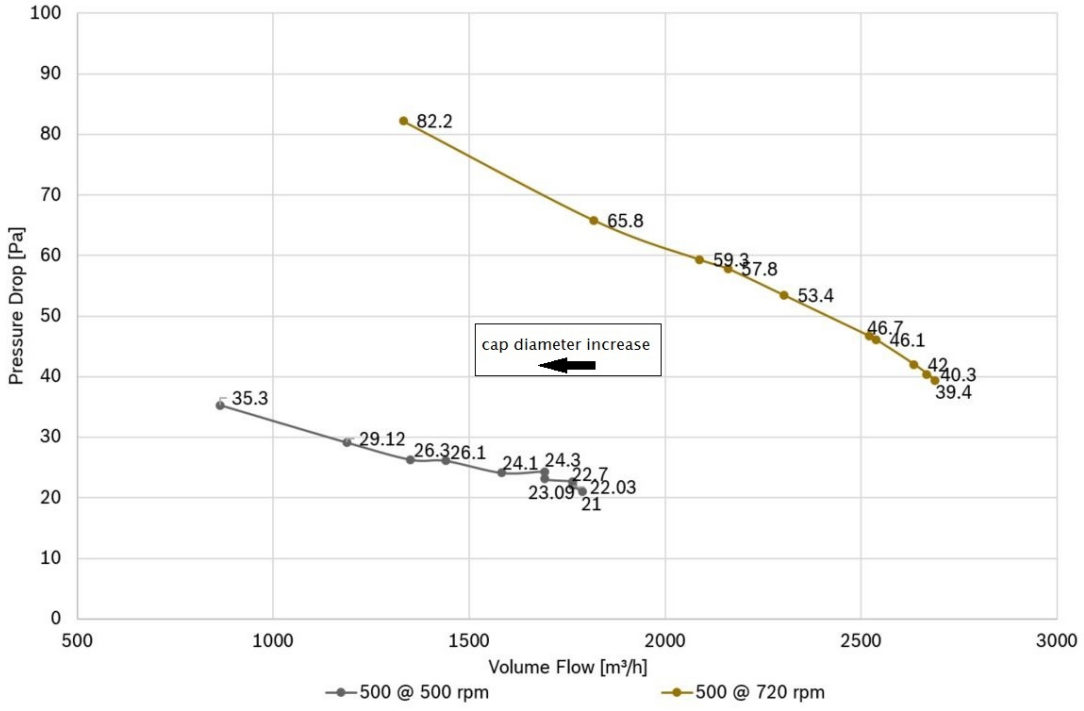

Figure 5.8: Operating Points of the motor cap variations performed on the ⌀500 fan in small-chassis, at low (500 rpm) and high (720 rpm) speed modes.

5.2 Iterative Process for Airflow Requirement - ⌀500 fan

As mentioned before, a fair comparison can only be met when the fans to be evaluated provide the same airflow rate. Therefore, Equation (3.11) was once again used to determine the rotation speed of each model holding the same airflow as the reference conditions.

This iterative process was solemnly performed on the ⌀500 fan, given time limitations and the uncertainty regarding the possibility of using the ⌀630 fan in the small-chassis unit, as suggested in Chapter 4.3.

5.2.1 Results

Table 5.4 presents the results at the fan surface under adjusted operating conditions.

Note that, as mentioned before, the airflow for the ⌀500 fan at low speed mode was slightly lower, therefore the speed was also adjusted for this case, which resulted in a slightly higher noise level.

Table 5.4: Operating points and surface Acoustic Power Level (SWL) for the motor cap variations performed on the 500 fan model in small-chassis, at low and high speed modes for airflow requirements after speed corrections.

Fan	**cap** ⌀$[mm]$	**velocity** $[rpm]$	**Airflow** $[m^3/h]$	**Pressure Drop** $[Pa]$	**Area Avg. SWL** $[dB]$
Cap o*	270,0	517	1829,0	24,5	39,7
	270,0	720	2635,2	42,0	47,1
-15%	229,5	510	1836,0	22,0	39,6
	229,5	711	2615,4	39,3	46,8
25%	337,5	539	1800,0	29,9	39,9
	337,5	823	2700,0	64,0	48,9

o* - denotes original model

From Table 5.4 and Figure 5.9, it is possible to observe how speed adjustments suppress the positive effect of the motor cap in terms of aerodynamic noise on the fan's surface.

Given that a diameter reduction is the possibility which requires the lowest speed adjustments to meet the prescribed flow expectations, it is the most attractive option of the analyzed variations. At both speeds, it shows a potential noise improvement of 0,5 and 1,1 dB, compared to the same fan operating without motor cap.

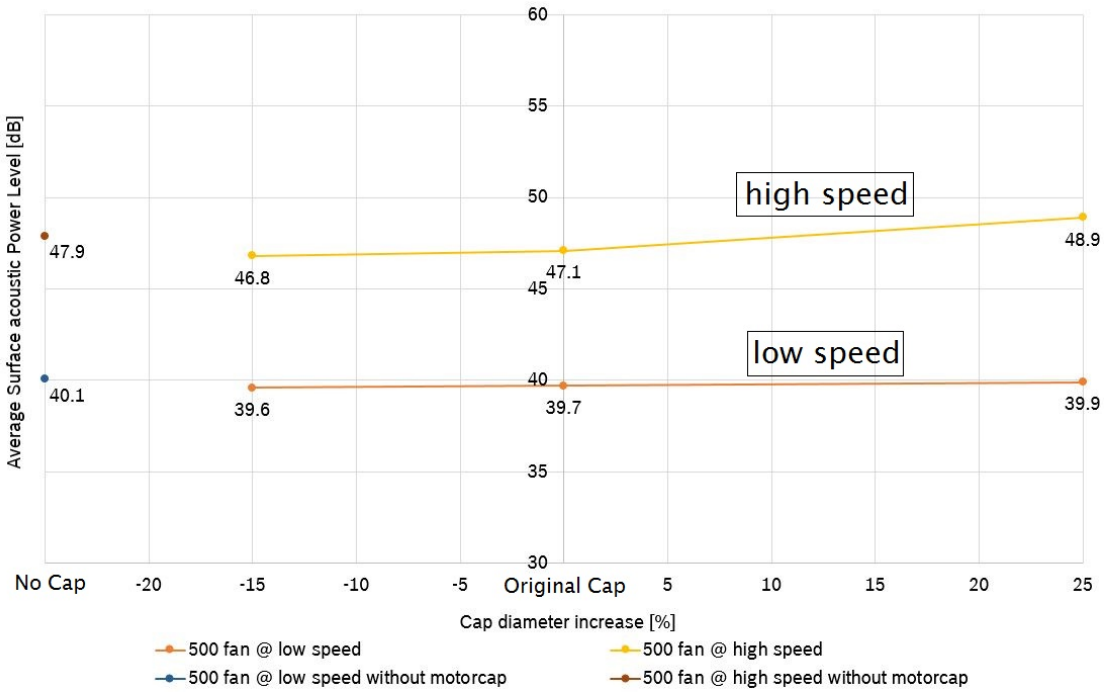

Figure 5.9: Average Acoustic Power Level on the ⌀500 fan in small-chassis at low and high speed modes, adjusted to guarantee the same airflow as the model without motor cap.

5.3 Conclusions

The following conclusions can be drawn from the collected data in regard to the motor cap analysis:

- The motor cap influences boundary layer noise on the fans by avoiding reverse axial flow (Figure 5.3) that otherwise would likely interact with the outlet fan flow and generate complex turbulent behavior.
- Although the motor cap reduces the emitted noise level, it influences the operating point of the fans by introducing resistance into the system, specially on the ⌀500 fan due to its small diameter, see Figure 5.8.
- The motor cap diameter optimization is a function on the fan's diameter and its operating speed, therefore creating an optimal cap that fits both fans at all operating points is impossible. It is important to establish a compromise between the positive effect of bigger caps and the downside of it shifting the operating points. Within this line of reasoning, two possible optimized caps were selected and further evaluated for the ⌀500 fan: -15% and 25% cap diameter variations.
- By adjusting the fan speed to meet the airflow requirements on the selected cap variations, the noise improvements become almost non-existent, see Figure 5.9. Therefore, and to prevent additional design efforts and production costs associated to a new motor cap design, it is suggested to keep the original motor cap, as it

shows potential improvements of 0,4 and 0,8 dB for the $\varnothing$500 fan at low and high speed modes, when compared to the CFD model without cap.

Chapter 6

Noise Reduction Features

To conclude the numerical analysis, two different noise reduction features were introduced, with the potential effect of reducing the noise emitted by the fans: a fan with serrated trailing edges and a fan with golf-ball dimples on its suction side, simulated within two scenarios: in free-flow condition and in the heat pump environment.

The noise benefits from serrated edges have been studied by several authors (see Chapter 3.2.3) over the past years and are proven to help reduce noise under certain conditions. However, adding serrations to an existing fan designed without taking into account for these features could have an unexpected effect. Therefore, serrations were designed and added to the current fan for comparison with the normal model.

The second feature, the dimpled fan, is an original idea. This feature was inspired in the golf-ball dimples' effect, which will be explained in more detail hereafter. Applied to the fan's surface, the golf-ball dimples were expected to help keep the airflow attached to the blade surface by increasing flow momentum, thus avoiding flow separation. The dimples were added to the upper suction side area of the fans, one of the most problematic regions for aerodynamic noise (see acoustic power contours in figures 4.9 and 4.19). Given the complex design of the fan blades and the time frame available for this work, this was the only dimple design analyzed. Future investigation proposals and work suggestions using fans with dimples can be consulted in Chapter 8.2.

More details on the design and sizing of the mentioned features can be consulted within the next chapters. The simulation workflow diagram is presented in Appendix A.

6.1 The Effect of Golf-ball Dimples

The main idea behind dimples on golf-balls is to keep the flow longer attached to the balls surface by inducing small-scale turbulence in the boundary layer. Small-scale eddies will appear on the carved surface of each dimple, due to the pressure and velocity fluctuations induced by the geometries. This will energize the flow and delay the flow separation point. The wake behind the ball will then be thinner and generate less drag and more lift.

Several studies have shown the positive effect of dimples on drag and lift coefficients and multiple patterns, shapes and dimensions have been proposed over the years. Figure 6.1 illustrates the wake formation, the boundary layer flow regime transition and the flow separation points for a smooth and a dimpled ball.

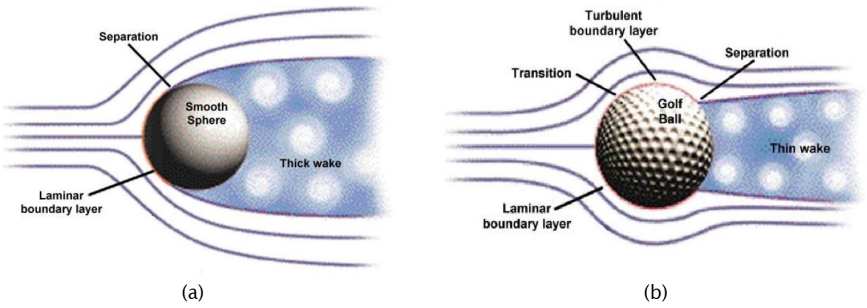

Figure 6.1: Flow behavior around a) smooth spheres and b) dimpled spheres, showing wake creation and flow separation point. Adapted from [43].

Figure 6.2 shows the pressure contour on the cavity of a golf-ball dimple, obtained by W. R. Michalchuk [44] in his experimental and numerical study of different dimple designs. The areas in green represent flow re-circulation in the cavity, whereas the yellow and red areas correspond to the regions where vortex shedding is occurring and flow velocity is nearly zero. The author indicates that the red zones correspond to nearly flow separation. The intensity of the turbulent eddies in the cavities define the energy exchange between the vortexes and the boundary layer flow, thus increased vortex shedding is favorable for overall flow attachment along the ball's surface.

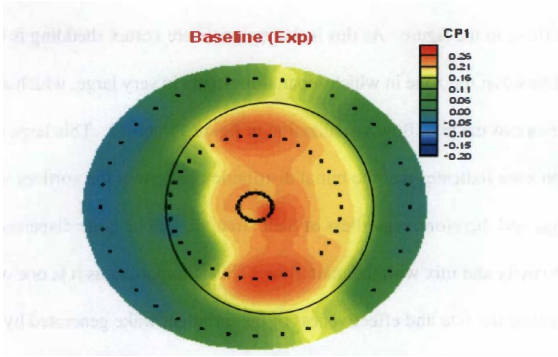

Figure 6.2: Pressure contour in a circular golf-ball dimple (baseline, experimental results); CP1 denotes a pressure measurement device used by the author [44].

6.2 CFD model: Features applied in Free Flow Conditions

These geometric features were first evaluated for free flow conditions, with a CFD model consisting of an inlet and outlet domain and a shrouded fan domain. The mesh was refined to better capture the added features. The fan operating point was plotted against the theoretical fan curve, provided by the manufacturer, for better understanding of its position within the operating range. The fans were evaluated at the characteristic low and high speed modes of the heat pump. As an additional study, and to further analyze the aeroacoustic behavior of the dimples in normal and aerodynamic stall conditions, the simple and the dimpled fans were analyzed at 800 *rpm* at a broad range of airflow rates.

Geometries

The features can be observed in Figure 6.3. Note that, for fair comparison, the rectangular surface protrusion characteristic of the original fan was removed, as will be demonstrated in Chapter 6.2.1. This protrusion is believed to be on the fan to support flow attachment. This way, it was possible to compare serrated edges and dimples to a more simple fan model.

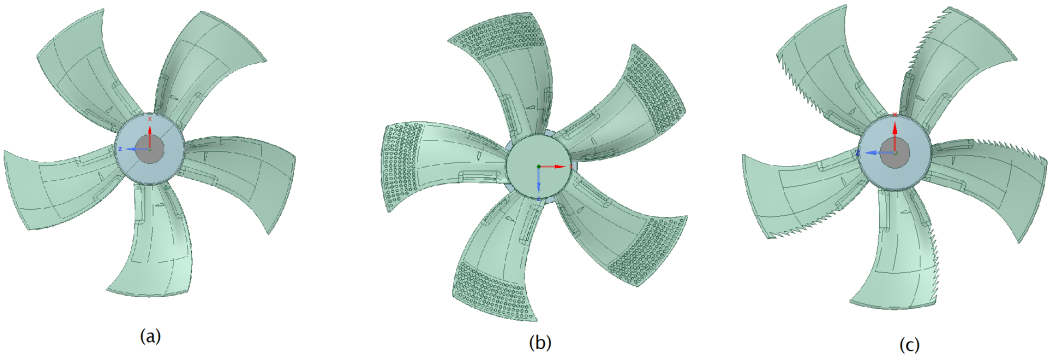

Figure 6.3: Features designed on the ⌀630 fan a) normal fan, without surface protrusion b) dimpled suction side c) serrated trailing edge.

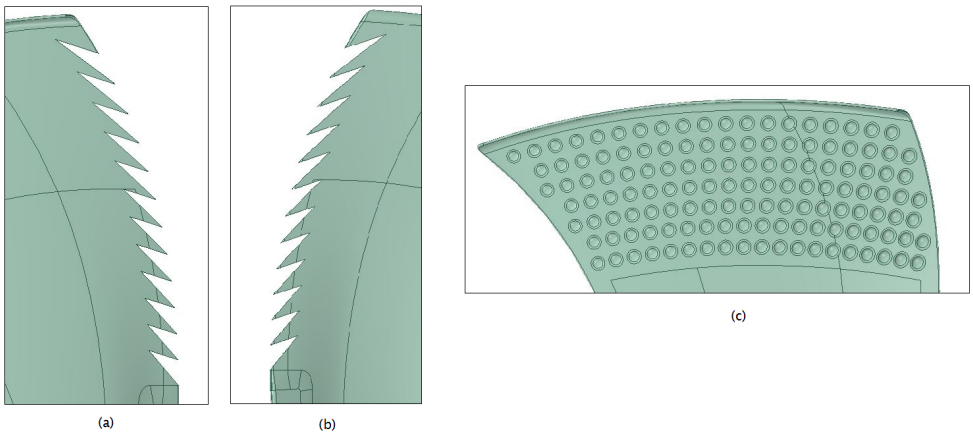

Figure 6.4: Zoom in on the features designed on the ⌀630 fan a) serrations viewed from suction side b) serrations viewed from pressure side c) dimples on suction side.

Mesh

All three models were meshed using the same mesh sizing and techniques. Once again, tetrahedral mesh elements were used with the patch conforming method and with a curvature normal angle of 4°.

Proximity and curvature size function was used with a defeaturing size of 0,66 mm. Minimum and proximity minimum mesh sizes were set to 1,33 mm. Orthogonality was used for quality control.

Mesh statistics indicate around 5 million elements for each model. The same turbulence and acoustic models as used in previous analysis were applied.

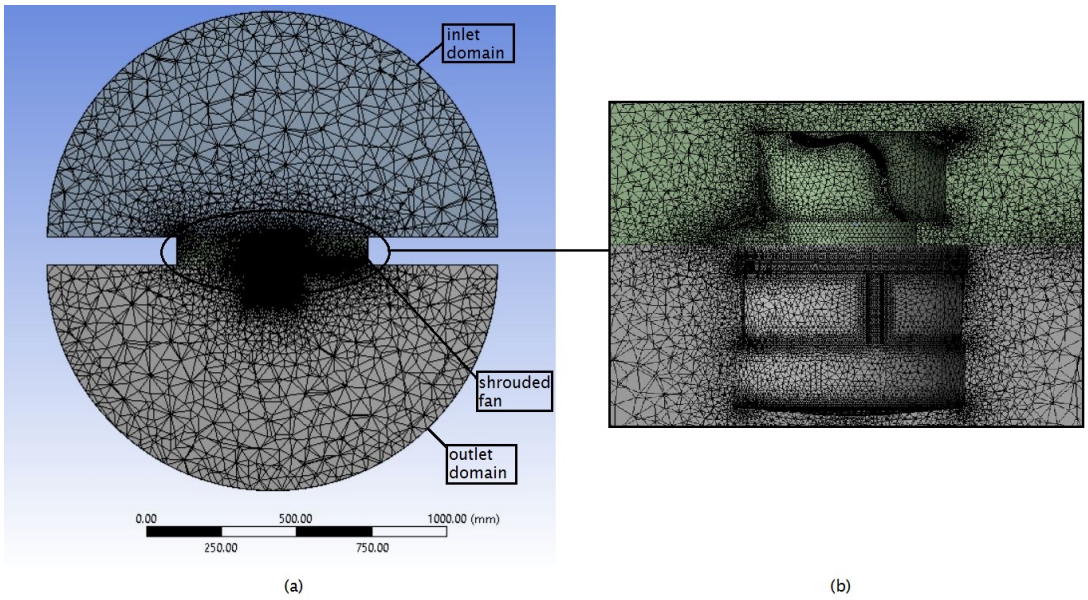

Figure 6.5: Conformal mesh for the free flow CFD model a) section view b) amplified view of mesh near fan motor and hub.

6.2.1 Simple Fan Design

The ⌀630 fan was simplified by removing surface features. Figure 6.6 shows a comparison of the fan before and after removing the rectangular protrusions, which also exist on the fan blade's suction side and from where they were removed as well.

Unigraphics NX 11.0 was used for this purpose.

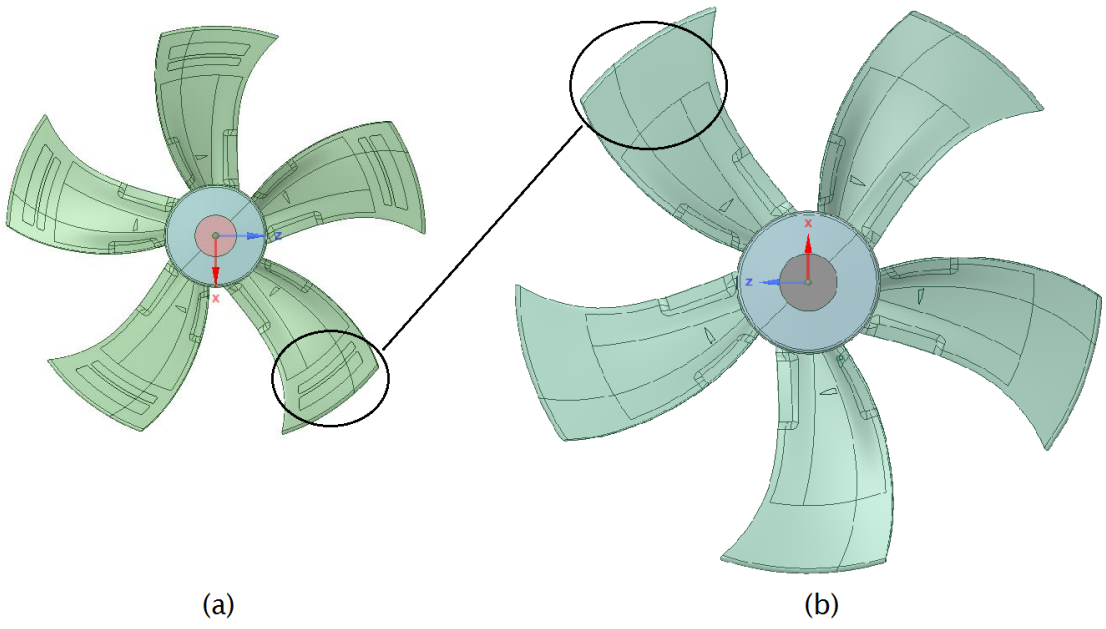

Figure 6.6: ⌀630 fan blade's pressure side a) with surface features b) without features.

6.2.2 Serrated Edges Design

These serrations were added to the simple fan shown in the previous chapter. The feature was designed based on recommendations from the literature review, exposed in Chapter 3.2.3. Very sharp serrations can result in less airflow rate, therefore a compromise between sharpness and the serrations' area was taken into account.

A spline, parallel to the trailing edge, with an offset of 12 mm and several horizontal lines, distanced 10 mm from each other, were traced. The opposite corners of the resulting trapezoid were connected and the resulting upper triangle was cut off from the fan's surface, as depicted in Figure 6.7.

These operations were performed using Ansys SpaceClaim 19.0.

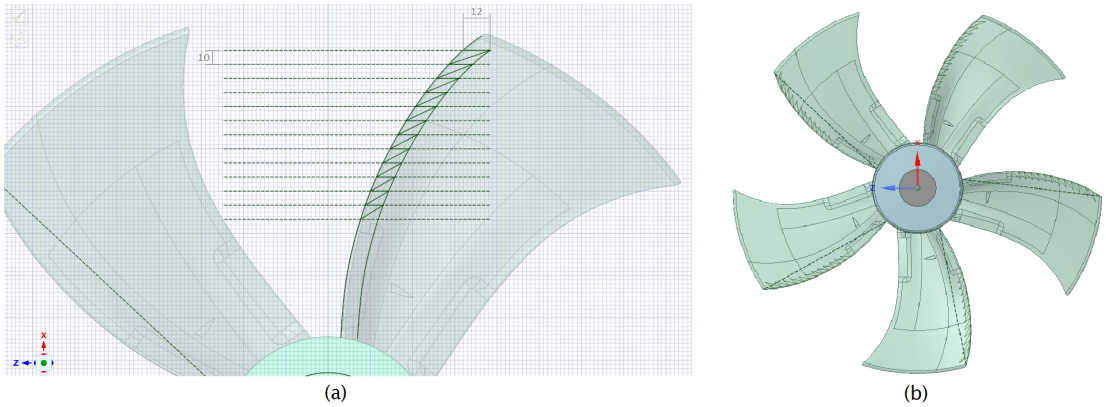

Figure 6.7: Serrated trailing edge design a) auxiliary lines and dimensions b) removed triangular areas.

6.2.3 Dimples Design

As mentioned before, the dimpled fan was inspired in the surface of golf-balls. The dimples were designed based on the golf-ball patent registered by Maehara *et al.* [45]. However, due to the difference in size magnitude between a golf-ball and a fan, the advised diameter was doubled and further research review was conducted for the dimple's depth.

The patent states the golf-ball should include different types of dimples with different diameters and/or depths. The advised dimple diameter is between 3 to 4 mm and the average dimple depth 0,12 to 0,18 mm. The preferable dimple shape is circular, although other shapes can be used [45]. Other patents and research studies show that different geometries such as hexagonal dimples can have a positive effect on drag reduction since their shape allows to cover 100% of the balls surface, whereas circular dimples don't [46].

Given the innovative nature of this investigation and time limitations, all dimples were designed with equal diameter and depth. A study conducted by Chang-Hsien *et al.* [47] evaluated the influence of golf-ball dimple configuration on aerodynamics, trajectory and acoustics and discovered that golf-balls with deep dimples (depth of 0,25 mm) produced the least noise.

Therefore, the dimples applied to the fan model were designed with a diameter of 8 mm and a depth of 0,8 mm. Further information on the dimples' design is shown in

Figure 6.8. The fan shows a total of 133 dimples per blade, distributed along seven rows on the upper suction side region. The design was created using Unigraphics NX 11.0.

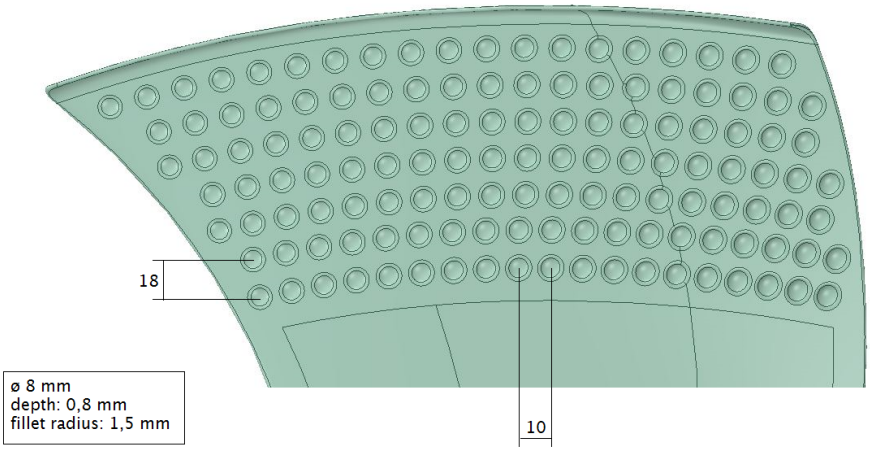

Figure 6.8: Dimples' pattern on fan blade suction side (dimensions in mm).

6.2.4 Results

In this chapter, the results obtained for the noise reduction features can be consulted; first, the aeroacoustic behavior of the serrations and the dimples is evaluated and compared to the simple fan at 500 and 720 rpm. Further, the fan curve obtained by varying the airflow rate of the simple and dimpled fans at 800 rpm is compared to the theoretical curve and the flow behavior of both fans is compared while in normal and assumed stall conditions.

Low and High speed modes

The obtained operating points and acoustic power levels can be consulted in Table 6.1. In figures 6.9 and 6.10 it is possible to observe the influence of the features on the surface acoustic power level and the turbulent kinetic energy, respectively. Figure 6.11 shows the pressure contours on the suction side of the fans. In Figure 6.12, the operating points are plotted against the theoretical fan curves of the original ⌀630 fan model.

Table 6.1: Operating points and surface Acoustic Power Level (SWL) for the three fan models.

Model	**velocity** $[rpm]$	**Airflow** $[m^3/h]$	**Pressure Drop** $[Pa]$	**Area Avg. SWL** $[dB]$	**Max. SWL** $[dB]$
Simple	500	3888,0	26,9	48,0	72,3
	720	5652,0	56,0	55,9	80,7
Dimples	500	3866,4	26,0	47,2	71,5
	720	5551,2	54,3	55,0	80,9
Serrations	500	3888,0	26,0	47,9	72,7
	720	5590,8	55,5	55,7	81,1

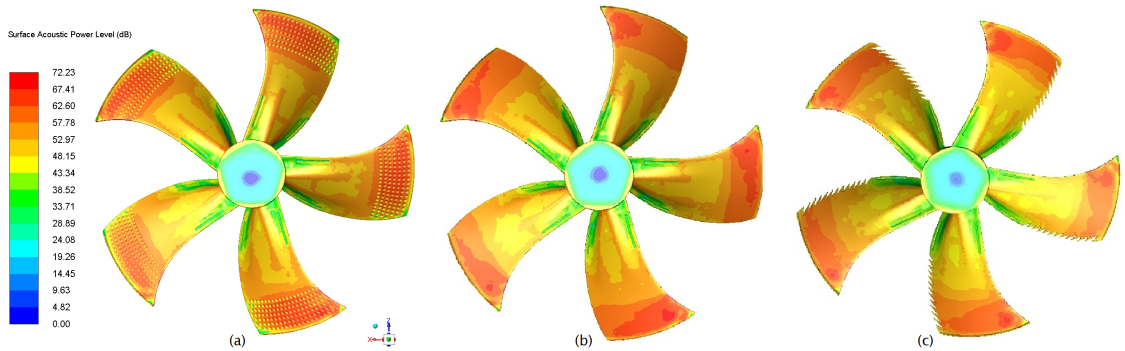

Figure 6.9: Surface Acoustic Power Level contours of the three models a) fan with dimples with area-weighted average (avg) SWL of 47,2 dB b) simple fan avg SWL of 48 dB c) fan with serrations avg SWL of 47,9 dB.

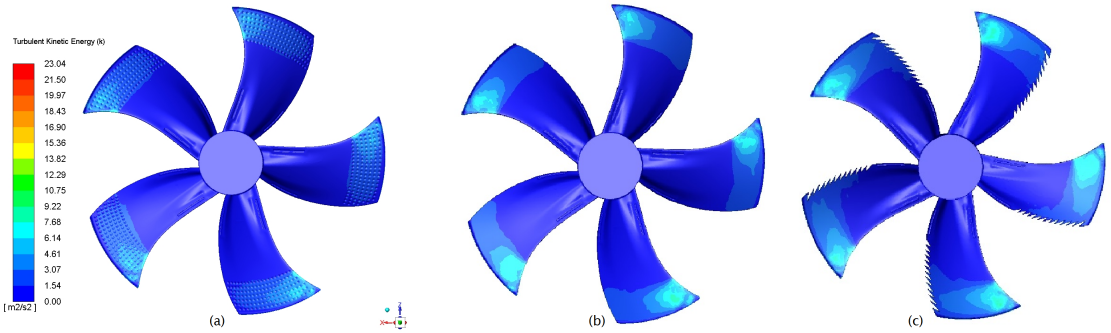

Figure 6.10: Turbulent Kinetic Energy contours of the three models a) fan with dimples avg k of 0,928 m^2/s^2 b) simple fan avg k of 1,074 m^2/s^2 c) fan with serrations avg k 1,090 m^2/s^2 .

The simulation results denote the highest noise reduction potential with the dimples design, showing 0,8 dB lower average surface acoustic power at 500 rpm and 0,9 dB at 720 rpm, when compared to the reference case. The highest surface acoustic power level on the fan is also lower with the dimples than without, see data from Table 6.1. Once again, note that the contours on each blade differ from each other due to the housing assymmetry, which influences the inlet flow conditions.

The serrated trailing edge also seems to contribute to noise reduction at the analyzed operating points, but in less extent than the dimpled fan, with a potential reduction of 0,1 and 0,2 dB at low and high speed modes, respectively. Given the small improvement, the difference registered between those values could be solemnly due to numerical errors.

By analyzing Figure 6.9, it is possible to observe how each feature influences the aerodynamic noise contours on the fan. The dimpled fan seems to spread the critical red areas along the upper part of the fan's suction side surface, with increased regions of less critical noise levels where normally higher levels should be detected.

The serrated trailing edge influences mostly the noise contours in the mid-span of the fan blades, by showing lower noise levels in those areas. The noise reduction features did not change the operating point of the fan. Small discrepancies are mostly believed to be due to the numerical error associated to the simulations.

In Figure 6.10, it is possible to see how the dimpled model presents less critical turbulent kinetic energy regions where the dimples are located. No significant changes can be detected in the serrated model.

From Figure 6.11, it is possible to observe how the pressure contours between the different cases are similar, although a pressure rise can be observed inside the dimples' cavity, see d) from Figure 6.11, which is supported by literature [44].

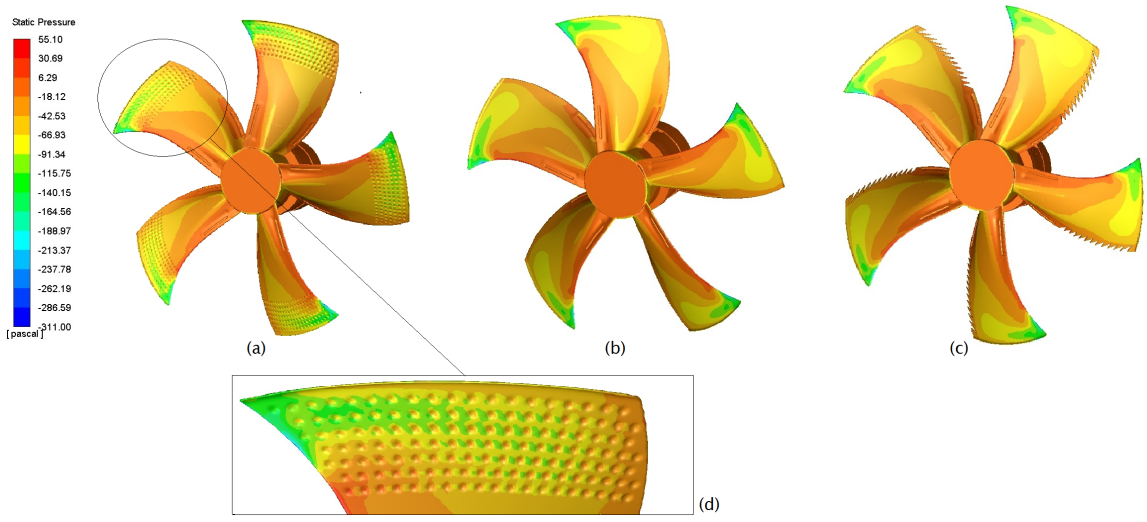

Figure 6.11: Pressure at suction side a) fan with dimples $avg\ \Delta P$ of -23,87 Pa b) simple fan $avg\ \Delta P$ of -25,13 Pa c) fan with serrations $avg\ \Delta P$ of -23,51 Pa d) amplified view of pressure contours inside the dimples' cavities.

Figure 6.12 shows the location of the operating points on the fan curves. The obtained results differ only slightly from the theoretical values. As can be observed, the simulated models are operating at normal airflow rates, with similar pressure drops to the ones predicted by the manufacturer.

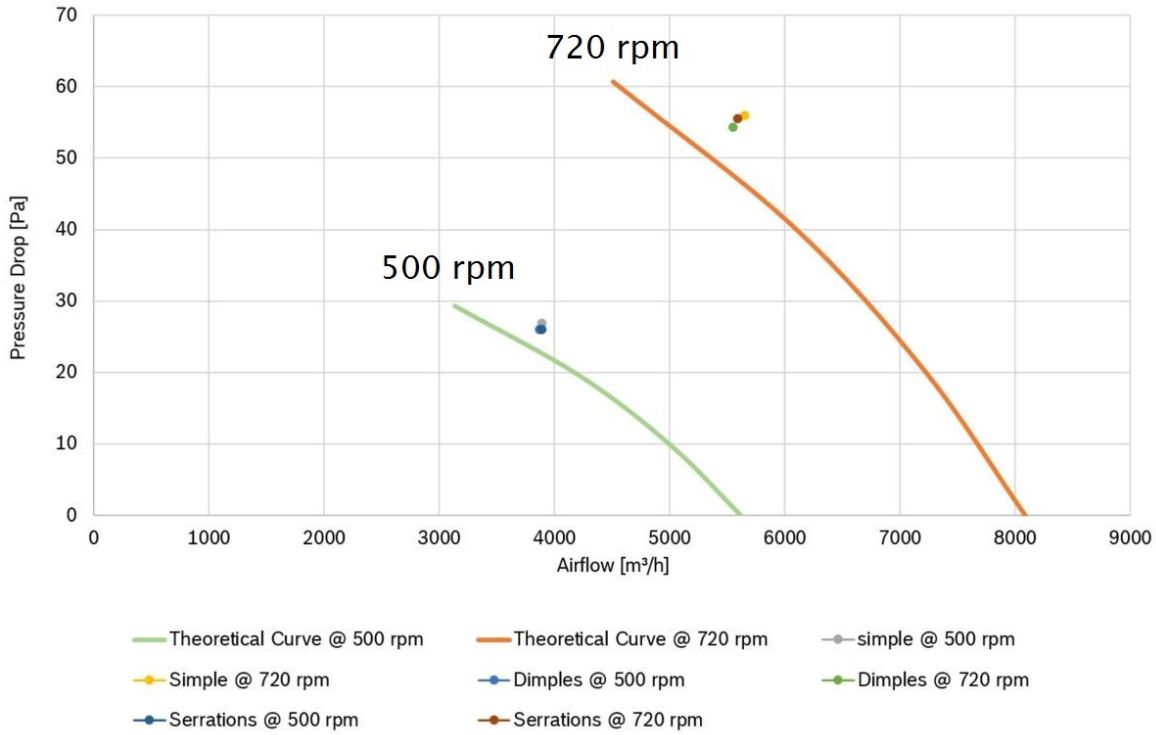

Figure 6.12: Operating points of the three models at 500 and 720 *rpm*. Theoretical Curves based on the fan's data-sheet.

Considering the aim of these kind of noise reduction features, which consist mainly in reducing flow separation, the noise benefits were not expected to be significant in the perfect operating range of the fans. Flow separation is a phenomenon which mainly manifests itself at lower airflow rates and near-stall or complete stall conditions, which correspond to operating points often not covered by the manufacturer's fan curves.

Given the lack of significant potential improvements in the serrated model, focus was shifted towards the dimples. To better understand its influence on aerodynamic noise at different operating conditions, the fan curves of the simple and dimpled fans were traced at a higher speed, 800 *rpm*, to better visualize the effect on turbulent kinetic energy and flow attachment; the results can be consulted hereafter.

800 rpm Fan Curve

The results obtained from varying the airflow rate at 800 *rpm* were compared to the theoretical fan curve. The airflow rate was changed by altering the mass-inlet-flow at the boundary condition in the CFD model. The fan curves and the evolution of the average acoustic power on the fans' surface can be observed in Figure 6.13. Table 6.2 lists the operating points used to plot the curves.

Table 6.2: Operating points and surface Acoustic Power Level (SWL) of the simple and the dimpled fan models at 800 rpm.

Model	**velocity** $[rpm]$	**Airflow** $[m^3/h]$	**Pressure Drop** $[Pa]$	**Area Avg. SWL** $[dB]$
Simple	800	1500	103,4	58,8
		2000	100,4	58,0
		2500	97,5	58,3
		3000	94,3	57,7
		3500	87,0	56,5
		4000	80,8	55,5
		4500	76,4	55,1
		5000	70,0	54,4
		5500	65,0	54,4
		6000	61,0	54,5
		6500	58,0	55,0
Dimples	800	1500	107,2	58,3
		2000	101,5	57,6
		2500	99,1	57,3
		3000	91,4	57,6
		3500	88,2	56,7
		4000	80,9	55,9
		4500	74,7	54,6
		5000	69,1	54,4
		5500	62,5	54,0
		6000	59,0	54,7
		6500	55,5	54,9

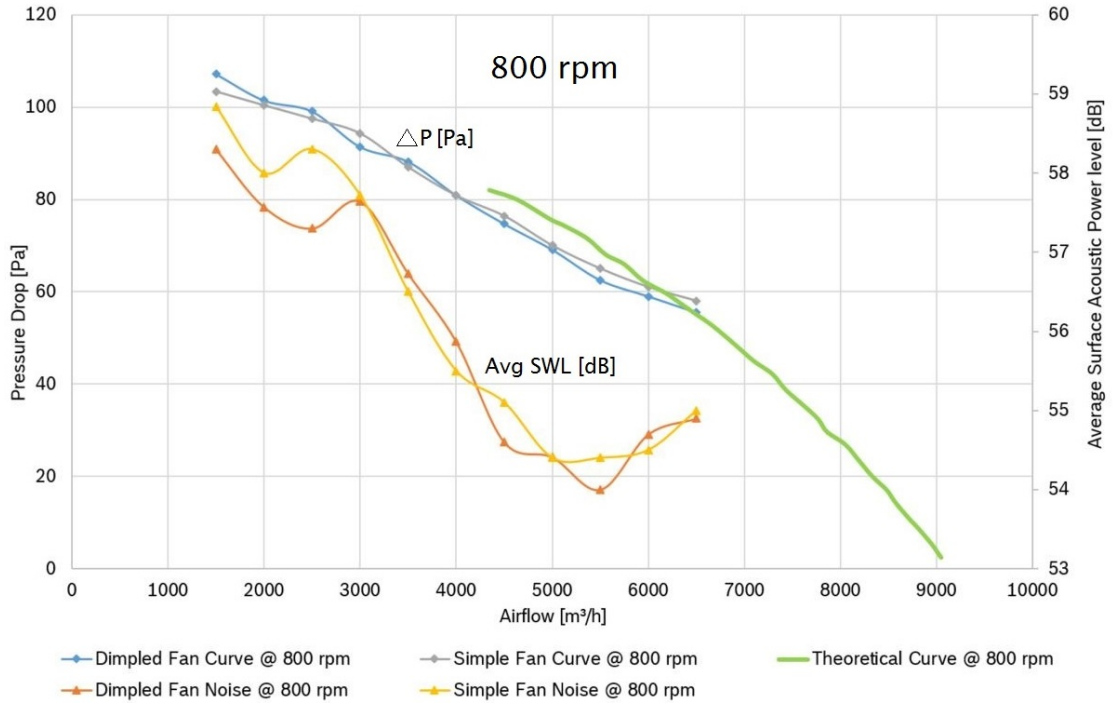

Figure 6.13: Evolution of the operating points and boundary layer noise of the simple and dimpled fans at 800 *rpm*, for different airflow rates. Theoretical Curves based on the fan's data-sheet.

In Figure 6.13 it is possible to observe that the simulation results do not deviate significantly from the theoretical curve. Unfortunately, the manufacturer does not provides data for airflow rates lower than 4000 m^3/h, which leads to associate the final point to a stall threshold.

Analyzing the fan noise curves, it is possible to see how boundary layer noise of both fan models decreases with increased airflow rate until 5000/5500 m^3/h, and increases from there on. This increase in noise levels for higher airflow rates is supported by literature, see Chapter 1.2. There is no clear consensus regarding which fan has better noise performance at the operating range (points which match the theoretical curve), since both show similar acoustic power values, considering associated numerical errors. However, at lower airflow rates, the fan noise curves behave in a curious way: they seem to reach a noise peak followed by a small dip, to then increase once again. The dimpled fan even seems to anticipate this behavior when compared to the simple fan: at 3000 m^3/h both models denote an average surface acoustic power of around 58 dB, but at 2500 m^3/h a considerable difference in the boundary layer noise can be observed. From this point on, the dimpled fan has lower average dB levels on its surface for the lower airflow rates.

To better understand the effect of the dimples, the airflow rates of 2500 and 5000 m^3/h were chosen as visualization examples, given the accentuated noise difference at the lower rate and the same obtained average noise value at the higher rate. Figures 6.14 to 6.17 show how the turbulent kinetic energy and the axial velocity behave for both models, at both operating points.

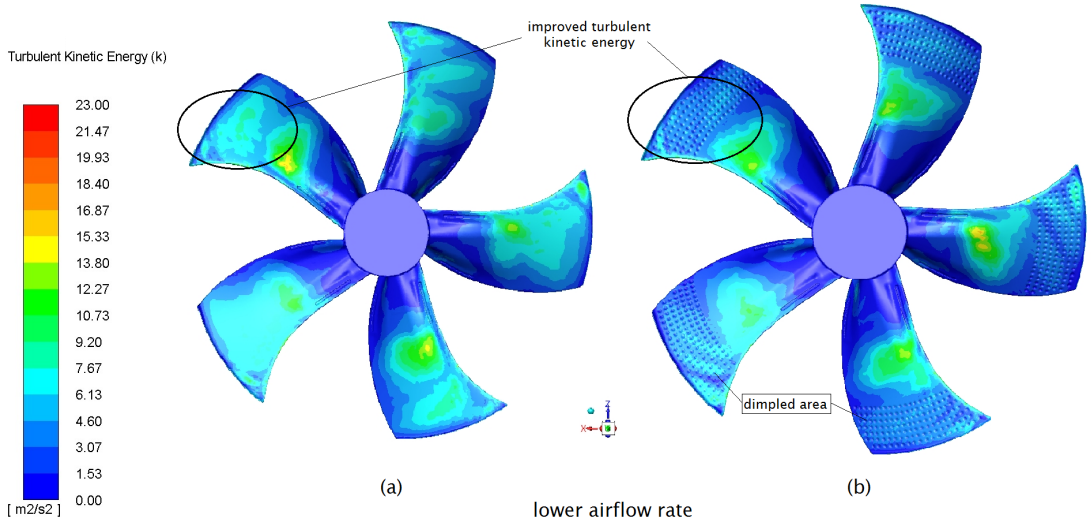

Figure 6.14: Turbulent kinetic energy contours (k) on the suction side of a) the simple fan avg k of 3,01 m^2/s^2 b) the dimpled fan avg k of 2,58 m^2/s^2 at 800 rpm and 2500 m^3/h.

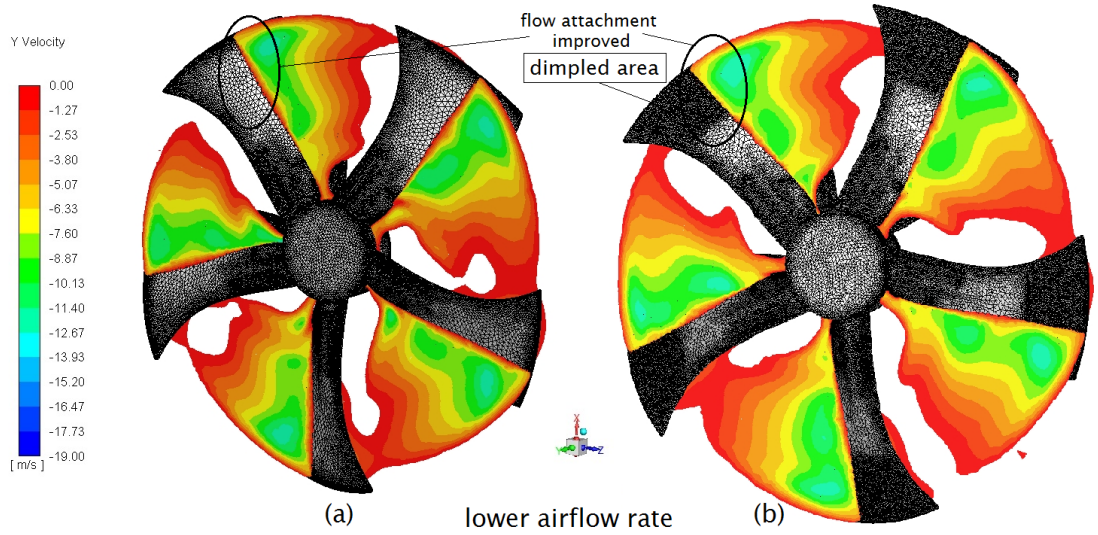

Figure 6.15: Axial velocity (Y) contours on the suction side of a) the simple fan b) the dimpled fan at 800 rpm and 2500 m^3/h.

Figures 6.14 and 6.15 show clear improvements using the fan model with dimples; lower turbulent kinetic energy values are registered at the dimpled area of the suction side and less stationary axial flow is seen on the blade's surface, which is an indication of delayed flow separation in the region. The high turbulence observed on the simple fan in Figure 6.14 is an indication that stall condition is most likely present.

The same effects, although to less extent, can be observed at 5000 m^3/h, a point that shares the same average noise level for both fans and, contrary to the previous point, is part of the theoretical operating range for the fan.

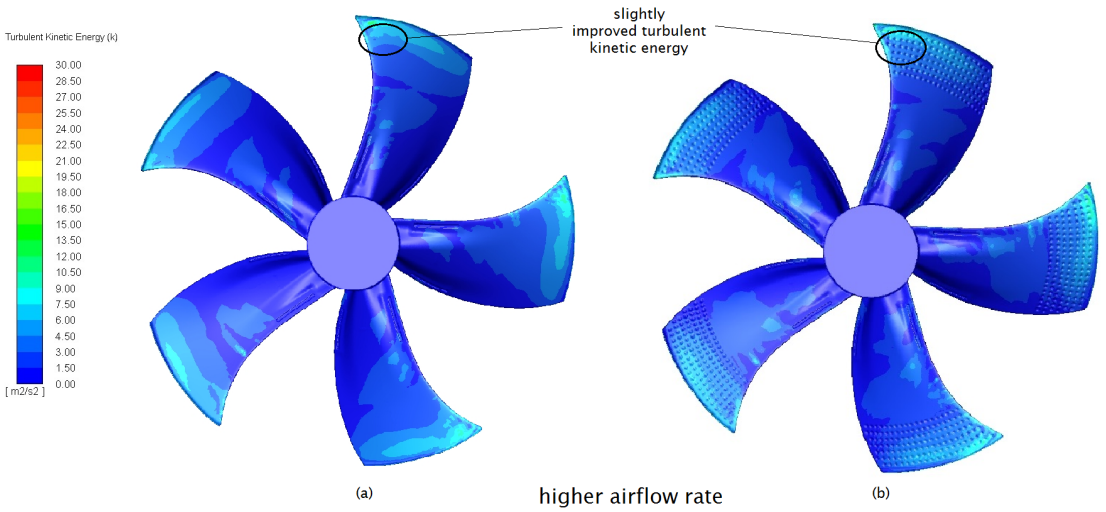

Figure 6.16: Turbulent kinetic energy contours (k) on the suction side of a) the simple fan avg k of 1,80 m^2/s^2 b) the dimpled fan avg k of 1,67 m^2/s^2 at 800 rpm and 5000 m^3/h.

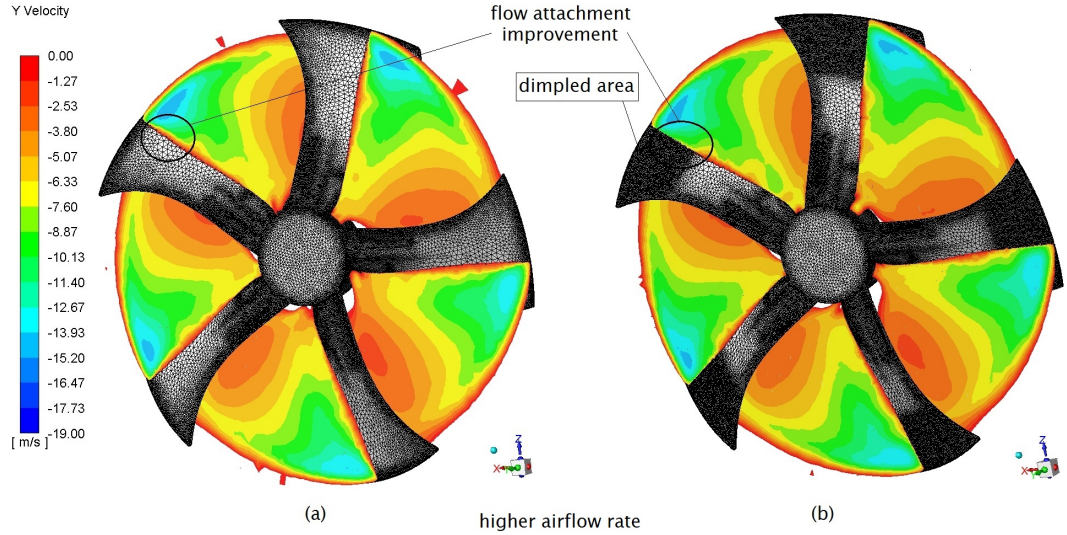

Figure 6.17: Axial velocity (Y) contours on the suction side of a) the simple fan b) the dimpled fan at 800 rpm and 5000 m^3/h.

Although the average surface acoustic power level on both fans is the same at 5000 m^3/h, the contours in Figure 6.17 indicate better flow attachment with the dimpled fan. Figure 6.16 also shows a slight improvement in the turbulent energy distribution, with an average turbulent kinetic energy lower for on the dimpled fan.

These two cases are a clear indication that the dimples are effective in counteracting flow separation. However, at a normal operating point of the fan, the noise benefits are barely significant because flow separation is not the most significant noise source of this fan model. Yet, it is possible to conclude that dimples do confer momentum at the suction side boundary layer flow and prevents the turbulence that apparently advents from flow separation.

A theory is hereby proposed to explain the fan dimples effect on the fan: the flow turbulence is better dissipated with the dimples; the larger eddies, which are generated during the suction side vortex-roll up and flow separation turbulence, are easily dissipated into smaller eddies, which have the lowest energy content [48], due to the dimples' cavities; as a result, the dimples spread the turbulent energy content of the flow along the suction side surface, in a way that creates less critical turbulent kinetic energy regions. For noise, the lower turbulent values on the suction side promote less boundary layer noise due to less accentuated velocity and pressure fluctuations on the surface.

To summarize, the dimples generate small-scale turbulence on the suction side region, providing beneficial energy dissipation capacity.

6.3 CFD model: Features applied to the Heat Pump

On a final approach, the three fan models were used within the heat pump environment, using the same mesh sizing and techniques as described in Chapter 4.1.1, and compared to previously obtained data from Chapter 4. The resulting mesh was unable to catch the details of the dimples and the serrations as well as with the refined mesh used in the free flow condition models.

Since the small-chassis unit with the bigger fan was used as the CFD environment, the analyzed speeds were 365 and 510 *rpm* and also the classic high speed mode of the original range, 720 *rpm*, to guarantee a wider spectrum of rotational velocities for the study.

The same fan models shown in Figure 6.3 were inserted in the small-chassis.

6.3.1 Results

The obtained results can be consulted in Table 6.3.

Table 6.3: Operating points and surface Acoustic Power Level (SWL) for the three fan models inserted in the heat pump unit.

Model	**velocity** [rpm]	**Airflow** [m^3/h]	**Pressure Drop** [Pa]	**Area Avg. SWL** [dB]	**Max. SWL** [dB]
Simple	365	1821,6	16,3	36,8	59,5
	510	2656,8	31,0	43,9	67,0
	720	3852,0	60,5	51,1	74,7
Dimples	365	1814,4	16,3	36,5	59,7
	510	2592,0	31,1	43,9	67,8
	720	3798,0	60,2	51,1	74,5
Serrations	365	1828,8	16,3	36,4	61,9
	510	2646,0	31,5	43,8	68,3
	720	3823,2	60,7	51,2	76,1

Figures 6.18, 6.19 and 6.20 plot the average surface Acoustic Power Level of the three models in the heat pump context as a function of airflow, at different speed modes. From Table 6.3 and the figures 6.18 and 6.20, it can be observed that the serrations registered

the best improvement at 365 and 510 *rpm* with 0,4 and 0,1 *dB* potential, while also revealing 0,1 *dB* higher levels than the other models at 720 *rpm*.

From analysis of the above stated data, it is not possible to draw a concrete conclusion; the noise improvements vary from 0,1 to 0,4 *dB* which, considering the numerical error, is not good enough to serve as support to any statements.

In free flow conditions, using a finer mesh, the features applied to the fan showed higher impact on aerodynamic noise, whilst inside the heat pump environment no relevant conclusions can be drawn. The connection chamber's geometry, the evaporator's induced pressure drop and the difference in the outlet domain influence the flow behavior and the formation of turbulence and vortexes.

The lack of noise improvement in these models can also be due to the less refined mesh. However, although beneficial in diminishing turbulent kinetic energy and flow separation, these features do not act against the major sources of fan noise in the heat pump context, namely the reverse flows and the vortex roll-up in the tip clearance.

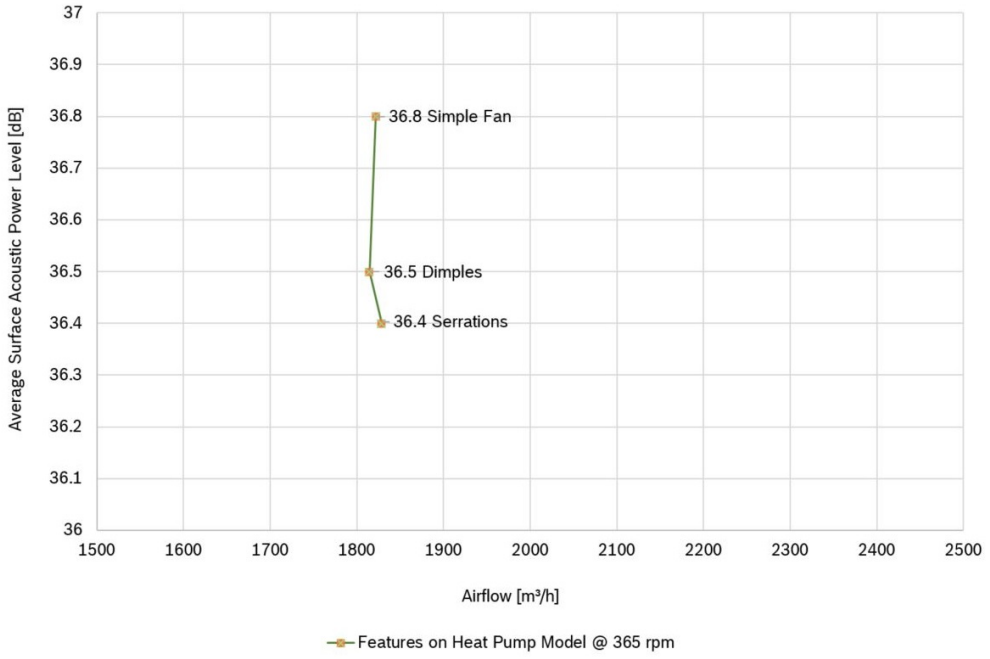

Figure 6.18: Average Surface acoustic power levels as a function of airflow on the three fan models, at 365 *rpm*, small-chassis unit.

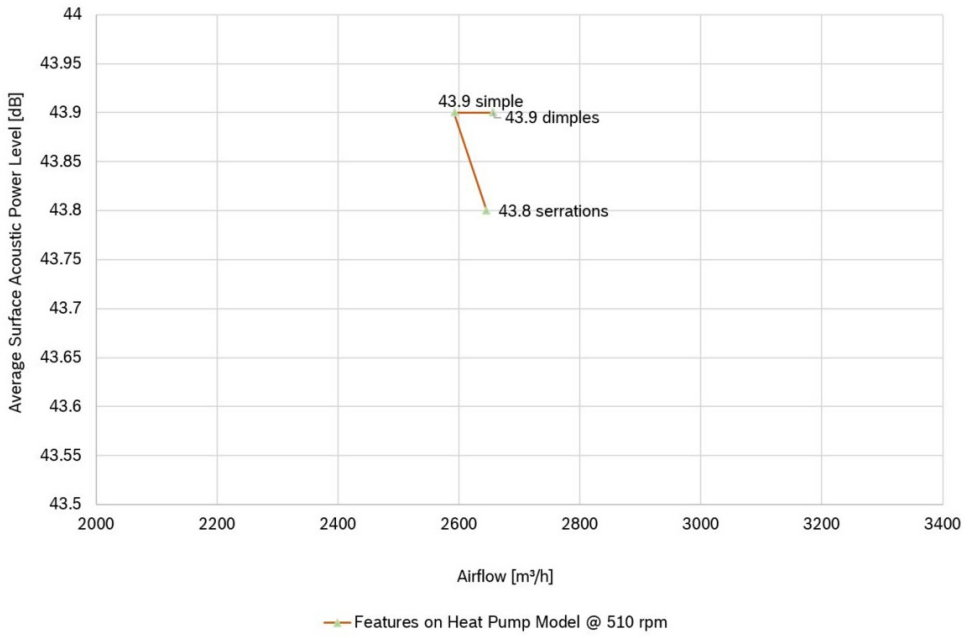

Figure 6.19: Average Surface acoustic power levels as a function of airflow on the three fan models, at 510 *rpm*, small-chassis unit.

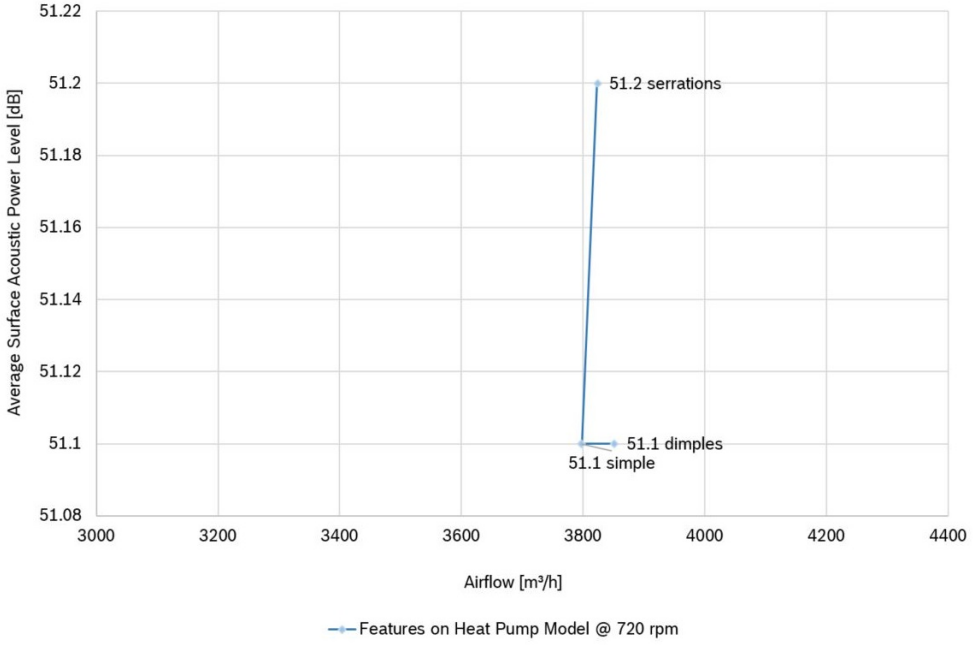

Figure 6.20: Average Surface acoustic power levels as a function of airflow on the three fan models, at 720 *rpm*, small-chassis unit.

6.4 Conclusions

Given the results obtained with the three fan models analyzed in this chapter, the following conclusions can be drawn:

- The dimples show a positive effect on flow separation, motivating the interest for further investigations;
- The proposed theory for the dimples states that the cavities dissipate the turbulent energy content of the flow along the increased surface area, resulting in less accentuated velocity and pressure fluctuations and thus less aerodynamic noise in the boundary layer;
- The dimples show similar flow separation improvements as registered in literature using the serrated edges [37];
- The lack of substantial improvements on the noise levels of the three models applied to the small-chassis leads to believe these features do not act against the major sources of fan noise in the heat pump context;
- For the current operating points of the fans in the heat pump units, there would be little to no benefit in adding dimples on the fan. However, for eventual applications requiring lower rotational speeds, the dimples could effectively provide boundary layer noise benefits by improving flow attachment. Any kind of application with low airflow needs (rates in the near-stall or stall region) could benefit from this (or a similar) feature, as they demonstrate better aeroacoustics at the targeted operating range by delaying flow separation.
- Between the dimples and the serrated edges, producing cavities on the fan's surfaces is probably easier and more cost-effective for production than the extremely sharp serrations, considering injection moulding as the manufacturing process, however some care shall be taken due to the local reduction of thickness in the dimple areas, which can reduce the tip stiffness of the blades.

Chapter 7

Experimental Study

Experimental measurements were performed on the three models analyzed in Chapter 6, with the main goal of evaluating the influence of the serrated edges and the dimples on fan noise, while providing the same airflow rate.

The experimental study consisted in measuring the airflow using an enthalpic tunnel, and the Acoustic Power Level in a hemi-anechoic chamber, of 3D printed re-scaled versions of the ⌀500 fan model. The experiments were conducted using the ⌀500 fan rather than the ⌀630 model due to size limitations of the available 3D printer. The dimples and the serrations were, therefore, applied to the smaller fan; the only difference in the features' size consists in an offset of 15 mm of the trailing edge spline, instead of the 12 mm mentioned in Chapter 6.2.2.

7.1 Model Prototyping and Experimental Setup

The fans for this experimental study were reduced in size using a 50% scale from the original size, resulting in a diameter of ⌀250 mm, and printed in a Connex MultiJet 3D printer using ABS as printing material. The prototypes can be seen in figures 7.1, 7.2 and 7.3. Unfortunately, the triangulation of the *stereolithography* format file was less refined for the simple fan than for the other prototypes, therefore, it shows lower surface quality.

A central aluminium hub was inserted in each fan model, after 3D printing process, to provide an efficient connection to the axe of the electric motor used to run the fan.

Connex MultiJet 3D printer uses Multi Jet Printing (MJP) technology; MJP is an inkjet printing process that uses piezo printheads to deposit photocurable materials, while also using a dissolvable or meltable support material to facilitate post-processing [49]. Its good resolution allows for complex geometries to be printed with relatively good surface quality.

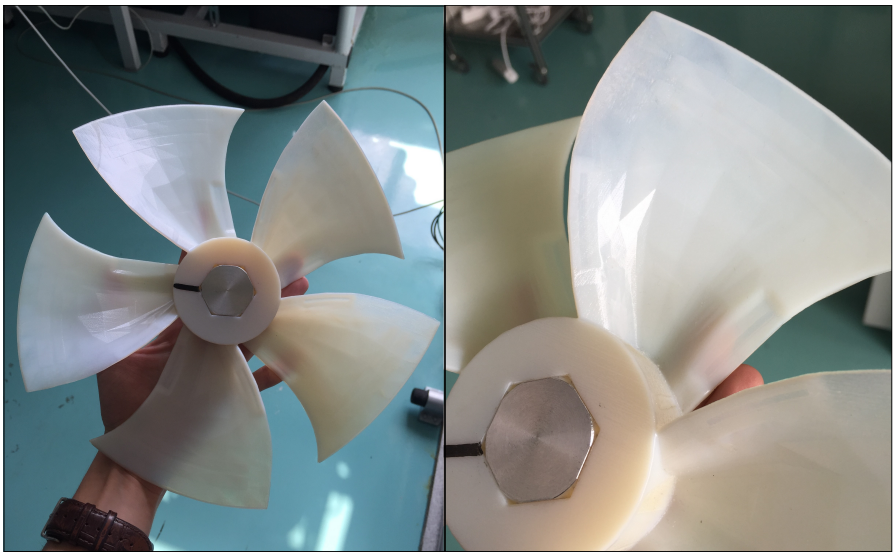

Figure 7.1: Simple fan prototype. (Note the rough triangulation on the surfaces)

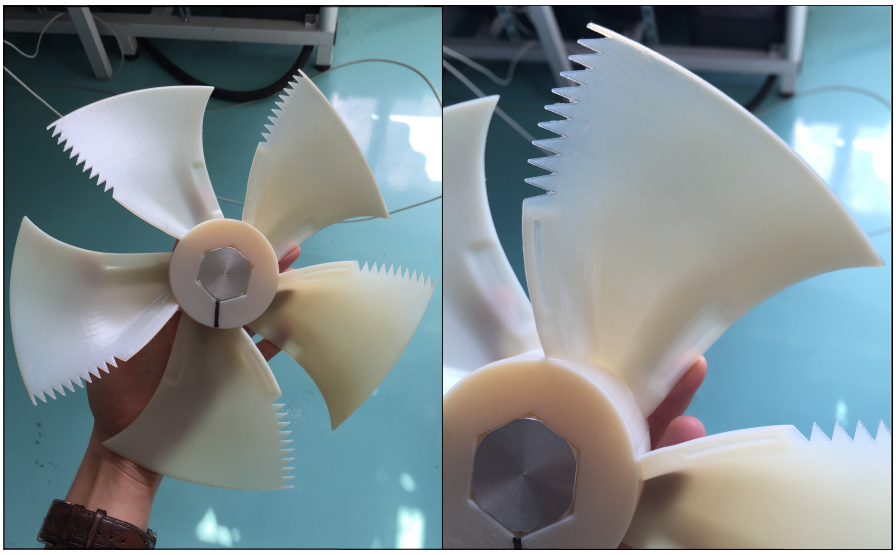

Figure 7.2: Fan prototype with serrated edges.

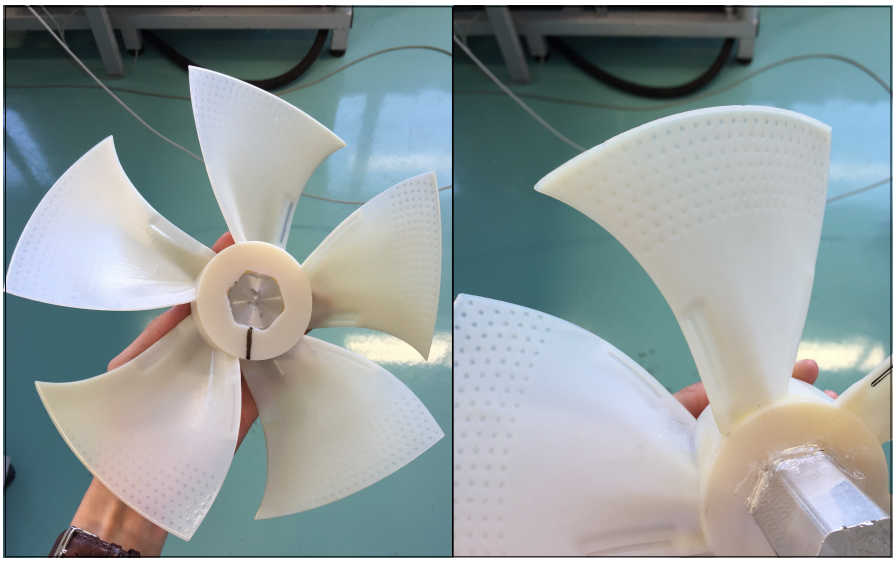

Figure 7.3: Fan prototype with dimples on the suction side.

The experimental setups for the airflow rate measurements and the acoustics study were very similar. To recreate the vortex roll-up noise effect, a metal shroud was included in the experimental setup. A wood panel was used to include the shroud and support the motor fixture. The motor fixture includes a steel motor ring and four support arms, which were welded to the motor ring using a shielded metal arc. The arms were bolted to the wood panel using four M8 bolts. The motor shaft was connected to the fan with an hexagonal metal hub, as indicated before.

The assembly was fixed to the entrance of the enthalpic tunnel, as can be seen in Figure 7.4. Figure 7.5 exposes the motor fixture in more detail.

The fans were powered by a 12 V DC GBM-S Bosch Motor. A potentiometer was used to control the speed of the shaft rotation. The wiring diagram can be seen in Figure 7.6.

The technical drawings of the parts can be found in Appendix B.

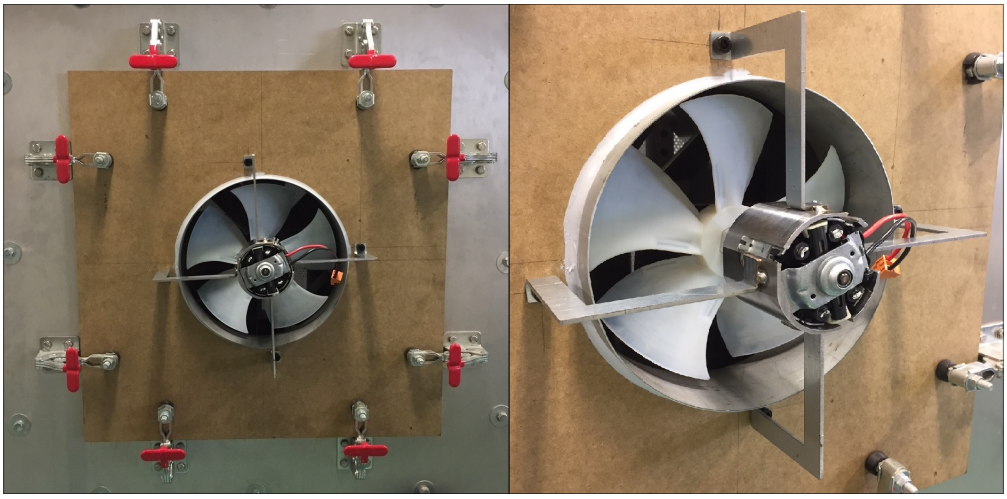

Figure 7.4: Assembly fixed in the enthalpic tunnel.

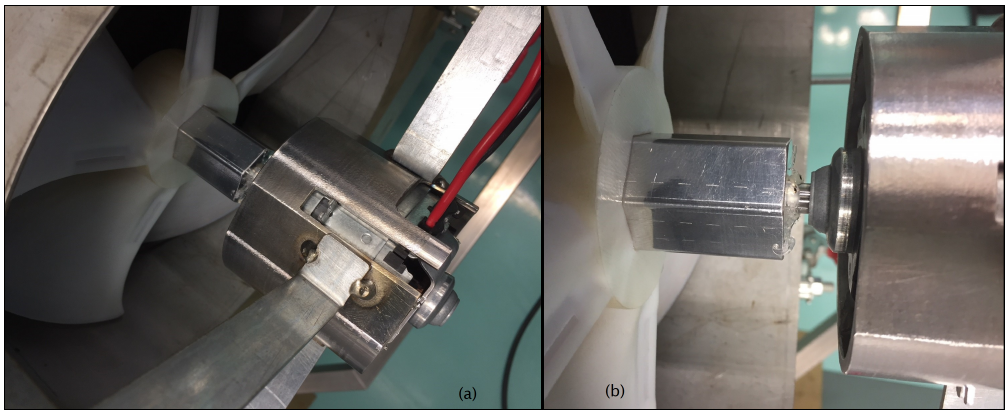

Figure 7.5: Details of the setup a) motor fixture: support arms welded to the motor ring b) hexagonal fan hub pressed and glued to the motor shaft.

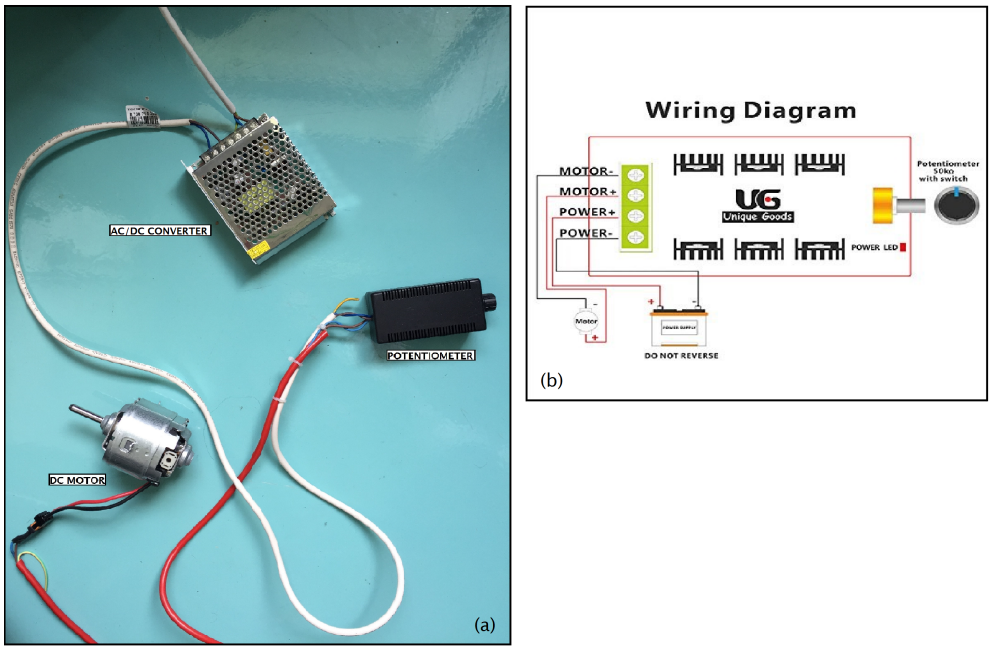

Figure 7.6: Wiring diagram of the potentiometer a) experimental setup b) schematic diagram [50].

7.2 Measurements

To measure the Acoustic Power Level of the fans in the hemi-anechoic chamber, the speed and airflow were measured first to guarantee a fair comparison between the three models. The airflow was measured in an enthalpic tunnel for different rotation velocities: 350, 500, 600, 720, 800 *rpm*. Speed was adjusted using a potentiometer and a stroboscopic light. The fans rotation speed were assumed the same as the ones indicated by the device when the flashes of light occurred at the same frequency of the revolutions of the fan, providing a steady image of the fan whilst illuminated by the flashes.

Unfortunately, the enthalpic tunnel incorporates guide vanes and filters which influence the airflow measurements and induce pressure drops across the flow path. Therefore, the measurements taken inside the tunnel were solemnly used to verify that all three models were moving the same airflow rate; no validation could be conducted for the scaling factor.

The results can be consulted hereafter. Unfortunately, the simple fan and the fan with dimples were damaged during the process of machining the hexagonal hole. Although the broken pieces were glued together, the crack lines are expected to have a negative effect on overall noise performance.

7.2.1 Airflow Rate

The fans' airflow rate were measured at 350, 500, 600, 720 and 800 *rpm* in the enthalpic tunnel as shown in Figure 7.7. The fan was powered before initiating the test and the speed was adjusted to the desired level. Data was collected during three minutes and the mean value of the obtained registers was registered. The results are exposed in Table 7.1. The tunnel uses Tescor Code Tester software.

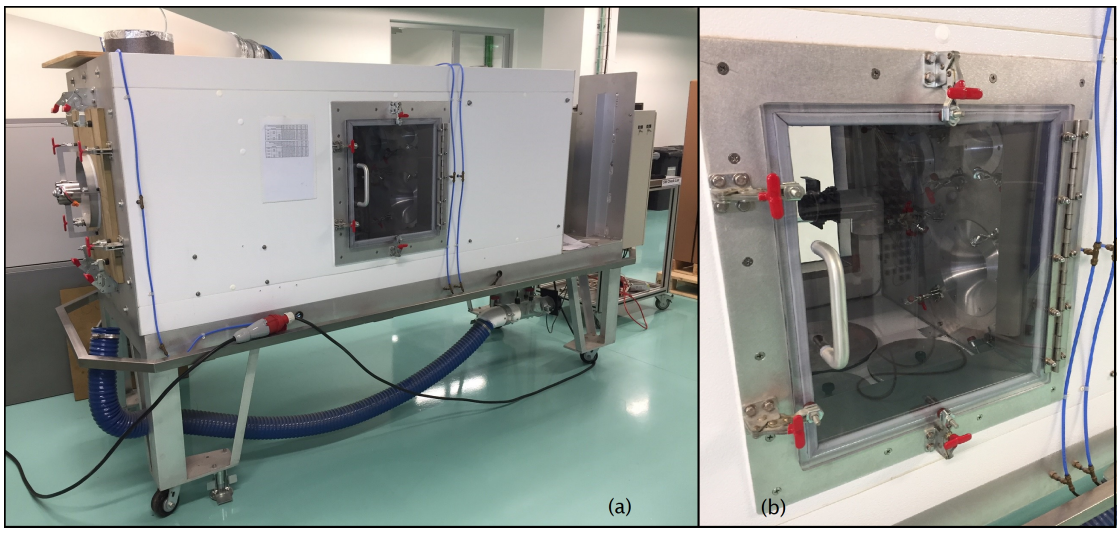

Figure 7.7: Enthalpic Tunnel Blower a) overview b) nozzles which measure airflow rate.

Table 7.1: Airflow rates measured inside the enthalpic tunnel using the ⌀500 re-scaled fan models.

Model	**Diameter** $[mm]$	**Velocity** $[rpm]$	**Airflow** $[m^3/h]$
Simple	250	350	138,0
		500	173,5
		600	198,0
		720	231,0
		800	253,0
Dimples	250	350	138,2
		500	173,2
		600	200,1
		720	231,8
		800	253,8
Serrations	250	350	133,0
		500	171,5
		600	195,5
		720	228,0
		800	248,7

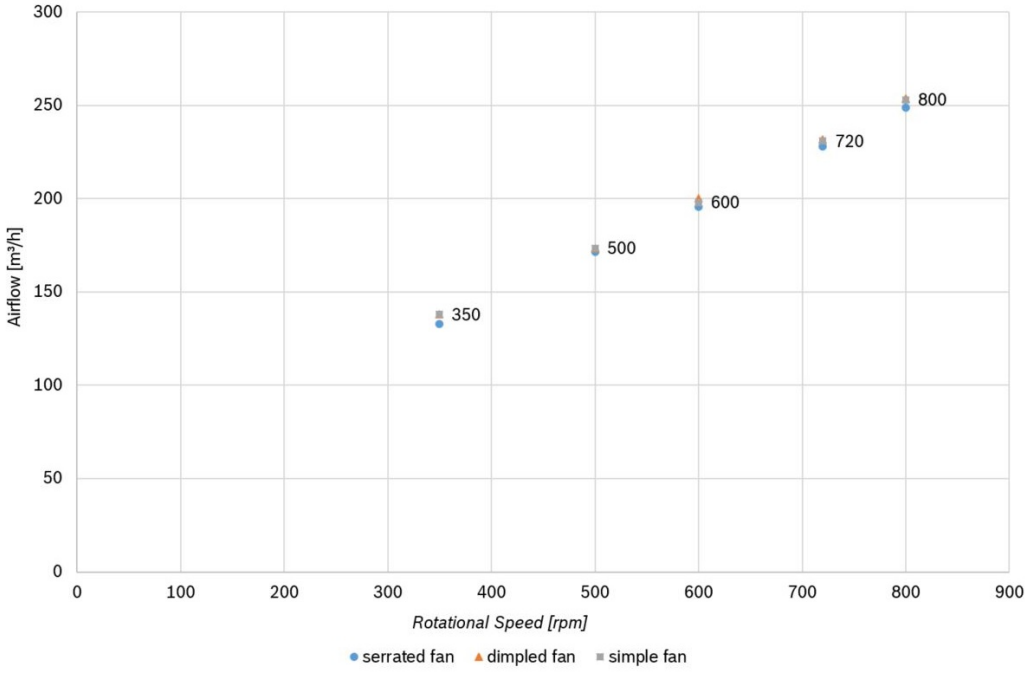

Figure 7.8: Obtained airflow measurements of the three prototypes at the specified range of speeds.

7.2.2 Acoustics

The acoustic measurements were conducted inside Bosch's hemi-anechoic chamber. The setup was fixed to a metallic frame, see Figure 7.9. A schematic representation of the

microphones' location inside the chamber can be seen in Figure 7.10.

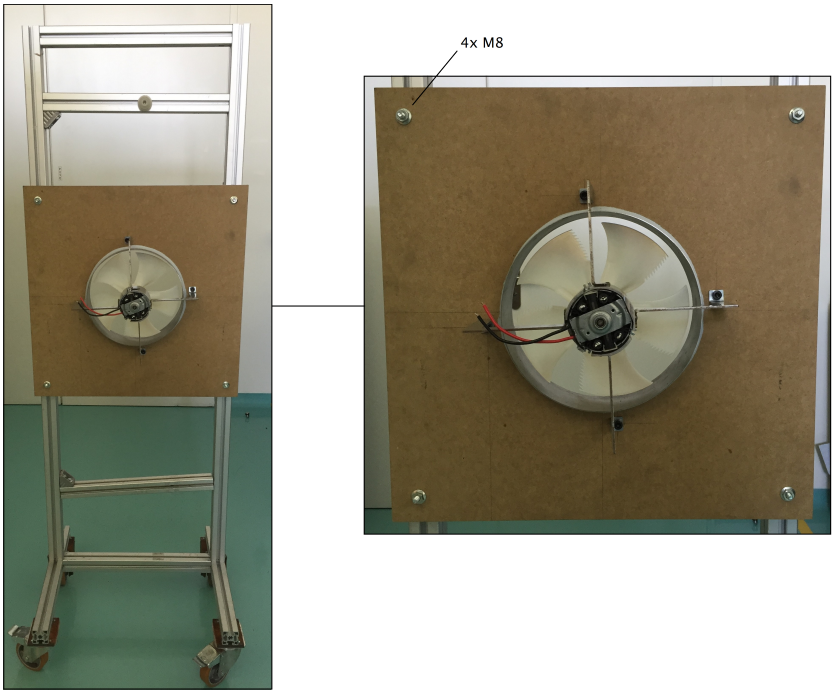

Figure 7.9: Setup for sound measurements: the metallic frame was placed in the center of the hemi-anechoic chamber.

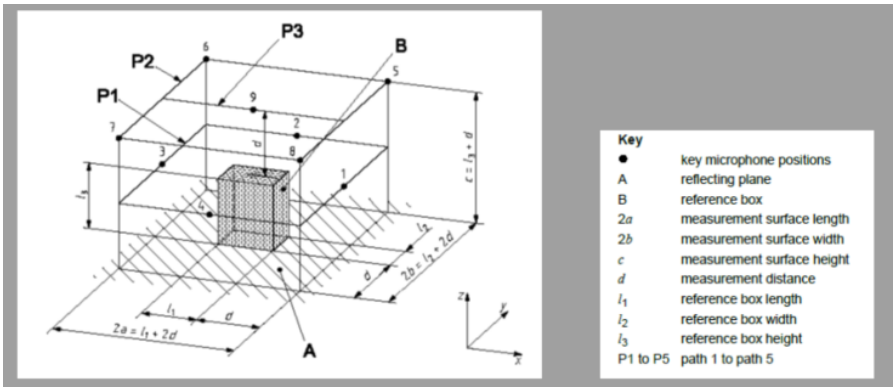

Figure 7.10: Microphones' distribution and setup inside the hemi-anechoic chamber: microphone 1 and 3 distance 1 m from the center; microphones 2 and 4 distance 1,22 m; 1,17 m distance from the floor to the center and 1,23 m from center to microphone 9. Overall dimensions are 2,5x2,5x2,5 m.

The Sound Pressure Level testing was conducted according to ISO 3744, with microphones calibrated to 94 dB by Rion Sound Calibrator NC-74 at 1000Hz. HeadLab Compact 24 + 12 channel module data acquisition equipment was used, with a measuring frequency range between 1Hz and 24kHz. Sound Power Level measurements were taken using 9 PCB ICP microphones (378B02) with windshield mounting (Audio CA132), ranged between 20Hz and 20kHz. The data acquisition system uses HEAD Acoustics

8.1 software with FFT resolution of 4096 points. The results can be consulted in Table 7.2. Figures 7.11 to 7.15 plot the frequency and the sound pressure level $dB(A)$(SPL) of the three fan models from 350 to 800 rpm. Figures 7.16 to 7.18 show the time and frequency response of a speed rap-up from 0 to sensibly 800 rpm of the three fan models.

Table 7.2: Far-field Sound Pressure Level measured inside the hemi-anechoic chamber.

Model	**Diameter** $[mm]$	**Velocity** $[rpm]$	**SPL** $[dB(A)]$
Simple	250	350	60,9
		500	62,0
		600	63,2
		720	64,2
		800	66,1
Dimples	250	350	57,2
		500	62,0
		600	62,7
		720	64,9
		800	66,3
Serrations	250	350	55,6
		500	58,2
		600	60,0
		720	62,7
		800	65,5

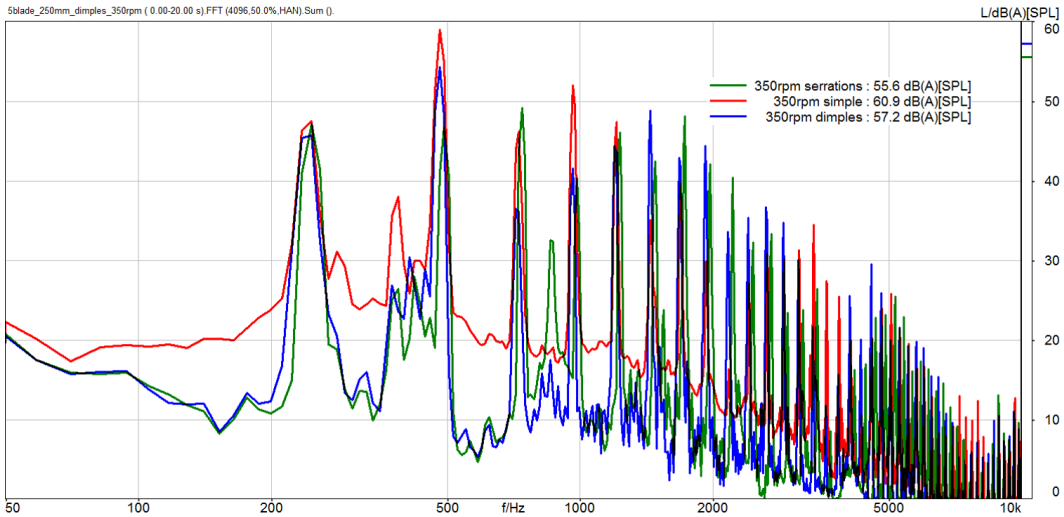

Figure 7.11: FFT of the three 3D printed fan models rotating at 350 rpm showing A-weighted sound pressure levels $dB(A)$(SPL).

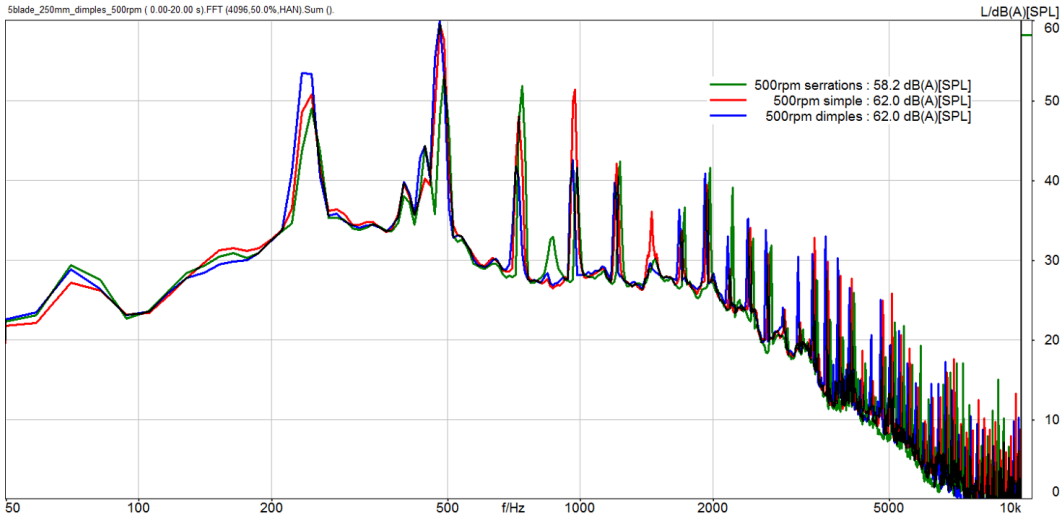

Figure 7.12: FFT of the three 3D printed fan models rotating at 500 *rpm* showing A-weighted sound pressure levels $dB(A)$(SPL).

At lower speeds, A-weighted sound pressure level improvements can be seen using the serrated and the dimpled fan, when compared to the reference model. It is possible to observe how the 900Hz peak is more significant in the simple model, which can be due to the differences in the surface quality of this prototype.

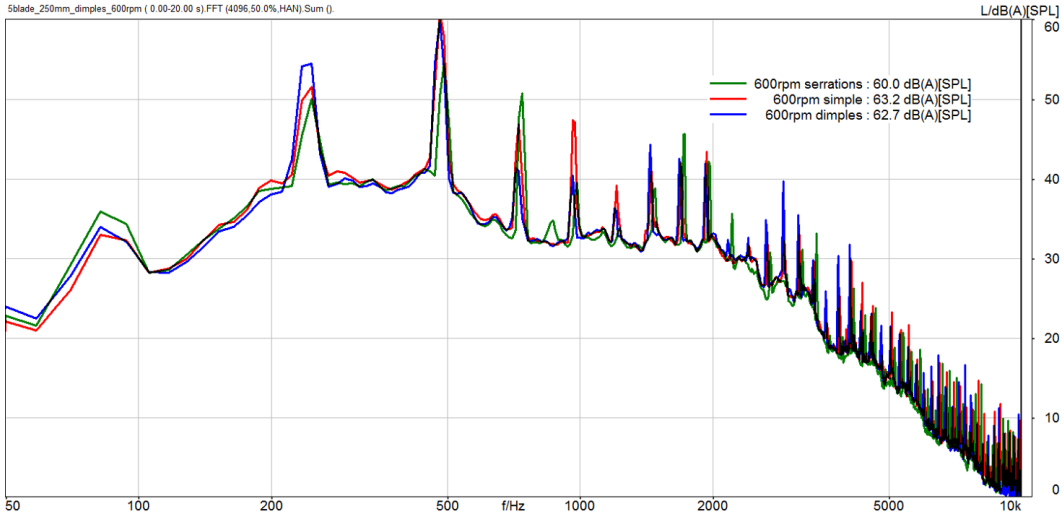

Figure 7.13: FFT of the three 3D printed fan models rotating at 600 *rpm* showing A-weighted sound pressure levels $dB(A)$(SPL).

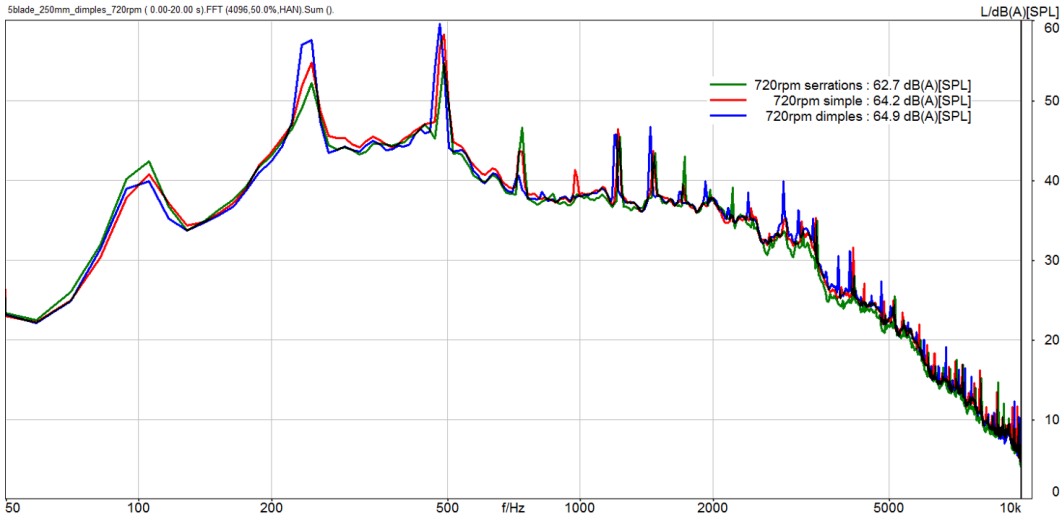

Figure 7.14: FFT of the three 3D printed fan models rotating at 720 *rpm* showing A-weighted sound pressure levels $dB(A)$(SPL).

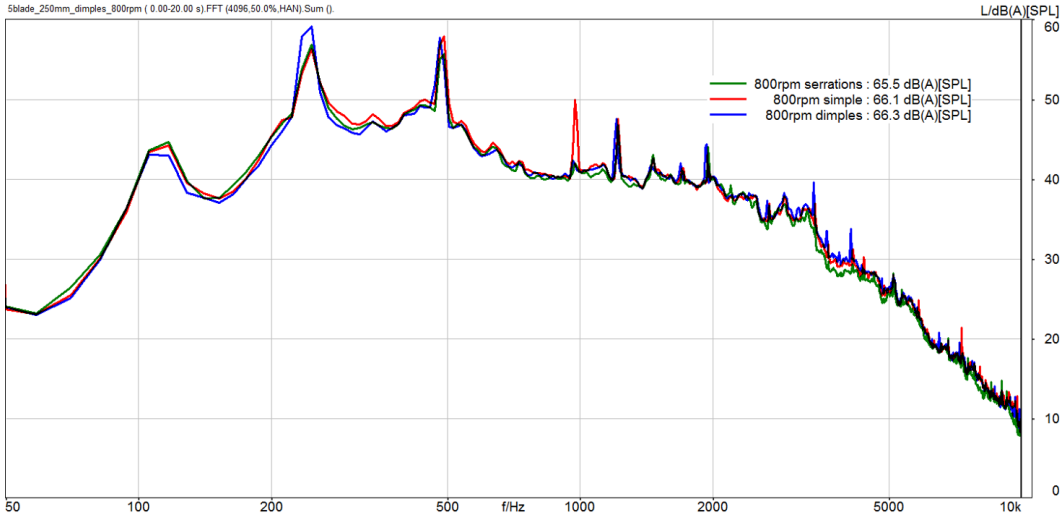

Figure 7.15: FFT of the three 3D printed fan models rotating at 800 *rpm* showing A-weighted sound pressure levels $dB(A)$(SPL).

From the frequency response of the measured rotation speed range, it is possible to identify several tones that remain constant with speed increase. These frequencies correspond to the PWM controller noise that runs the DC motor, due to the pulses and variations of the motor's duty cycle introduced by the PWM speed control.

A ramp-up test from 0 to roughly 800 *rpm* was performed on each prototype and can be seen in figures 7.16, 7.17 and 7.18.

In these images, it is possible to observe the similar acoustic behavior of the three prototypes during a gradual increase in speed. It is possible to see how the critical noise frequencies range between 100Hz and 750Hz and how the spikes of the PWM controller manifest themselves equality in all models, independent of the velocity. On the right side of the images, it is possible to observe the fans' noise spectrum at 800 *rpm*.

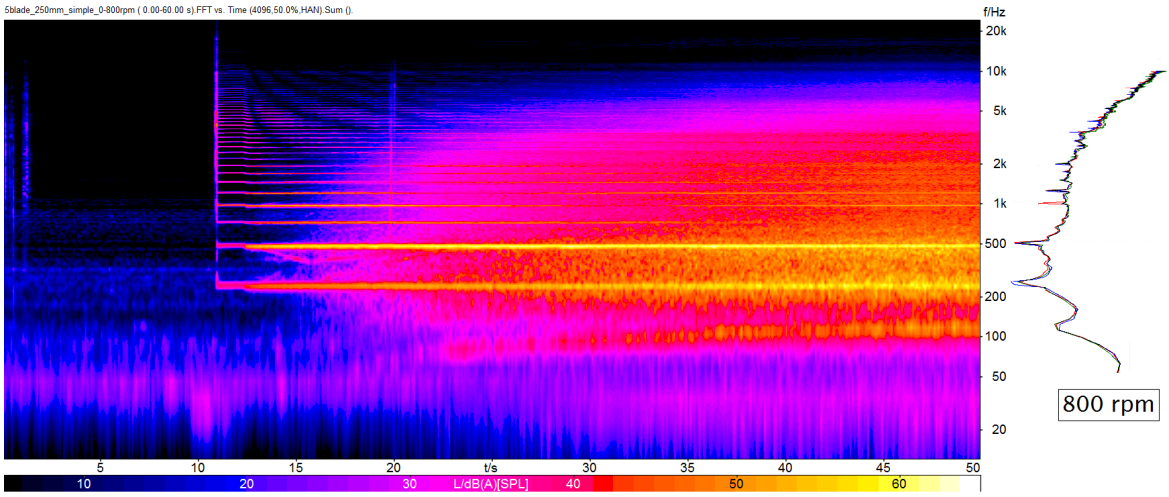

Figure 7.16: FFT vs time response of a 50 seconds long speed ramp-up test from 0 to roughly 800 *rpm* - simple model.

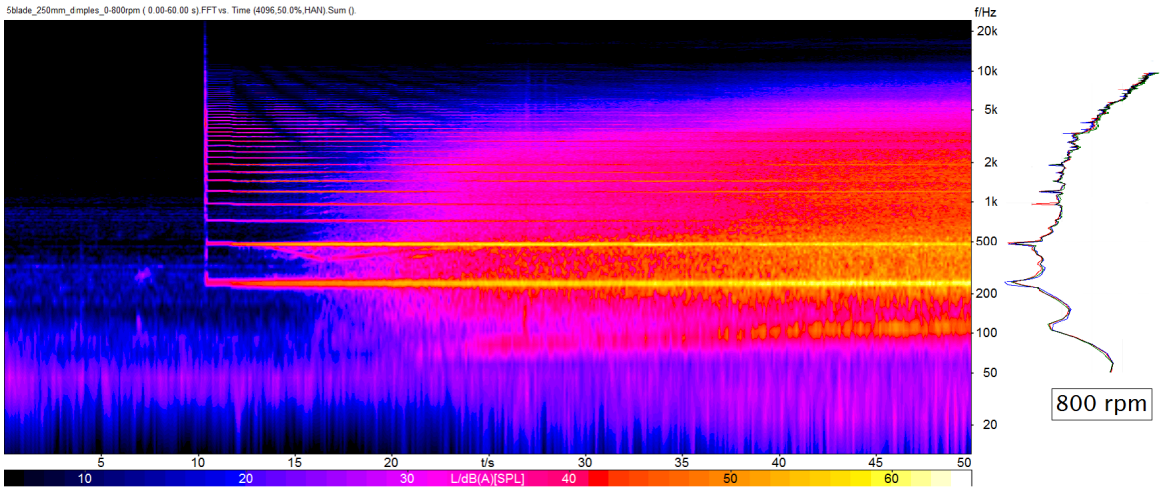

Figure 7.17: FFT vs time response of a 50 seconds long speed ramp-up test from 0 to roughly 800 *rpm* - dimpled model.

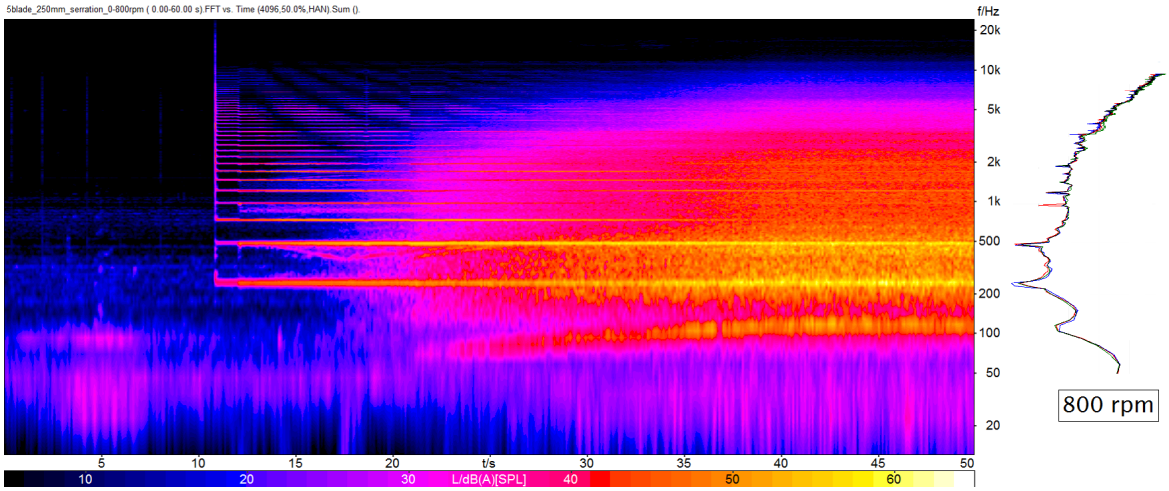

Figure 7.18: FFT vs time response of a 50 seconds long speed ramp-up test from 0 to roughly 800 *rpm* - serrated model.

7.3 Conclusions

The following conclusions can be drawn from the experimental studies regarding airflow rate and noise levels of the fan prototypes:

- The noise reduction features did not change the airflow rate of the fan prototype;
- The difference between the surface quality of the simple model and the fans with dimples and serrations has, most likely, a considerable influence on the aerodynamic noise due to irregularities on the surface that can cause non-beneficial turbulence in the boundary layer;
- The damaged parts of the simple model and the fan with dimples are also likely to have forged the results;
- Still, the overall noise spectrum of the fans are coherent and increase noise levels with increased speed; tonal noises due to the PWM controller can be found and are mostly dominant for rotation speed ranges under 600 *rpm*. Above this threshold, the airflow noise overcomes the noise due to electronics.
- In the theoretical near-stall condition, 350 *rpm*, the fans with serrated edges and with dimples reveal noise improvements of 5,3 and 3,7 $dB(A)$, respectively, when compared to the reference fan, although its rough surface quality could be responsible for most of this difference.
- At higher speeds, the noise improvement for the fans with noise reduction features decreases, as expected in theory. The fan with dimples even registered higher noise levels at 720 and 800 *rpm*, although it is important to enhance it was a damaged model.
- To truly evaluate the noise reduction potential of these models, new measurements should be performed with new, undamaged fans with equal surface quality. Still,

there is potential for possible noise reduction using these features, given the obtained results at lower speeds.

Chapter 8

Summary and Future Work

"I'm smart enough to know that I'm dumb."
Richard Feynman

8.1 Concluding Remarks

Within the workflow of this thesis, an analysis of aerodynamic noise on heat pump fans was concluded. The two fan models were studied in terms of diameter and tip speed acoustics, of the motor cap influence on downstream fan flow and also in regard to noise reduction features.

From the first analysis, it became apparent how tip speed has a profound impact on the boundary layer noise of the fans and how a bigger fan, rotating at lower speed, could imply aeroacoustic benefits for overall heat pump noise. This implies that the rotating velocity impacts the boundary layer noise to greater extent than the increase in rotor diameter, at the analyzed operating conditions.

It was also found that the motor cap prevents reverse flow, downstream of the fan, from interacting with the rotating flow, thus improving aerodynamic noise mainly on the fan blades' roots. A reduction of 15% in the cap diameter showed best noise improvement potential for the ⌀500 fan model, by conferring the acoustic benefits without implying a substantial change in its operating point.

Regarding the final part of the investigation, including dimples on the upper span suction side of the ⌀630 fan showed great potential for flow separation prevention and turbulent kinetic energy dissipation. The serrations did not reveal much noise improvement applied to the Ebm-papst fan.

Unfortunately, within the heat pump environment, no relevant benefits could be observed using the noise reduction features. Considering that the flow separation is not the main source of aeroacoustic noise, this results is not surprising. Also, it is important to note that a more coarse mesh was used in this CFD model, when compared to the free flow model.

In regard to the experimental measurements, given the damages and the low superficial quality of the reference model, no conclusions can be drawn with confidence. The fan with serrated edges registered a 5,3 $dB(A)$ noise improvement at 350 rpm. Small improvements can also be seen using the fan with dimples, also at the lower speed range,

with a 3,7 $dB(A)$ noise reduction, although some considerable extent of this improvement could be due to the lower superficial quality of the reference fan. The higher the speed of the fans, the lower the noise improvements registered with the noise reduction features, which is aligned with theoretical expectations.

8.2 Future Work Suggestions

There are a few future work suggestions worth mentioning for other researchers who wish to further analyze aeroacoustic improvements on the heat pump units.

The possibility of using bigger fans for lower airflow requirements shows promising aeroacoustic benefits, however it is necessary to evaluate both models at the exact same operating point; therefore, the suggestion is to simulate the fans within the heat pump unit and modify the resistance on the evaporator for the bigger fan, in order to cause the same pressure drop as in the preceding model.

Regarding the motor cap analysis, the proposal is to study a motor cap which could be designed to fit the motor on its hole, encapsulating it with a conical wall, creating therefore a smoother passage for the outlet air and avoiding fluid accumulation near the motor's external end.

Finally, taking into consideration the aeroacoustic improvements registered for the dimpled fan model, further investigation could be performed on the location, design, pattern and density of these features. Since it is a new idea, there are several possibilities to explore. Concrete suggestions consist in adding dimples on the root area of the fan blade, since it is a region usually affected by stall, and on the pressure side as well. Several diameters and depths could be studied and its design could be changed to hexagonal, oval and diamond shape. Research conducted with golf-balls can be used as groundwork and inspiration to further investigate the dimpled fan design.

Regarding the experimental measurements, it is important to repeat them with a reference model of better quality and an undamaged dimples' model. Only then, concrete conclusions can be drawn from the setup. Additionally, it seems important to evaluate the dimples' effect on real size fan models, since the reduction in size applied to the experimental models used in this study lead to tiny dimple geometries whose effect may have been compromised.

Overall, considering this thesis analyzed solemnly the broadband boundary layer noise component, the immensity and complexity of detecting sources of aeroacoustic noise and acting upon them becomes clear to the eye. It is also of extreme importance to consider the structural dynamics of the heat pump housing whithin all the envolving components (fan, comrpessor, pipes, electronics, *etc*). In my personal opinion, the journey towards a silent fan, and thus a silent heat pump, is comprised of several small accomplishments, acting upon all of the involving components, where juggling every modest dB improvement together is the road to success.

References

[1] D. A. Bies, C. H. Hansen, C. Q. Horward *Engineering Noise Control*, 5^{th} edition, New York: CRC Press, 2018. Chap. 10.2.

[2] R. van de Vondervoort. *Prediction of Aerodynamic Performance and Noise Production of Axial Fans*, Faculty of Engineering Technology, University of Twente, 2015.

[3] D. L. Huff. *Noise Reduction Technologies for Turbofan Engines*, NASA Glenn Research Center, 2006.

[4] Newsletter: *NASA Fact Sheet: Reducing Aircraft Noise to Improve Our Quality of Life - NASA's Quiet Aircraft Technology Program*, Langley Research Center, 2002.

[5] P. Ala-Honkola (December 22, 2017) *Updated aviation safety rules and new rules on drones approved by the Council*, European Council, Coundil of European Union, retrieved from `http://www.consilium.europa.eu/en/press/press-releases/2017/12/22/updated-aviation-safety-rules-and-new-rules-on-drones-approved-by-the-council/`, accessed March 2018.

[6] C. Vetterlein (May 23, 2019) *Increase in air traffic - challenge for the aviation industry*, ARTS, retrieved from `https://www.arts.aero/blog/aircraft-noise-and-aircraft-noise-protection`, accessed March 2018.

[7] Amazon Prime Air (December 7, 2016) *First Prime Air Delivery*, Amazon Prime Air, retrieved from `https://www.amazon.com/Amazon-Prime-Air/b?ie=UTF8&node=8037720011`, accessed March 2018.

[8] R. Kaufman (July 7, 2016) *Shh!: UAS Go Silent*, Inside Unmanned Systems, retrieved from `http://insideunmannedsystems.com/shh-uas-go-silent/`, accessed March 2018.

[9] M. Abbasi, M. R. Monazzam, A. Akbarzadeh, S. A. Zakerian, M. H. Ebrahimi. *Impact of wind turbine sound on general health, sleep disturbance and annoyance of workers: a pilot- study in Manjil wind farm, Iran*, Journal of Environmental Health Science and Engineering 13:71-89, 2015.

[10] M. Ittershagen (March 13, 2017) *Heat pumps and the like: low-frequency hum annoys a growing number of people*, Umwelt Bundesamt, retrieved from `https://www.umweltbundesamt.de/en/press/pressinformation/heat-pumps-the-like-low-frequency-hum-annoys-a`, accessed April 2018.

[11] C. Horváth, B. Tóth, P. Tóth, J. Vad. *Reevaluating Noise Sources Appearing on the Axis for Beamforming Maps of Rotating Sources*, International Conference on Fan Noise, Technology and Numerical Methods, 2015.

[12] O. Verhoeven. *Trailing Edge Noise Simulations using IDDES in OpenFOAM*, TU Delft, 2011.

[13] Newsletter: *NASA Facts: Making Future Commercial Aircraft Quieter*, NASA Glenn Research Center, 1999.

[14] NASA gallery (March 30, 2016) retrieved from `https://www.nasa.gov/aeroresearch/programs/aavp/aetc/subsonic`, accessed April 2018.

[15] J. Banke. *NASA Helps Create a More Silent Night*, NASA Aeronautics Research Mission Directorate, 2010.

[16] C. A. Arce-Leon. *Modelling of Serrated Trailing Edges to Reduce Aerodynamic Noise in Wind Turbines Using Computational Fluid Dynamics*, Department of Information Technology, Uppsala Universitet, 2010.

[17] E. Envia. *Fan Noise Reduction: An Overview*, International Journal of Aeroacoustics 1:43-64, 2002.

[18] J. M. Brookfield, I. A. Waitz. *Trailing-Edge Blowing for Reduction of Turbomachinery Fan Noise*, Journal of Propulsion and Power, 16:57-64, 2000.

[19] D. H. Geiger. *Comparative Analysis of Serrated Trailing Edge Designs on Idealized Aircraft Engine Fan Blades for Noise Reduction*, Virginia Polytechnic Institute and State University, 2004.

[20] H. Xia, P. G. Tucker, S. Eastwood, M. Mahak. *The influence of geometry on jet plume development*, Progress in Aerospace Sciences 52:56-66, 2012.

[21] A. Brocklehurst, G. N. Barakos. *A review of helicopter rotor blade tip shapes*, Progress in Aerospace Sciences 56:37-74, 2013.

[22] L. Josephs. (July 20, 2017) *Drones are our noisy future: People find their buzzing more annoying than cars or trucks*, Quartz, retrieved from `https://qz.com/1033675/`, accessed April 2018.

[23] R. Curry. (April 28, 2016) *Award for Drone Noise Reduction Technology*, UAS Vision, retrieved from `https://www.uasvision.com/2016/04/28/award-for-drone-noise-reduction-technology/`, accessed April 2018.

[24] *Taking the drone out of drones*, Dotterel, retrieved from `http://dotterel.co.nz/`, accessed April 2018.

[25] J. Mathew et. al. *Serration Design Methodology for Wind Turbine Noise Reduction*, Journal of Physics: Conference Series 753, 2016.

[26] M. Maizi, M. H. Mohamed, R. Dizene, M. C. Mihoubi. *Noise reduction of a horizontal wind turbine using different blade shapes*, Renewable Energy 117:242-256, 2018.

[27] C. Horváth, J. Vad. *Broadband Noise Source Model Acoustical Investigation on Unskewed and Skewed Axial Flow Fan Rotor Cascades*, Conference on Modelling Fluid Flow, 14^{th} International Conference on Fluid Flow Technologies, 2009.

[28] L. Huang, J. Wang. *Acoustic Analysis of a Computer Cooling Fan*, The Journal of the Acoustical Society of America 118:4, 2005.

[29] F. Zenger, S. Becker. *Fluid Mechanical and Acoustic Characterization of Low-Pressure Axial Fans with different Blade Skew*, Institute of Process Machinery and Systems Engineering, University of Erlangen-Nuremberg, 2016.

[30] A. Nashimoto, N. Fujisawa, T. Akuto, Y. Nagase. *Measurements of Aerodynamic Noise and Wake Flow Field in a Cooling Fan with Winglets*, Journal of Visualization 7:85-92, 2004.

[31] Ebm-papst (August 4, 2004) *Fan blades with winglets for quiet fans*, retrieved from `http://www.newark.com/pdfs/techarticles/mro/fanBladesForQuietFans.pdf`, accessed April 2018.

[32] D. Deb Nath, k. Viswanath, A. Bhai Patel. *Experimental Study of the Effect of Serrations on Axial Flow Fan Blade Trailing Edge*, ASME 2016 International Mechanical Engineering Congress and Exposition 1:11–17, 2016.

[33] X. Liu, H. Kamliya Jawahar, M. Azarpeyvand. *Wake Development of Airfoils with Serrated Trailing Edges*, University of Bristol - Explore Bristol Research, 2016.

[34] M. G. Gruber, M. Azarpeyvand, P. F. Joseph. *Airfoil trailing edge noise reduction by the introduction of sawtooth and slittled trailing edge geometries*, Proceedings of the 20^{th} International Congress on Acoustics, ICA 2010.

[35] *Fe2 Owlet axial fan* (December 5, 2015) Asknature, retrieved from `https://asknature.org/idea/fe2-owlet-axial-fan/`, accessed April 2018.

[36] R. W. Derksen, J. R. Bender. *Aerodynamic shape optimization of axial flow fan nose cones*, Computer Aided Optimum Design in Engineering XII 125:109-118, 2012.

[37] A. Clay. *Axial Fan Noise Literature Review and Similitude Analysis*, Bosch Thermotechnik GmbH. Junkers, Germany, 2018.

[38] R. E. Longhouse. *Vortex shedding noise of low tip speed, axial flow fans.* Journal of Sound and Vibration 53:25-46, 1977.

[39] R. B. Langtry, F. R. Menter. *Correlation-Based Transition Modeling for Unstructured Parallelized Computational Fluid Dynamics Codes*, The American Institute of Aeronautics and Astronautics 47:2894-2906, 2009

[40] F. R. Menter, R. Langtry, S. Volker's. *Transition Modelling for General Purpose CFD Codes*, Flow, Turbulence and Combustion 77:277-303, 2006.

[41] Ansys, Inc. (January 23, 2009) *ANSYS FLUENT 12.0 Theory Guide*, retrieved from `http://www.afs.enea.it/project/neptunius/docs/fluent/index.htm`, accessed March 2018.

[42] N. Curle. *The influence of solid boundaries upon aerodynamic sound*, Proceesings of the Royal Society of London, Series A (Mathematical and Physical Sciences) 231:505-514, 1995.

[43] E. Livya, G. Anitha, P. Valli. *Aerodynamic Analysis of Dimple Effect on Aircraft Wing*, International Journal of Aerospace and Mechanical Engineering 9:2-11, 2015.

[44] W. R. Michalchuk. *An Investigation of Different golf-ball Dimple Flow Fields*, University of Tennessee, Knoxville Trace: Tennessee Research and Creative Exchange, 2006.

[45] K. Maehara, K. Ihara, H. Shimosaka, M. Inoue, A. Kasashima. Bridgestone Sports Co., Ltd., Tokyo, Japan, *golf-ball*, patent number 5935023, 1999.

[46] A. M. Somani. *The Comparison and Design of golf-balls*, California State Science fair, 2010.

[47] T. Chang-Hsien, C. Chih-Yeh, L. Jik-Chang, H. Qing-Shan. *Effects of golf-ball dimple configuration on aerodynamics, trajectory, and acoustics*, National Ping-Tung University of Science and Technology, 2007.

[48] H. K. Versteeg, W. Malalasekera. *An Introduction to Computational Fluid Dynamics*, 2^{nd} edition, Edinburgh Gate: Pearson Education Limited, 2007. Chap. 3.1.

[49] 3D Systems. (July 5, 2018) *What is MJP (MultiJet Printing)?* retrieved from `https://www.3dsystems.com/resources/information-guides/multi-jet-printing/mjp`, accessed July 2018.

[50] Wiring Diagram, Amazon, retrieved from `https://images-na.ssl-images-amazon.com/images/I/51ElbekUJmL.jpg`, accessed May 2018.

Appendices

Appendix A

Workflow

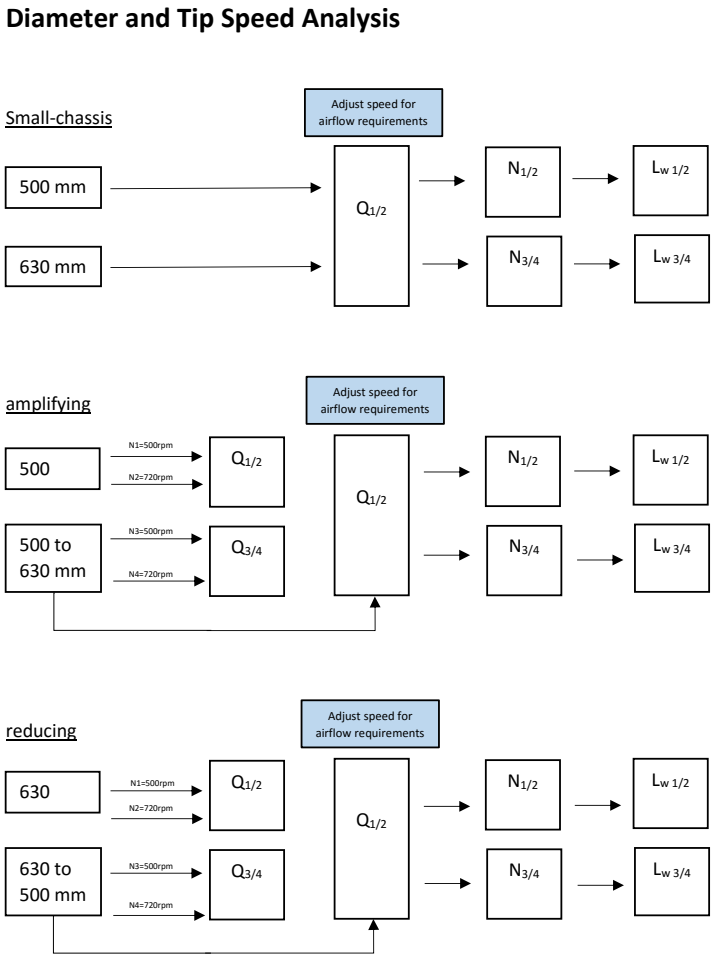

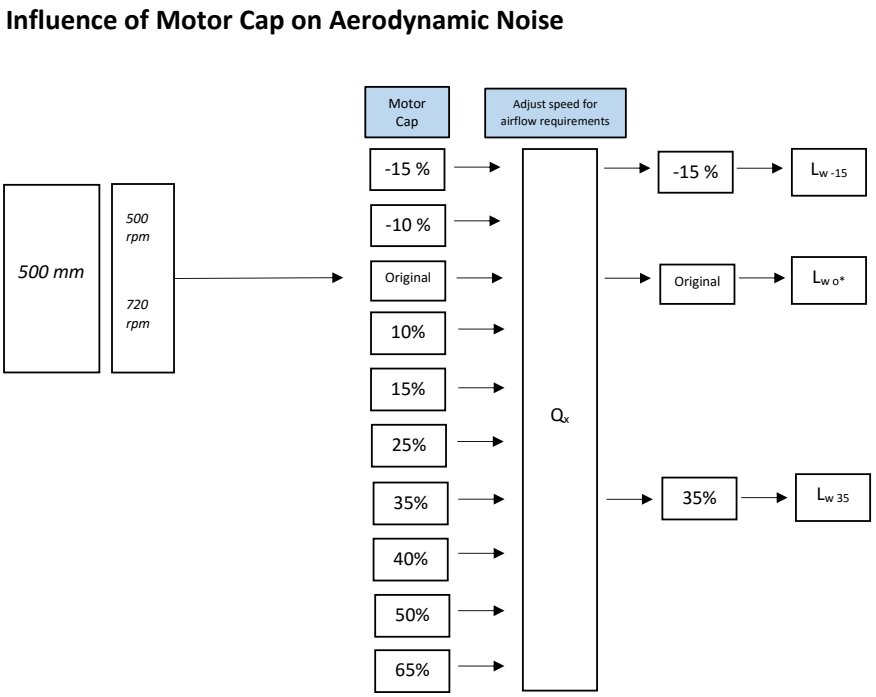

Figure A.2: Simulation workflow for Chapter 5 - ⌀500 fan.

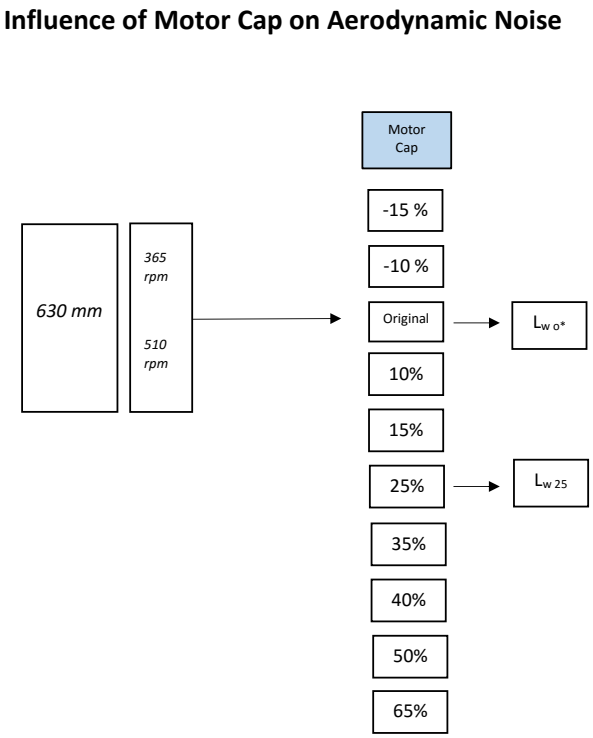

Figure A.3: Simulation workflow for Chapter 5 - ⌀630 fan.

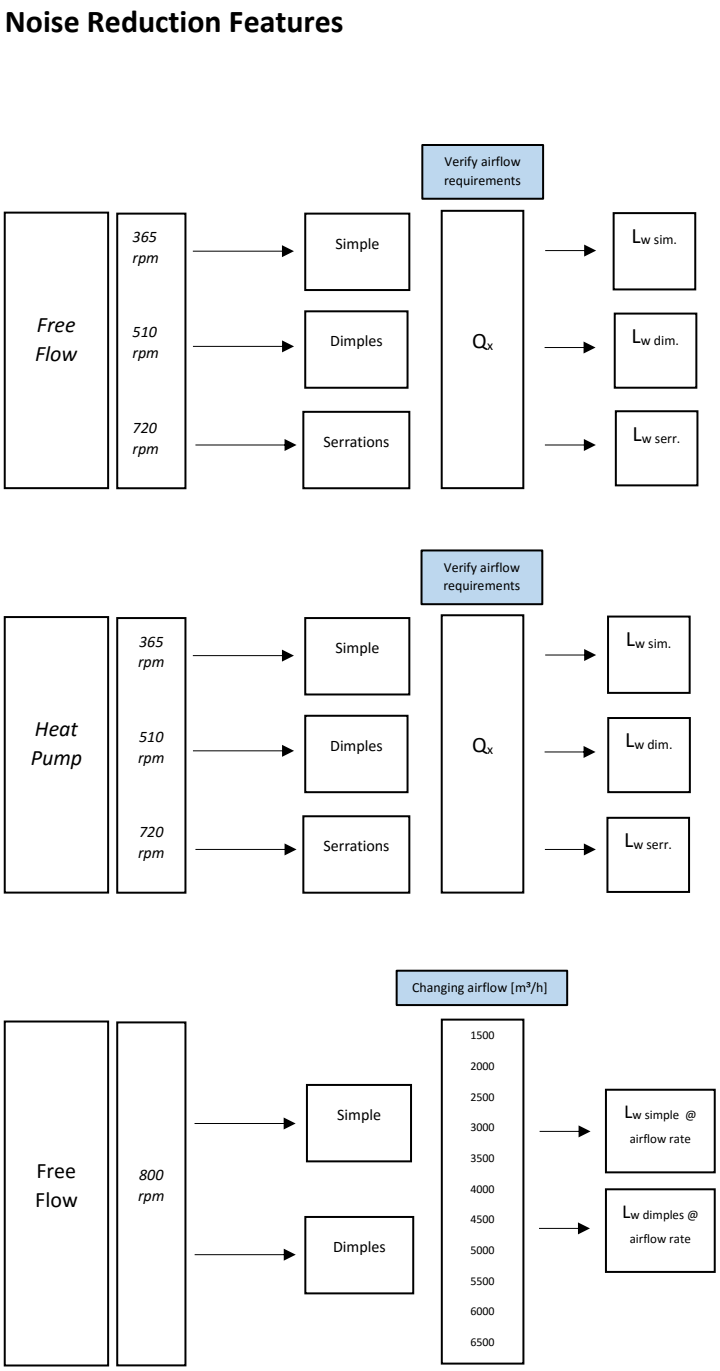

Figure A.4: Simulation workflow for Chapter 6.

Appendix B

Technical Drawings

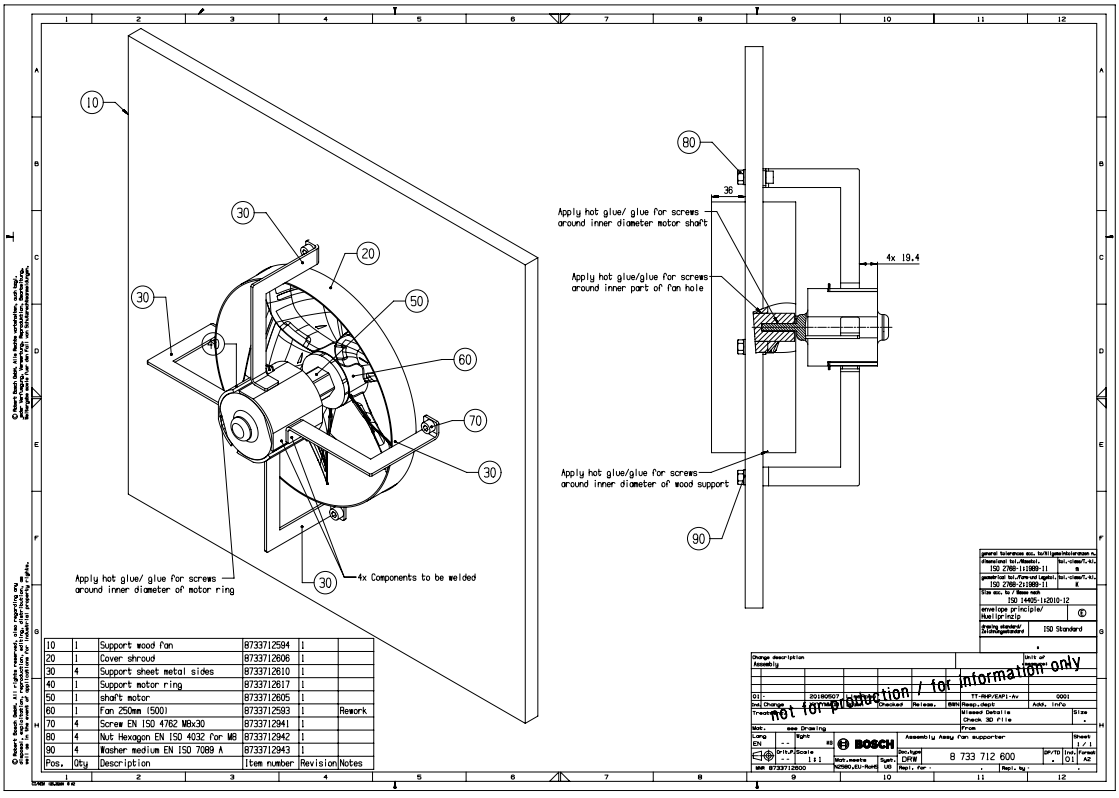

Pos.	Qty	Description	Item number	Revision	Notes
10	1	Support wood fan	8733712594	1	
20	1	Cover shroud	8733712606	1	
30	4	Support sheet metal sides	8733712610	1	
40	1	Support motor ring	8733712617	1	
50	1	shaft motor	8733712605	1	
60	1	Fan 250mm (500)	8733712593	1	Rework
70	4	Screw EN ISO 4762 M8x30	8733712941	1	
80	4	Nut Hexagon EN ISO 4032 for M8	8733712942	1	
90	4	Washer medium EN ISO 7089 A	8733712943	1	

Figure B.1: Technical Drawing Assembly.

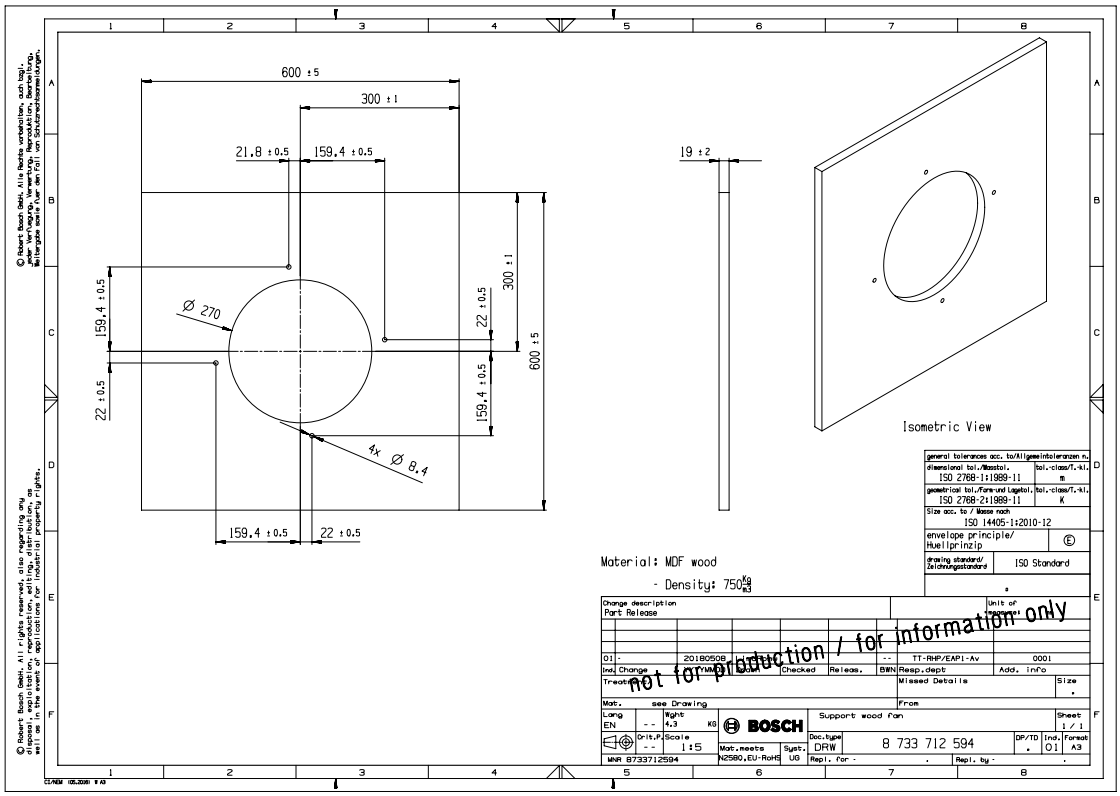

Figure B.2: Technical Drawing Wood Panel.

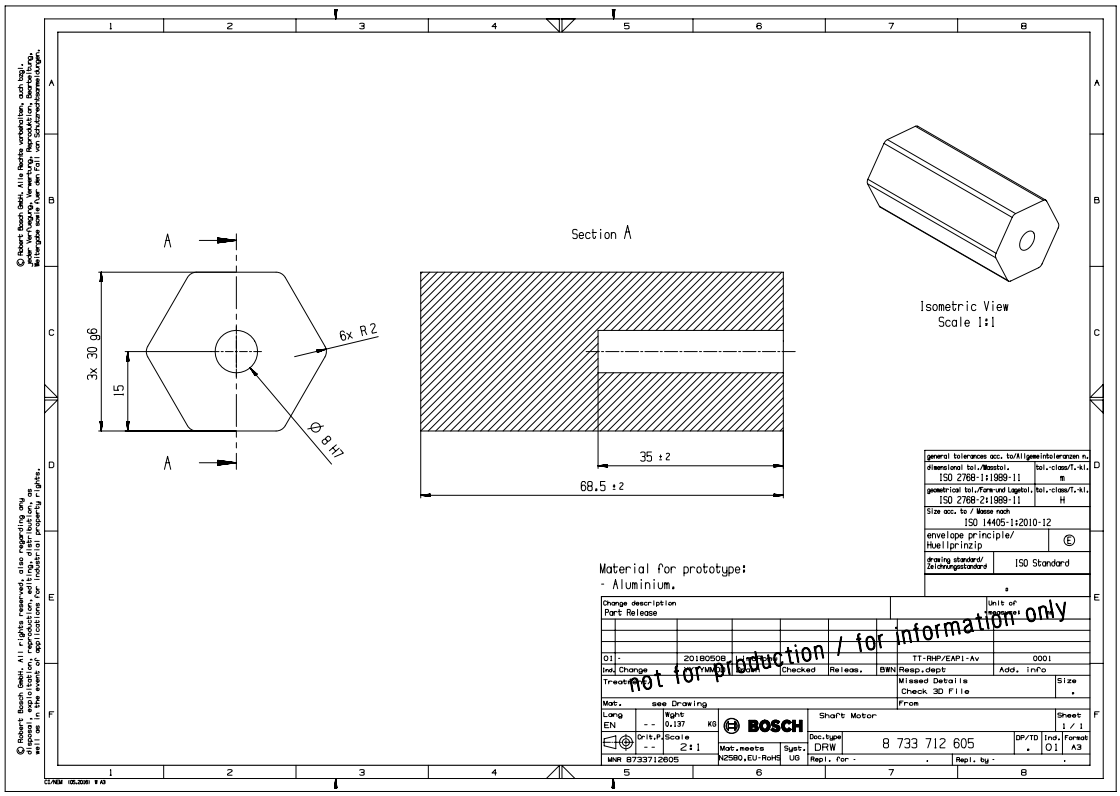

Figure B.3: Technical Drawing Hexagonal Shaft - connection between fan and motor shaft.

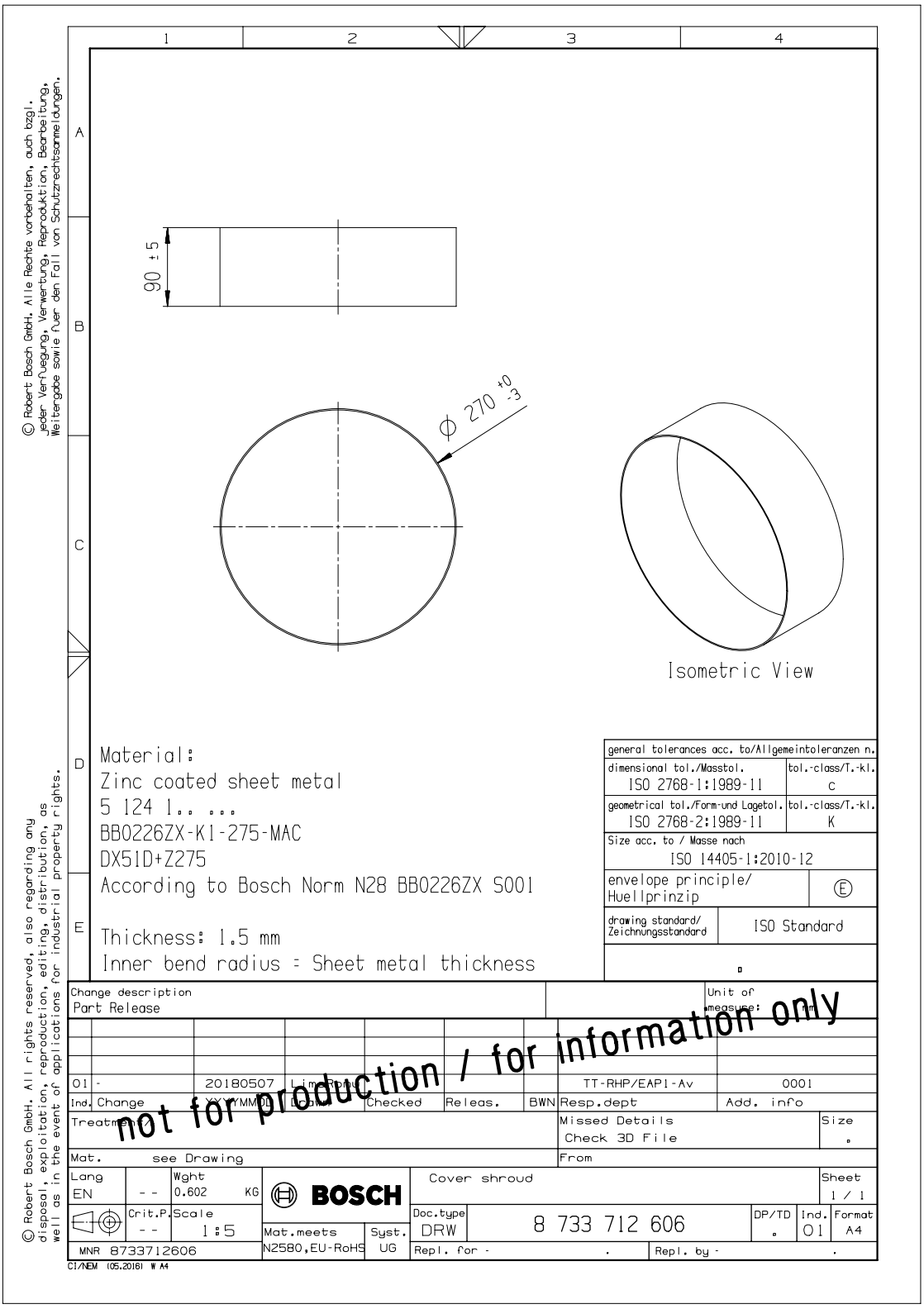

Figure B.4: Technical Drawing Fan Shroud.

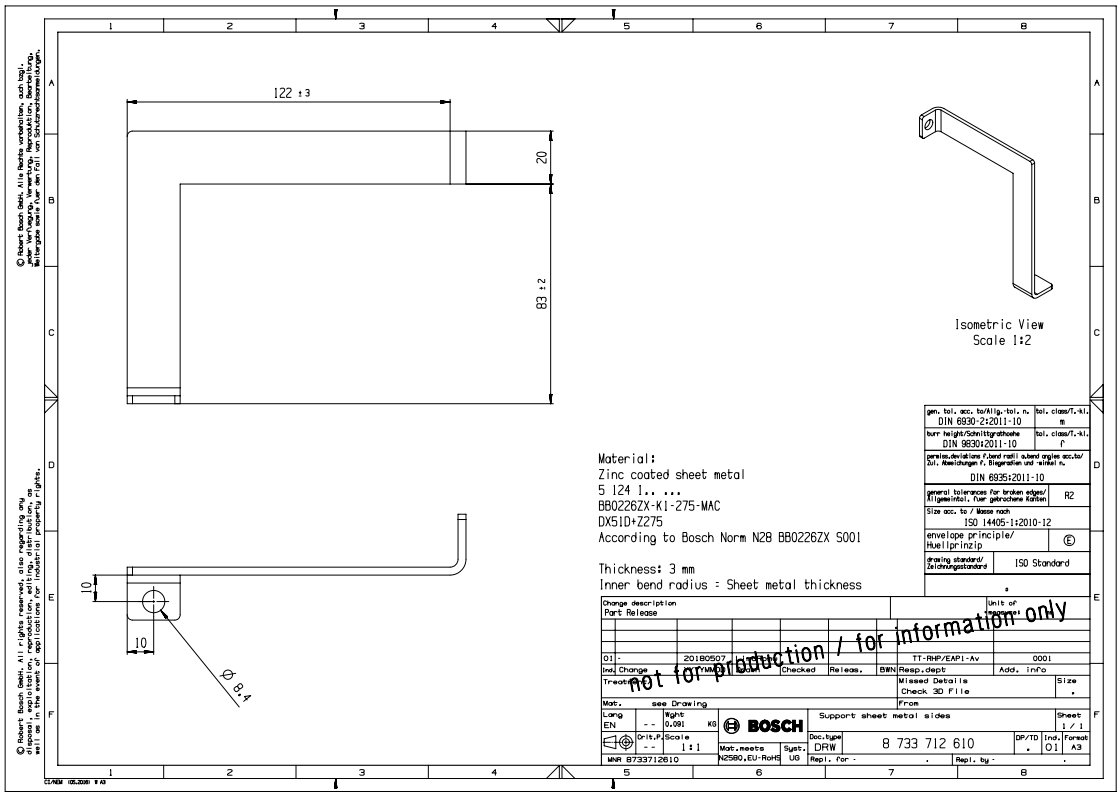

Figure B.5: Technical Drawing Motor Support.

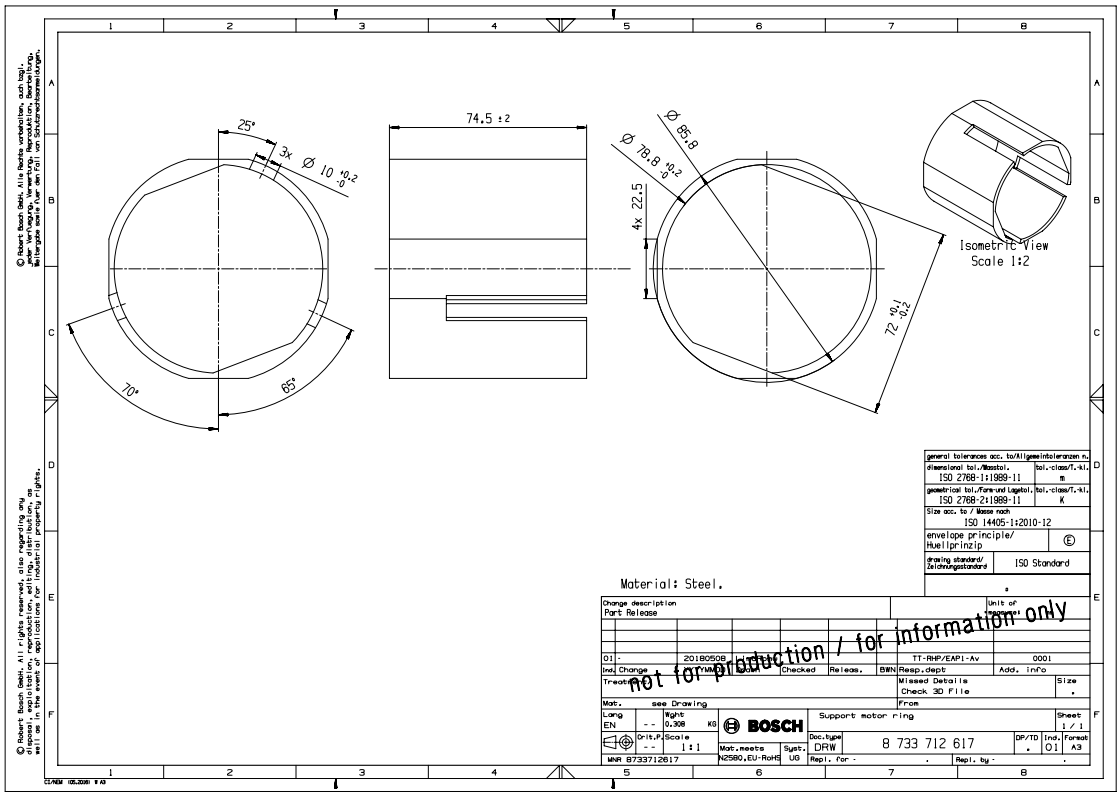

Figure B.6: Technical Drawing Motor Ring.